Syntheses and Characterizations of Ta$_3$N$_5$ Thin Films and Nanotubes for Photoelectrochemical Applications under Visible Light Irradiation

By

Sherdil Khan

Institute of Physics

Thesis submitted to the Universidade Federal do Rio Grande do Sul, Brazil as a partial requirement to obtain the degree of Doctor in Sciences, under the supervision of Prof. Dr. Sérgio Ribeiro Teixeira (Institute of Physics-UFRGS) and co-supervision of Prof. Marcos José Leite Santos (Institute of Chemistry-UFRGS).

November, 2015

بِسْمِ اللَّهِ الرَّحْمَنِ الرَّحِيمِ

"In the name of ALLAH, most Gracious, most Compassionate"

هُوَ الَّذِي أَنزَلَ مِنَ السَّمَاءِ مَاءً لَكُم مِّنْهُ شَرَابٌ وَمِنْهُ شَجَرٌ فِيهِ تُسِيمُونَ ﴿١٠﴾

يُنبِتُ لَكُم بِهِ الزَّرْعَ وَالزَّيْتُونَ وَالنَّخِيلَ وَالأَعْنَابَ وَمِن كُلِّ الثَّمَرَاتِ إِنَّ فِي ذَلِكَ لآيَةً لِقَوْمٍ يَتَفَكَّرُونَ ﴿١١﴾

وَسَخَّرَ لَكُمُ اللَّيْلَ وَالنَّهَارَ وَالشَّمْسَ وَالْقَمَرَ وَالنُّجُومُ مُسَخَّرَاتٌ بِأَمْرِهِ إِنَّ فِي ذَلِكَ لآيَاتٍ لِقَوْمٍ يَعْقِلُونَ ﴿١٢﴾

وَمَا ذَرَأَ لَكُمْ فِي الأَرْضِ مُخْتَلِفاً أَلْوَانُهُ إِنَّ فِي ذَلِكَ لآيَةً لِقَوْمٍ يَذَّكَّرُونَ ﴿١٣﴾

وَهُوَ الَّذِي سَخَّرَ الْبَحْرَ لِتَأْكُلُوا مِنْهُ لَحْماً طَرِياً وَتَسْتَخْرِجُوا مِنْهُ حِلْيَةً تَلْبَسُونَهَا وَتَرَى الْفُلْكَ مَوَاخِرَ فِيهِ وَلِتَبْتَغُوا مِن فَضْلِهِ وَلَعَلَّكُمْ تَشْكُرُونَ ﴿١٤﴾

وَأَلْقَى فِي الأَرْضِ رَوَاسِيَ أَن تَمِيدَ بِكُمْ وَأَنْهَاراً وَسُبُلاً لَعَلَّكُمْ تَهْتَدُونَ ﴿١٥﴾

Al-Quran (Surah, An-Nahl, Verse 10 –15)

"He it is Who sends down water from the sky for you; from it you drink, and by it (grows) trees on which you pasture your cattle (10). Therewith He causes to grow for you herbage, and the olives, and the palm trees, and the grapes, and of all the fruits. Verily there is a sign in this for a people who give thought (11). And He has subjected for you the night and day and the sun and moon, and the stars are subjected by His command. Indeed in that are signs for people who reason (12). And [He has subjected] whatever He multiplied for you on the earth of varying colors. Indeed in that is a sign for people who remember (13). And He it is Who has made the sea subservient that you may eat fresh meat from it and bring forth from it ornaments which you wear, and you see the ships cleaving through it, and that you may seek of His bounty, and that you may be grateful (14). And He has cast firm mountains in the earth that it does not quake with you, and streams and roads that you may be guided aright (15)."

They call it "water" we call it fuel; God make it we break it.

ACKNOWLEDGMENTS

*I would like to thank **ALMIGHTY ALLAH** for blessing me the opportunity to study PhD (Physics) in Federal University of Rio Grande South, Brazil. I would like to thank Institute of Physics, (IF-UFRGS) for the lab facilities and National Council for Scientific and Technological Development (CNPq), Brazil for providing funds. I would like to express my heartiest gratitude to my supervisor Dr. Sergio Ribeiro Teixeira of his massive help and advice throughout my studies. I gained a lot of knowledge by working with him. His patient guidance and friendly behavior made me feel always **"Brazil a home away from my home"**. May Allah bless him a great success in every walk of his life! Ameen.*

Most of all, I would like to thank my co-supervisor Dr. Marcos José Leite Santos, for his enthusiastic guidance on my work and particularly for his dedication to work even on holidays. I would like to express heartiest thanks to Luana de Lucca for her care and support. I would express my gratefulness to my research group mate Dr. Pedro Migowski for his help in lab works. Also thanks to laboratory technician Mr. Silvio Kirst for his help with laboratory issues and particularly, for the installation of nitridation system. Furthermore, I would like to thank Dr. Rafael Latuada and Mr. Tao Hasse from C-Nano, Ms. Aline Tais and Dr. Daniel Baptista for their kind help with operating the SEM/HRTEM instruments. Also my friends and lab colleagues Dr. Jesum Fernandes, Dr. Renato Gonçalves, Dr. Irfan Qadir, Dr. Dario Eberhardt, Hemerson Pablo, Mauricio Vaz, Maximilliao Zapata, Gustavo Lanes Ariadne Koche, Luana Muller, Flavia Sonaglio, Guilherme Rosa, Guilherme Machado, Tiago Cassol, Wellington Dougless, Nisar Khan, Aasim Khurshid, Muhammad Farhan for offering their support and encouragement during the whole PhD course. Most of all I appreciate Mr. Otelo Macahdo and Mr. Andre Vargas (PUCRs) for their help in XRD measurements, Dr. Antonio Marcos and Mr. Julio Schoffen for their help in magnetron sputtering, Dr. Claudio Radtke, Fabiano Bernardi for XPS measurements, Dr. Henry Boudinov and Dr. Denise Azambuja for their useful discussions and Dr. Marcelo Pereira and Dr. Ricardo Rego for the optical measurements, Dr. Jacqueline Ferreira for chemical reagents and electrolytes preparation and Dr. Jairton Dupont for his continuous support.

Last, but not the least I send my great gratitude to my father; Safdar Zaman Khan Jadoon, my mother; Shamshad Bibi, both of my sisters Zainab Jadoon and Shumaila Shahzad and my uncle Badiul-Zaman Khan Jadoon for their decision to send me here and also for their care and emotional support for all turns of my life. I love them all; they are a great source of inspiration in my life.

TABLE OF CONTENTS

List of Figures

List of Tables

ABSTRACT

In this work thin films and nanotubes (NTs) of Ta_3N_5 have been synthesized by thermal nitridation of amorphous Ta_2O_5 starting materials. Ta_2O_5 thin films were prepared by radio frequency magnetron sputtering; whereas Ta_2O_5 NTs were prepared by electrochemical anodization. With the aim to investigate electronic, optical structural, surface, and particularly photoelectrochemical properties; the Ta_3N_5 samples were studied employing thorough characterization techniques. X-ray diffraction and high resolution electron microscopy analyses have shown that Ta_3N_5 thin films exhibit monoclinic phase whereas Ta_3N_5 NTs present orthorhombic crystalline structure of Ta_3N_5. Utilizing Ta_3N_5 thin films the optical constants were obtained by spectroscopic ellipsometry. The obtained dielectric constant of Ta_3N_5 thin film was in the range of 7–9 in the visible spectral region (3.1–1.7 eV). After studying Ta_3N_5 thin films the investigations were focused on the NTs. To preserve the tubular morphology of Ta_3N_5 NTs at higher nitridation temperatures the anodization was optimized by fine-tuning the adherence and the wall thickness of Ta_2O_5 NTs. The Rietveld refinement has confirmed that in addition to oxygen substitutional defects the nitridation process results in Schottky defects of nitrogen and tantalum within the crystalline structure. Utilizing cyclic voltammetry, chronoamperometry and electrochemical impedance spectroscopy it was observed for the first time that lower photoelectrochemical performance of pristine T_3N_5 NTs is attributed to the presence of trapping states associated with T_3N_5 NTs–electrolyte interface in standard electrolyte. Even highly crystalline pristine Ta_3N_5 NTs could not cope with these trapping states. These states devastate the performance of the photoanode and present the necessity of applying higher biasing (> 1.23 V vs RHE); which is a major drawback of using pristine Ta_3N_5 NTs for water splitting. These were not observed in the electrolyte containing sacrificial reagent due to its efficient hole scavenging ability. Electrochemical Impedance spectroscopy has shown that the charge transportation at the Semiconductor–Electrolyte interface is highly influenced by the nitridation conditions; however, the flat band of pristine Ta_3N_5 NTs remained unchanged. It was found that for improved photoelectrochemical performance of Ta_3N_5 NTs the nitridation temperature should be high enough to improve crystallinity but the time should be short enough to preserve the tubular morphology. The improved photoelectrochemical performance was related to low oxygen content, high crystallinity, low defects formation and low interfacial charge transfer at Semiconductor–Electrolyte interface, obtained at optimum anodization and nitridation conditions.

RESUMO

Neste trabalho, filmes finos e nanotubos (NTs) de Ta_3N_5 foram sintetizados por termo-nitretação a partir de Ta_2O_5 amorfo. Filmes finos de Ta_2O_5 foram preparados por rádio frequência *magnetron sputtering* e os nanotubos foram preparados por anodização electroquímica. Foram investigadas as propriedades eletrônicas, ópticas, estruturais, superfíciais e, particularmente, as propriedades fotoeletroquímicas dos amostras de Ta_3N_5. Difração de raios-X e análises de microscopia eletrônica de alta resolução mostraram que filmes finos de Ta_3N_5 apresentam fase monoclínica, enquanto nanotubos de Ta_3N_5 estrutura cristalina ortorrômbica. Para os filmes finos de Ta_3N_5 foram obtidos constantes ópticas por elipsometria espectroscópica. O valor obtido para a constante dielétrica foi de 7–9 na região espectral visível (3,1-1,7 eV). Após o estudo dos filmes finos de Ta_3N_5 as investigações centraram-se nos nanotubos. Para preservar a morfologia tubular em altas temperaturas de nitretação, o processo de anodização foi otimizado para aumentar a aderência e a espessura da parede dos nanotubos de Ta_2O_5.O refinamento Rietveld mostrou que o processo de nitretação resulta em defeitos Schottky de nitrogênio e tântalo, além de isso, a amostra apresenta defeitos substitucionais do oxigênio. Utilizando voltametria cíclica, cronoamperometria e espectroscopia de impedância electroquímica foi observado que o desempenho fotoeletroquímico inferior dos nanotubos puros de Ta_3N_5 é atribuído à presença de estados aprisionados associados a interface dos nanotubos de Ta_3N_5–electrólito com electrólito padrão. Ainda, mesmo altamente cristalinos os nanotubos puros de Ta_3N_5 não podem suportar os estados de aprisionamento mencionados, que prejudicam o desempenho do fotoanodo e, assim, necessitam a aplicação de maior polarização externa (> 1,23 V vs RHE). Estes resultados não foram observados no electrólito contendo reagente de sacrifício. A espectroscopia de impedância electroquímica mostrou que o transporte de carga na interface de semicondutores–eletrólito é altamente influenciada pelas condições de nitretação. No entanto, a banda plana de nanotubos de Ta_3N_5 puro mantem-se inalterada. Verificou-se que para um melhor desempenho fotoelectroquímico das nanotubos de Ta_3N_5 a temperatura de nitretação deve ser suficientemente elevada para melhorar a cristalinidade, mas o tempo deve ser curto o suficiente para preservar a morfologia tubular. A melhora do desempenho fotoeletroquímico foi relacionada com baixo teor de oxigênio, alta cristalinidade, baixa formação de defeitos e baixa transferência de carga na interface do semicondutor com o eletrólito, obtidos em condições de anodização e nitretação ideais.

INTRODUCTION AND OVERVIEW

The global population growth coupled with industrial developments will pose an enormous challenge in meeting current rising energy demand in the near future. The old fashioned fossil fuels widely used as energy source all over the world have a life time. The energy demand, combined with environmental issues, as well as the higher prices of fossil fuels have motivated scientific society to seek alternative, environmentally-friendly low-carbon energy sources.[1] Continuing this line of thought, the challenge remains to find a source of energy that is abundant, free and sustainable. The most interesting idea is to harvest the energy of the sun, which is constantly bombarding the Earth with enough energy to sustain society over any foreseeable future.[2,3] Sunlight radiates typically ca. 700 W m^{-2} in the Sunbelt regions which is a huge amount of energy. Sun energy at the top of earth´s atmosphere consists of is 50% infra red (IR), 40% visible region (VR), and 10% ultra violet (UV). Radiation passing through the atmosphere is attenuated by molecules (O_3, H_2O, CO_2) and suspended particulates that can scatter or absorb portions of the spectrum.[4] The consumed energy per year on the planet Earth is (4.1×10^{20} J in 2001) and the energy from the sun striking the Earth for every 1 h is (4.3×10^{20} J).[5] Therefore, harnessing solar energy would definitely fulfill all of the electrical and chemical energy demands of the modern civilization.[2] According to the report "A Sun Bath to Brazil" by Instituto of Vitae Civilis; Brazil receives solar energy of about 1013 MWh (mega watt hours) per year, which corresponds to 50 thousand times the annual electricity consumption in the country. With that intense solar radiation, Brazil possesses enormous potential for research in solar energy harvesting.

To utilize sunlight as a clean energy source one should consider the process to capture, convert and distribute the energy. In this regard, a lot of techniques have been developed to use sun as a source of energy.[6] An interesting choice to avoid the environment contamination is to utilize hydrogen as a green fuel because hydrogen produces water as a byproduct. However, this argument would have a significant meaning, only if the hydrogen is produced by a clean way. Currently, industry uses steam methane reforming (SMR) to produce hydrogen, this process generates typically 5 kg CO_2/kg of H_2 by an annual discharge of about 240 mega tons CO_2 in the atmosphere. Therefore hydrogen would be considered as a clean fuel if and only if it is produced by a clean source under clean mechanisms.[1]

Hydrogen produced by a clean mechanism offers a great potential to fulfill the clean energy requirements, as we can consider water as the greatest reservoir of hydrogen on earth. The most potential choice is to utilize certain mechanism to produce hydrogen by harvesting

sunlight result into splitting the chemical bond between hydrogen and oxygen. These mechanisms are photolysis and photoelectrolysis. Both of these techniques utilize a suitable semiconductor as a catalyst. In recent years, photoelectrolysis has emerged as a phenomenal route to perform water splitting under light irradiation. In photoelectrolysis, a suitable semiconductor is used as a photoelectrode separated by a counter electrode and both are immersed in water; sunlight light is irradiated on the semiconductor generating charge carriers. The minority carriers diffuse to the semiconductor–water interface; whereas the majority carriers are transferred to the counter electrode. Depending on the type of the semiconductor; hydrogen is produced on one electrode and oxygen at the other. Several semiconductors have been studied to produce hydrogen by photoelectrochemical (PEC) water splitting. [7] For solar PEC water splitting the semiconductor should fulfill certain requirements such as visible light absorbance, efficient charge separation and transportation and long time stability. Furthermore, the development of the semiconductor at the nanoscale has been featured in the forefront of materials science because of their great potential for applications in the clean energy application.

Ta_3N_5 has emerged as a promising semiconductor for water splitting applications. Within the context of improved performance, several nano-morphologies of Ta_3N_5 such as nanoparticles (NPs), [8] Nanorods (NRs), [9] Nano urchins (NUs) [10] and Nanotubes (NTs) [11] have been developed to achieve water splitting. For PEC applications 1D nature of NTs that helps the facile charge transportation and their large surface area make them promising for PEC applications. For PEC water splitting nanotubes of Ta_3N_5 have been firstly synthesized in 2010 by Feng et al by nitridation of Ta_2O_5 NTs prepared by anodization. [12] Later on, Bard´s group has shown further progress by loading oxidation co-catalysts. [13] Furthermore, enhancement in the photocurrent has been shown by Schumki´s group; reason of that was proposed to be modified anodization process for the synthesis of Ta_2O_5 NTs and loading catalyst on Ta_3N_5 NTs. [14] In addition, they have shown barium and tungsten doping of Ta_3N_5 NTs separately in two different reports for water splitting that resulted in to enhanced PEC performance. [15,16] Zhang et al. have proposed the mechanism of bridging the NTs by lowering the anodization temperature for the synthesis of Ta_2O_5 NTs to transform them in to pristine Ta_3N_5 NTs. [17] Based on the previous literature on the Ta_3N_5 NTs; only improving the PEC activities have been reported by utilizing co-catalysts and/or doping, etc. Therefore, it is more reasonable to highlight that the pristine Ta_3N_5 NTs need further fundamental investigations for tailoring their physico-chemical properties for efficient water splitting.

Aiming to contribute this research to study the PEC properties of Ta_3N_5, we have synthesized, characterized and applied Ta_3N_5 thin films and Ta_3N_5 NTs for photoelectrochemical applications under the visible light irradiation. Thin films have helped to determine the dielectric constant of Ta_3N_5 that was utilized in Mott-Schottky curves to get the insight to the band structure of Ta_3N_5 for PEC applications.

This research work is divided into six chapters. **Chapter 1** reviews the fundamental concepts and focuses on the understanding of photoelectrochemical processes and water splitting performed by photoelectrochemical routes, by using semiconductors–electrolyte interfaces. **Chapter 2** deals with the experimental part, and characterizations; detailed descriptions of equipments and experimental setup are given. **Chapter 3** deals with the determination of the optical constants of Ta_3N_5 thin films. In addition, photoelectrochemical properties of Ta_3N_5 thin films photoelectrodes are studied in phosphate buffer electrolytes set to pH 4, 8 and 12. Further details on thin films can be seen in Appendix 1. Hereafter, we have focused on the Ta_3N_5 nanotubular samples prepared by the nitridation of precursor Ta_2O_5 nanotubes. **Chapter 4** describes the insight to the trapping states driven higher external potential requirement for the pristine Ta_3N_5 nanotubes applied in photoelectrochemical water splitting. In this chapter we have used two electrolytes; one standard electrolyte for water oxidation and the other that contains sacrificial reagent. From the comparison of the photoelectrochemical experiments we have observed the major drawback of using pristine Ta_3N_5 nanotubes that hinders the water splitting reaction and further we discussed the methodologies to circumvent that obstacle of Ta_3N_5 nanotubes for water splitting. **Chapter 5** emphasizes the effect of thermal nitridation on the structural and photoelectrochemical properties of Ta_3N_5 nanotubular photoelctrodes. In this chapter, we have compared the Ta_3N_5 samples as a function of different nitridation conditions by varying time and temperature and optimized the nitridation for improved photoelectrochemical activity. Lastly; **Chapter 6** highlights the general conclusions of this thesis.

Besides the work presented here, we have published two full articles (mentioned below) from the current project and one conference proceeding that published in IOP Science on the basis of Bernhard Gross award for the best work oral presentation in renewable energy research symposium (L) SBPMAT Joao Pessoa meeting, 2014, Brazil.

Publications from the current project

✓   **<u>KHAN, SHERDIL</u>** ; ZAPATA, MAXIMILIANO J. M. ; BAPTISTA, D. ; GONÇALVES, RENATO V. ; FERNANDES, JESUM A. ; DUPONT, JAIRTON ; SANTOS, MARCOS J. L. ; TEIXEIRA, SERGIO R. Effect of Oxygen Content on Photoelectrochemical Activity of Crystallographically Preferential Oriented Porous Ta_3N_5 Nanotubes. Journal of Physical Chemistry C (Print), C **2015**, *119*, 19906−19914

✓   **<u>KHAN, SHERDIL</u>** ; PEREIRA, M. B. ; ZAPATA, MAXIMILIANO J. M. ; SANTOS, MARCOS J. L. ; TEIXEIRA, SERGIO R. ;DUPONT, JAIRTON. Structural, Optical and Photoelectrohcemical Characterizations of Monoclinic Ta_3N_5 Thin Films. PCCP. Physical Chemistry Chemical Physics (Print), 2**015**, *17*, 23952 −23962.

✓   **<u>KHAN, SHERDIL</u>** ; DUPONT, JAIRTON ; SANTOS, MARCOS J. L. ; TEIXEIRA, SERGIO R. Photoelectrochemical Study of Ta_3N_5 Nanotubes for Water Splitting. IOP Conf. Ser.: Mater. Sci. Eng. **2015,** 97, 012007.

CHAPTER 1

SEMICONDUCTOR–ELECTROLYTE INTERFACE FOR PHOTOELECTROCHEMICAL WATER SPLITTING

1.1 Photoelectrochemical cell

A typical photoelectrochemical cell is a setup of three electrodes, working electrode (WE), counter electrode (CE) and reference electrode (RE) immersed in an aqueous solution (**Fig. 1.1**).[18] Light is irradiated on the working electrode which is known as photoelectrode. In a two electrode system when current flows through the cell the interfacial potential of the counter electrode may vary due to the interaction of solution species. This problem can be solved by introducing a reference electrode for which the potential is well defined in electrochemical scale. This ensures the potential is reproducible and is controlled between the WE and RE and current passes through the CE.
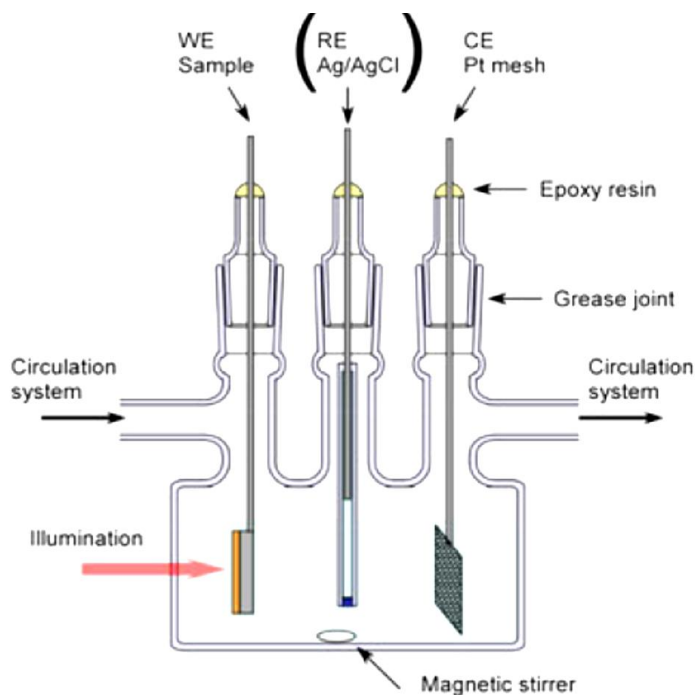
Fig.1. 1 A typical three electrodes photoelectrochemical cell. [18]

Usually, reversed biasing is applied for a semiconductor used for Photoelectrolysis. Under illumination hydrogen is generated at one electrode and oxygen at the other. The direction of the flow of charge carriers determines which electrode produces oxygen and which produces hydrogen.[19] Under light irradiation, n-type semiconductor is used for oxidation reactions; meanwhile p-type semiconductor is used for the reduction. Generally, photoelectrochemical

water splitting using n-type semiconductors is favored in basic media; meanwhile p-type semiconductors are favored in acidic conditions.

1.2. N–type semiconductor in dark

Fig. 1.2 shows an ideal n–type semiconductor/liquid junction in dark. When a semiconductor is immersed in solution; in order to reach electric equilibrium charges must flow across the semiconductor/liquid junction. [20],[21] Considering the equilibrium process under dark, charge for the equilibrium process originates from the donor impurities not from the bonded electrons in the semiconductor lattice. In case, if it originates from the bonded electrons then the decomposition of the semiconductor can be inferred.
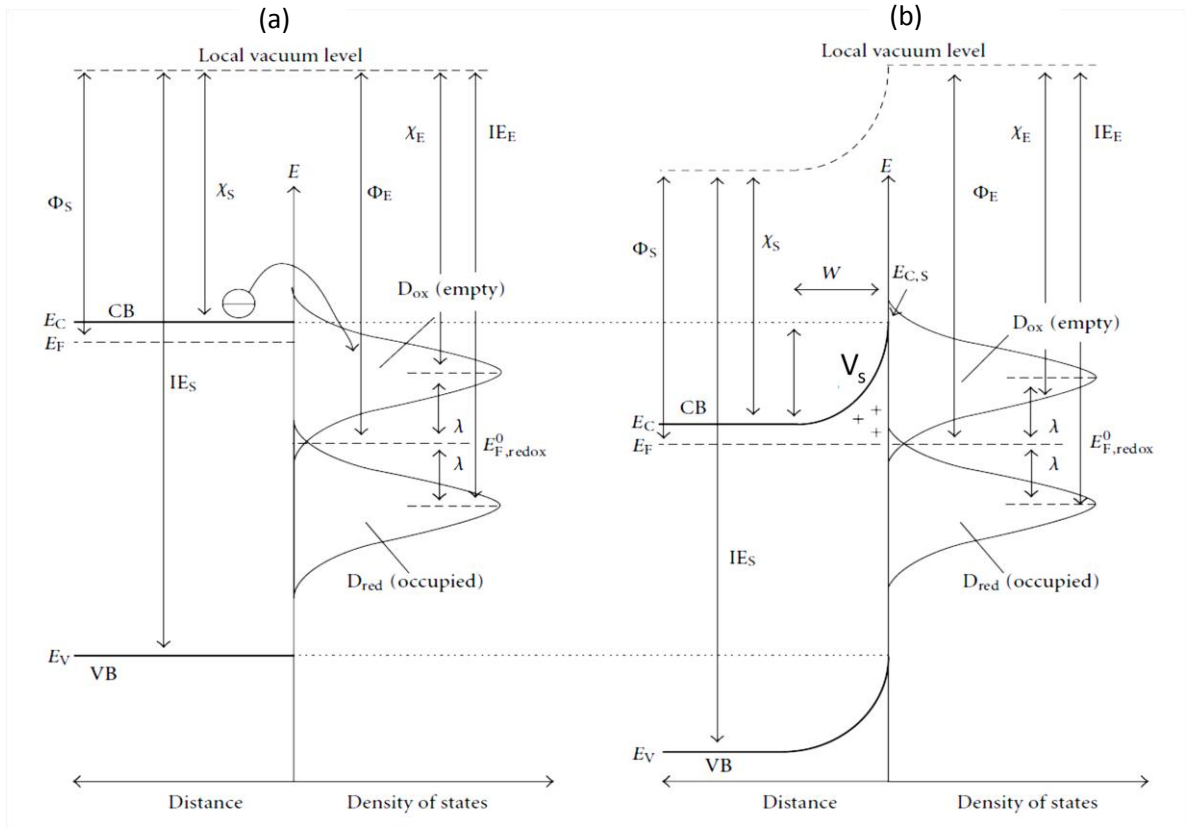
Fig.1. 2 Energy levels in semiconductor (LHS) and electrolyte (RHS) w.r.t vacuum level where Φ, χ, λ represents work function, electron affinity, solvent re-organization energy respectively. Semiconductor-electrolyte interface before (a) and after (b) equilibrium. [20]

The equilibrium process is actually an electrostatic adjustment between the semiconductor and liquid interface. There is a specific region in the semiconductor from which charges are removed for the equilibrium process; beyond that boundary the semiconductor is neutral as a whole. [22] The space where the majority carriers are depleted is named as depletion region or space charge region. The Fermi level in the semiconductor hops down and process stops

unless the Fermi levels are aligned on both sides of the interface. This equilibrium process generates band bending across the interface shown in **Fig.1.2b**. If we consider electrostatic adjustment phenomena on the potential space; we would observe a potential distribution across the interface which is represented along with a simplified equivalent circuit in **Fig. 1.3.** The potential drop across the depletion region is represented by V_{sc} which can be calculated by;

$$V_{sc} = - \left[\frac{e_0 N_D}{2\varepsilon_s} \right] W^2 \tag{1.1}$$

Where W, N_D and ε_s, represent width of depletion region, doping density and static dielectric constant of the semiconductor. Furthermore the capacitance of the depletion region is known as depletion region capacitance C_{SC}. From equation (1.1) it should be noted that the depletion region would be wide for low doped semiconductor and vice versa. Nominal dimensions of W are in 10 nm to 100 nm range.[22]
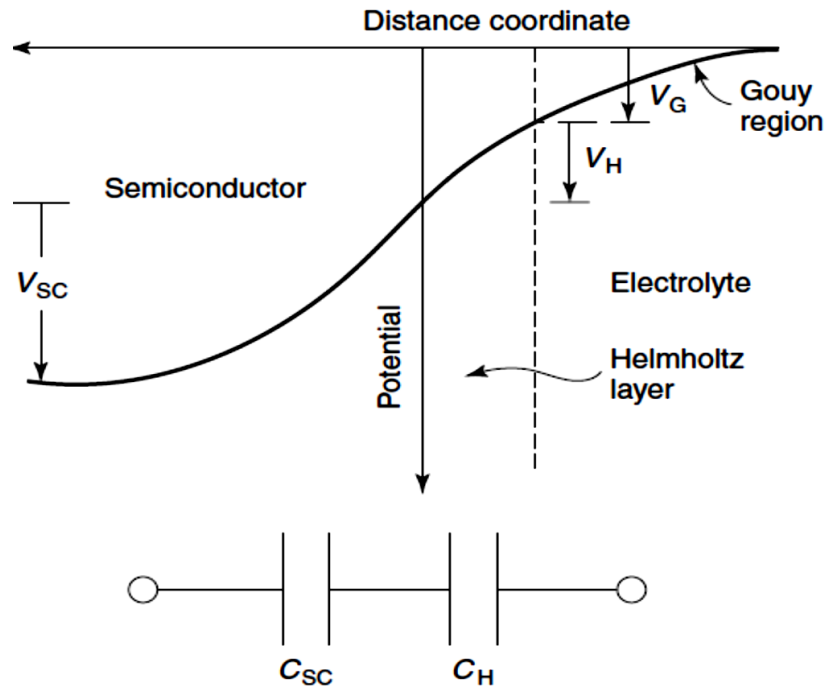
Fig.1. 3 A simplified equivalent circuit for a semiconductor–electrolyte interface.[22a]

Adjacent to the depletion layer there forms a space due to adsorbed species e.g. , for water (H$^+$ or OH$^-$) and oppositely charged solvated ions in the solution, this space is called Helmholtz region. [20] The water species from the electrolyte form inner Helmholtz layer while the solvated ions inside the solution form an outer layer and the potential difference across

these layers is known as V_H and its capacitance is known as Helmholtz capacitance C_H. Typical dimensions of Helmholtz region are 0.3–0.5 nm. [19, 22b, 23] The capacitance of the Helmholtz region is higher than that of the depletion region. Generally on inner Helmholtz region one of the two water species (H^+ or OH^-) dominates depending on the pH of the solution. However, for photoelectrochemical water spitting usually, acidic conditions are used for p-type semiconductors and alkaline conditions are used for n-type semiconductors.
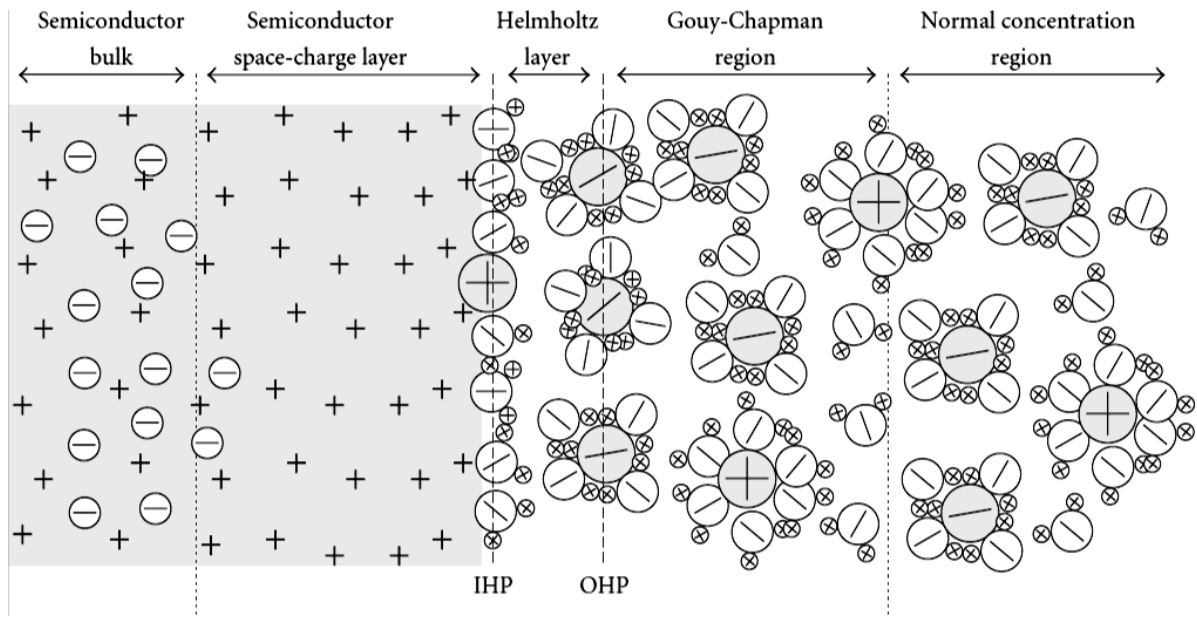
Fig.1. 4 Semiconductor–electrolyte interface in terms of formed regions. [20]

The adsorbed ions (H^+ or OH^-) on the surface of the semiconductor cannot be compensated by the attracted solvated positive ions therefore next to the Helmholtz region another double layer consisting of solvated ions majority of which is positive is formed called Guoy region. [20] This region is a result of residual electric field normal to the surface of semiconductor. Potential drop across this layer is V_G and capacitance of this region is C_G. All of the three regions are depicted in **Fig. 1.4**. The thicknesses of the space charge layer and Gouy layer decrease with increasing concentrations of charge carriers in the photoelectrode and electrolyte, respectively. For example, the thickness range of the Gouy layer is between 10 and 100 nm in aqueous ionic solutions with low ion concentrations, while it decreases to about a mono-molecular layer in 1 M concentrated ionic solutions. Accordingly, it can be omitted in PEC cells, because one uses electrolytes with high ion concentrations that is why the Gouy region is not mentioned in the equivalent circuit of **Fig. 1.3**. [23] However it has a

considerable role for a low concentration electrolyte. By considering all of the potential drops across the interface the total potential drop can be written as;

$$V_t = V_{SC} + V_H + V_G \tag{1.2}$$

Consider now the space charge potential V_{SC}. The potential and charge distribution within the space-charge layer can be described by a one dimensional Poisson equation for the semiconductor/liquid interface presented in **Fig.1. 3**:

$$\frac{\partial^2 \varphi}{\partial x^2} = -\frac{1}{\epsilon \varepsilon_0} \rho \tag{1.3}$$

Where "φ" represents the potential, ϵ and ε_0 are the relative permittivity of the semiconductor and the permittivity of vacuum, respectively, and ρ is the volume charge density. After solving equation (1.3) by two successive integrations assuming $\rho = qN$ (q is the elementary charge; N is the doping concentration) and applying some boundary conditions one obtains the following relation for the width of the depletion region (x = W): [20]

$$W = \left| \frac{2\epsilon \varepsilon_0}{qN} (V_{sc} - \frac{kT}{q}) \right|^{1/2} \tag{1.4}$$

where V_{sc} is potential drop in the space charge layer. The V_{sc} is actually the maximum open-circuit potential. It is the difference between the semiconductor flat band potential (E_{fb}) and Fermi level of the electrolyte. Along with describing V_{sc} by equation (1.1) a simple way to calculate that or $(V_{oc})_{MAX}$ is as follows:[20][24]

$$(V_{oc})_{MAX} = V_{sc} = E_{fb} - E_{f,redox} \tag{1.5}$$

The position of the flat band potential is of fundamental significance as it gives direct information of the conduction band of the semiconductor, which then determines the reduction ability of the semiconductor that it would be active with or without external biasing. The flat band potential can be defined as the potential of the electrode with respect to a reference electrode in solution at which the bands are flat, or at which space charge is absent. There are electrochemical techniques to determine the flat band; including photocurrent onset,

variable intensity light illumination, Mott-Schottky plots etc. From the knowledge of the flat band it is easy to estimate the CB of the semiconductor that further describes the maximum reduction ability of the semiconductor on the energy scale.

1.3. N–type semiconductor under applied voltage (Biasing)

At equilibrium, semiconductor-liquid interface exhibit an equivalent Fermi level i.e $E_{F, redox}$ shown in **Fig. 1.5a**. At that instance forward and reverse currents balance each other, the arrows in **Fig 1.5a** represent equal charge transfer across the interface. Consider now the application of bias potential across the interface. The biasing can be reverse or forward. Both of the situations are displayed in **Fig.1.5**. Under reverse biasing **Fig 1.5b**, band bending increases and current flows due to minority carriers. Similarly under forward biasing, **Fig 1.5c**, the band bending decreases and current flows due to majority carriers. [25]
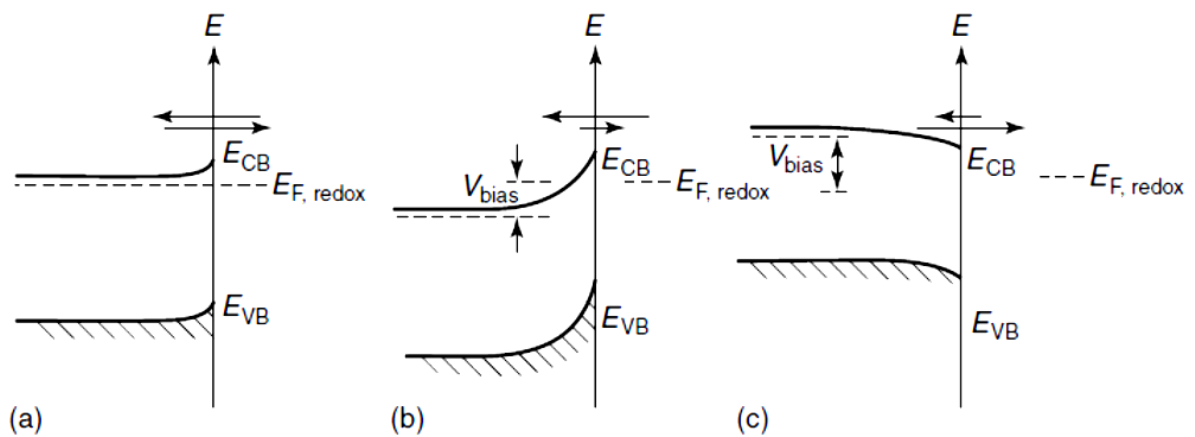
Fig.1. 5 Semiconductor/liquid interface at (a) equilibrium, (b) reverse biasing, (c) forward biasing.[22a]

The charge transfer process under forward and reverse biasing can be understood in terms of electron or hole exchange with the solution species under dark. **Fig. 1.6** presents these phenomena in a simple way;
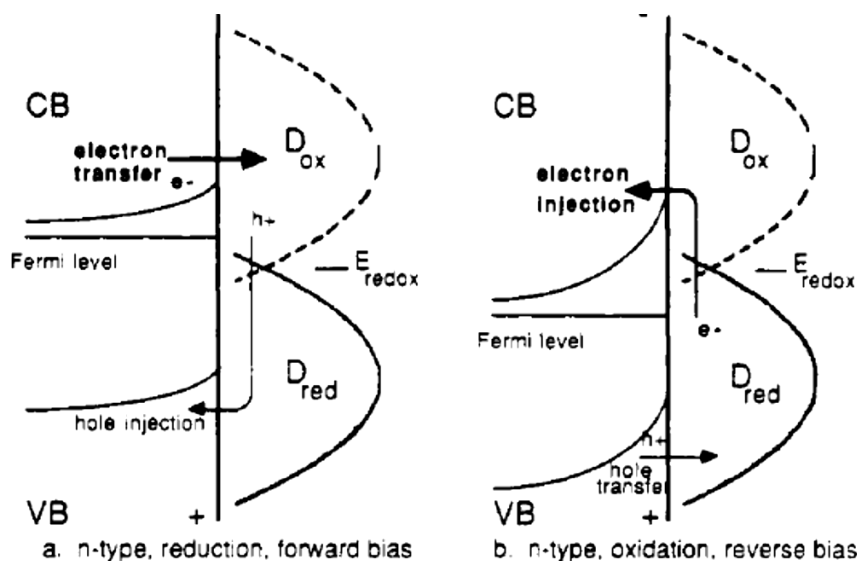
Fig.1. 6 Reduction and Oxidation at the interface under applied biasing. [25]

In **Fig. 1.6a** under forward bias the net cathodic current can result from electron transfer from the CB to an oxidized molecule or by injection of a hole from the molecule into the VB. Similarly, under reverse bias the net anodic current can be resulted by hole transfer from the VB to a reduced molecule or electron injection from a molecule to the CB. In the preceding section we may assume that all of the applied potential drops across the space charge layer i.e there is no potential drop across Helmholtz layer. In other words, the interface is in depletion conditions. Intuitively, this situation reveals the band edges are pinned and there is no Fermi level pinning. [22a] At more negative applied potentials for n-type semiconductors, majority carriers accumulate at the surface, on the other hand for n-type electrodes for more positive biasing the conditions of extreme depletion or carrier inversion exist. Current flow is usually irreproducible in these situations and likely to be dominated by tunneling processes through the Helmholtz layer. Moreover, it should be noted that the Helmholtz potential strictly depends upon the applied biasing voltage. This dependence becomes negligible when C_{SC} is much smaller than C_H that is, the semiconductor is depleted ($N_{adsorbed} \gg N_D$). Therefore, in case of depleted semiconductor all applied potential will be dropped across the semiconductor and V_H will be unaffected due to the assumption $C_{sc} \ll C_H$. The depletion region condition is by far the most important parameter to be considered in photoelectrochemical measurements related to the charge transfer whereas information related to the conduction band can be found in accumulation region. [11, 25, 22a, 26]

1.4. N–type semiconductor under light irradiation and biasing

The bandgap of a semiconductor is the energy difference between its CBM (conduction band minimum) and VBM (valence band maximum). The CB and the VB for an ideal semiconductor can be defined as; the maximum reduction power of excited electrons and the maximum oxidization power of photogenerated holes, respectively.[24] The optical bandgap (E_g) of a semiconductor defines its light absorption behavior. For a direct transition a photon having energy $hv > E_g$ absorbed by the semiconductor results in a transition by which an electron from the VB jumps to the CB.[27] The optical transitions are of two types "Direct and Indirect" transitions. In the direct transition, the momentum is conserved and the top of VB and bottom of CB are located at k = 0 (k is electron wave vector). The indirect transition involves phonon modes and the value of k ≠ 0. A given material can exhibit a direct or indirect band-band transition depending on its crystalline structure. It should be remarked that the light absorption depth (1/α) for direct and indirect transitions are vastly different. For direct transition the absorption depth span 10-100 nm range while for indirect transition it may be as large as 10^4 nm.[28] Optical transition in semiconductor can also involve localized states within the band gap. For nanocrytalline semiconductor these sub-band transitions can be probed with photon having energy less than the band gap. For an n-type semiconductor, photon having energy $hv > E_g$ incident on the semiconductor, excites the electron from the VB to the CB, the photogenerated electron is driven to the counter electrode/liquid interface while the holes generated within the diffusion length transfers to the semiconductor/electrolyte interface.[27] The photogenerated electrons reduce the electrolyte species at the counter electrode whereas photogenerated holes oxidize the solution species at the semiconductor surface. Under intense light irradiation sufficient carriers are photogenerated resulting in decreasing the band bending and further increasing light intensity can flatten the band bending. Interestingly, varying light intensity for higher values can predict the flat band of the semiconductor and it is a widely used technique for the prediction of the flat band position. In this technique, the open circuit potential can be plotted against the varying light intensity, the potential at which the open circuit potential does not change further is the flat band potential of the semiconductor under stake.[20] An important parameter of a semiconductor that should be considered for photoelectrochemical applications is its bulk Fermi level. If the bulk Fermi level is higher than the counter electrode Fermi level the electrons from the conduction band of the semiconductor will flow through the counter electrode to the solution which will initiate the reduction at the electrode/electrolyte interface.

Similarly, if the valence band edge is lower than oxidizing potential of the solution the holes will accept the electrons from the solution and Oxidation will begin at semiconductor/liquid interface. **Fig. 1.7** depicts the above situation for an n-type semiconductor under illumination with and without any external bias.[26a]
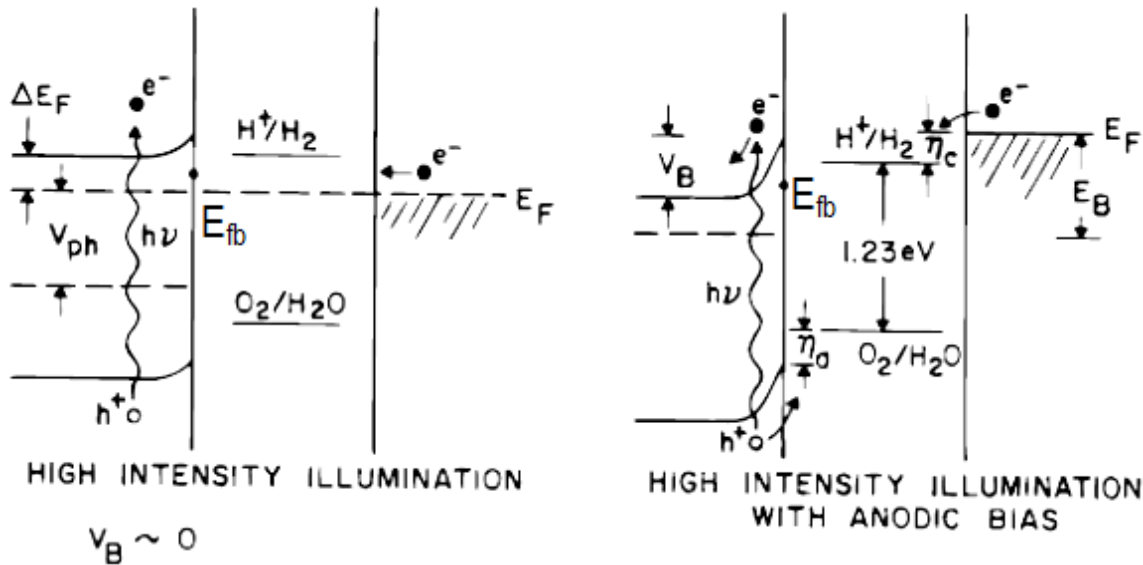
Fig.1. 7 n–type semiconductor in dark and under light irradiation. [26a]

The oxidation and reduction w.r.t to the redox potentials of H_2O are depicted along with energy level diagram of the semiconductor. If E_{fb} is below H^+/H_2 potential, even sufficient light intensity would not initiate the reduction of H^+. The external bias provides the overvoltage at the metal cathode; in addition, it will elevate the E_f of the counter electrode which then sustain the current flow and maintains the charge separation driven by electric field by increasing the band bending. Further the E_{fb} lies below the H^+/H_2 level, the greater would be the external bias. Biasing can be provided either by external power source or by immersing semiconductor into basic solution and counter electrode into the acidic solution. [26a.] As an example, a simplified mechanism explained above for photoelectrolysis of water without any external can be visualized in **Fig. 1.8** for $SrTiO_3$ for which the E_{fb} position is appropriate. UV light is irradiated on the $SrTiO_3$–electrolyte interface that excites electron from VB to CB of the semiconductor. E_{fb} of the semiconductor is appropriate enough that the photoexcited electron will pass through a relatively lower energy barrier to reduce the water on the counter electrode.
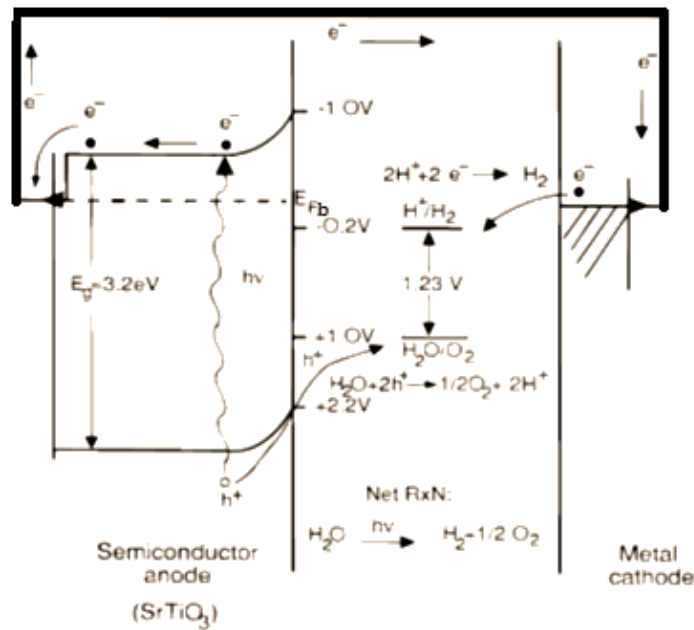
Fig.1. 8 Energy level diagram for the photoelectrolysis of water proceeded without external biasing by using $SrTiO_3$.[26a]

1.5. Photoelectrolysis and surface states

The solid-state properties of a semiconductor are generally modeled by the band theory where VB and CB are separated by a forbidden region; the band gap. At the interface of the solid with a solution, the crystal structure is physically and chemically different than within the bulk. These inhomogeneities can produce discrete energy levels within the band gap. [29,30,31] These intermediate levels may be derived from the "dangling bonds" of unfilled valencies on surface atoms, defects in the crystal structure, formation of oxide layers, adsorbed chemical species or heterogeneity caused by different exposed crystalline planes. [25] These states may mediate charge transfer, provide recombination centers, and allow applied potential drop to occur at the surface rather than the space-charge region. Unfortunately, quantitative determination of these states and understanding their precise nature is complicated and the data is usually open to various interpretations. However, there have been numerous reports on quantifying and identifying these states employing variety of techniques including photocurrent transient,[32] dynamic PEC measurements,[33] impedance spectroscopy,[34] photoluminescence [35]. As an example, for nano-structured TiO_2 these states are associated with low coordinated Ti sites,[36,37,38] grain boundaries,[39] oxygen vacancies.[40] For hematite they are proposed to be Fe^{III}–OH/Fe^{IV}=O [41] and for GaN they are related to the morphology.[42] The presence of these levels limits theoretical treatments of the electrochemical systems due to

significant contributions from intermediate processes. It is therefore desirable to circumvent these levels within the system for the fundamental analyses of the semiconductor/liquid interface. Nevertheless, the situation becomes more complicated when semiconductor is illuminated. [34] For some materials they act as current charge-transfer pathway [43] and for others; recombination centers.[41] However, the exact nature of these states remains controversial.

As an example; consider TiO_2 –electrolyte interface for which the surface states level is located close to the H_2O/O_2 redox level, (**Fig. 1.9**); where E_t represents the surface states potential. [43] In the far left of the **Fig. 1.9**, the Fermi level E_{Fs} of the semiconductor before contact with the electrolyte is assumed to be pinned to the surface states level E_t. These are the preexisting surface states, presenting equilibrium between the surface states and semiconductor bulk. Upon contact with the electrolyte (**Fig. 1.9** (middle)) the semiconductor Fermi level is released from the pinning. It is expected that the surface states can be significantly occupied by electrons in the electrolyte, while the band bending in the surface barrier region of the semiconductor is small. For far right figure, the whole of a bias voltage appears across the semiconductor space-charge region.
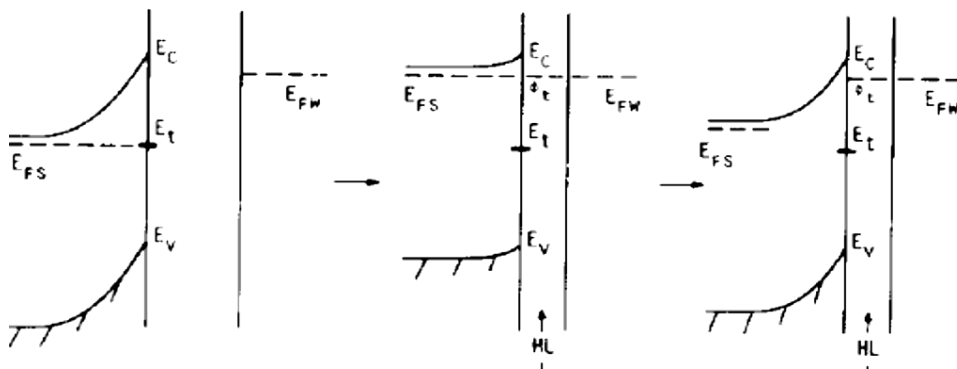
Fig.1. 9 Role of surface states for TiO_2-liquid interface. HL represents Helmholtz layer. [43]

The hole emission from the surface states to the VB can be neglected, it follows that all holes reaching the semiconductor surface are captured by the surface states and then tunnel through the Helmholtz layer with higher transfer probability; since E_t (2.3 eV from VB) for TiO_2 is located close to the H_2O/O_2 redox level (1.8 eV from VB), as a result the E_{fw} (water femi level) will be close to the E_t and hence surface states are proposed to act as current flow sites for holes.[43]

In case of Hematite surface states acted as a recombination centers. [34, 44] Proposed physical model for the charge carriers' dynamics, showing their generation, G, by light

absorption, surface state trapping, and interfacial charge-transfer reactions is presented in **Fig 1. 10**. [45] The central role of a surface state in Hematite is to act as a recombination center that affects the charge transfer of holes to the donor species in electrolyte.[34]
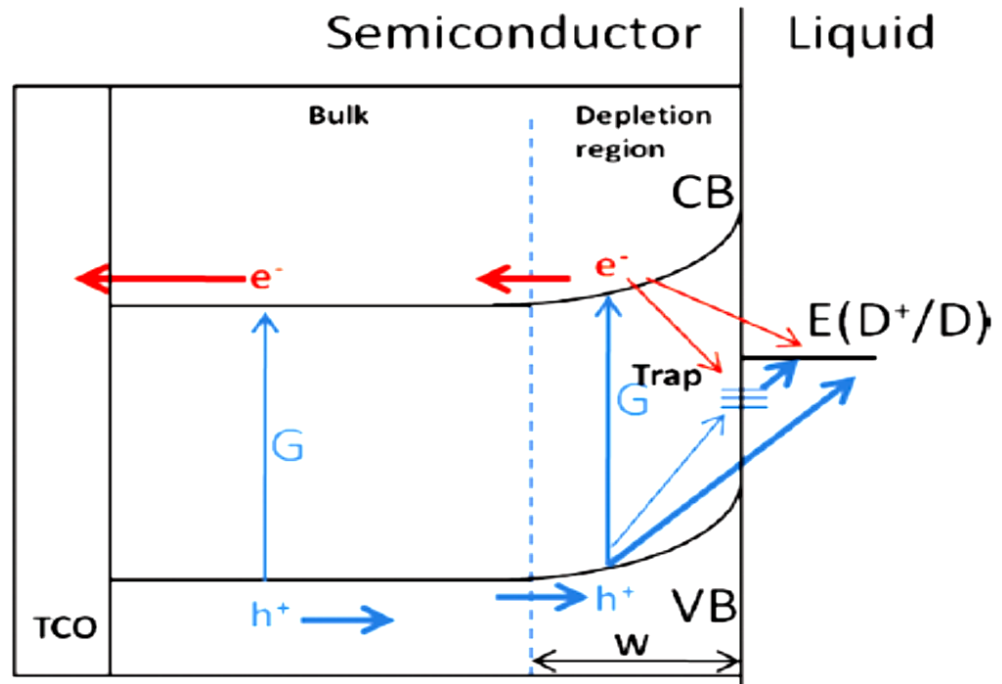
Fig.1. 10 Role of surface states in Hematite/liquid interface. [34]

Fig. 1.11 presents a general photoelectrochemical process governed by intermediate states under illuminated n-type photoanode. The possible mechanism for the charge transfer mediated by the surface states can be understood. The photogenerated electron jumps to the CB and due to the presence of intermediate states the hole is trapped in the surface states (E_{ss}).
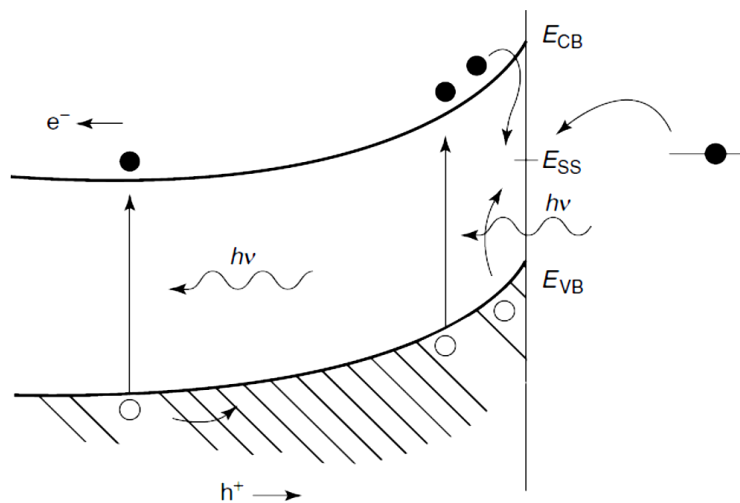
Fig.1. 11 Recombination and charge transfer via surface states.[22a]

If the position of E_{ss} is adequate as shown in **Fig. 1.10** the electron from the solution species will reduce that hole. Otherwise, electrons from the CB will recombine to reduce the trapped hole as a result such type of trap levels would be harmful for photoelectrochemical reactions.

1.6. Photoelectrochemical water splitting

"Yes my friends, I believe that water will one day be employed as fuel, that hydrogen and oxygen which constitute it, used singly or together, will furnish an inexhaustible source of heat and light, of an intensity of which coal is not capable.... When the deposits of coal are exhausted we shall heat and warm ourselves with water. Water will be the coal of the future."

— Jules Verne, *The Mysterious Island* (1874–5)

They call it water, we call it a fuel. God make it, we break it.

Every language has a word for water; no living thing exists without water. It soothes the spirit, its beauty inspires art and music. Salty or fresh, it's everywhere – falling from the skies, rushing to the sea, lapping the shores, deep within the Earth. It cycles from the air to the land to the sea and back again. Simply, water is life. Humans put water to hundreds of purposes, raising animals and crops, generating power, keeping lawns green. There is no life without water.

It has been discussed earlier in this chapter that using sunlight for water splitting in order to produce hydrogen has a potential to fulfill the modern civilization demands for clean energy. In this context, the development of an efficient and cost-effective photoelectrolysis of water into hydrogen and oxygen using sunlight has been the goal of many researchers since the early 1970s. [46] The net electrically assisted water splitting reaction can be written as follows;

$$H_2O \ (liquid \ or \ vapor) + \ electrical \ energy \ \rightarrow H_2(g) + \frac{1}{2}O_2(g) \qquad (1.6)$$
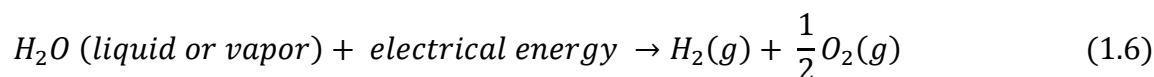
Under standard temperature pressure (STP), the change in the Gibb´s free energy for water splitting is positive. For the reaction to occur external energy should be provided which would be equal to the difference of the Gibb´s free energy. The minimum potential difference, derived from that difference for water splitting is equal to 1.23 V. Therefore, in an

electrocatalytic system a minimum of 1.23 V should be applied across the electrodes in order to split water into hydrogen and oxygen. In an electrochemical system, generally three electrodes configuration is used to split water (Section. 1.1). In the current work we used Ag/AgCl as a reference electrode. For the sake of ease we converted the Ag/AgCl potential into reversible hydrogen electrode (RHE). According to RHE scale, water reduction occurs at 0 V vs RHE and oxidation occurs at 1.23 V vs RHE which is independent of pH of the aqueous solution. The well-known Nernst equation provides the conversion of Ag/AgCl reference electrode to RHE which is as follows;

$$V_{RHE} = V_{Ag/AgCl} + (0.059) \times pH + 0.197 \text{ V} \quad (1.7)$$

As mentioned earlier, the production of clean energy demands the synthesis of hydrogen from a clean source and in case of pure electrolysis we need electric energy that definitely is not be a good choice. Therefore, we should use a photoelectrochemical system that utilizes the sunlight by decreasing the need of external electric energy for the water splitting reaction or even replacing completely the electric energy input with the sunlight. An efficient solar harvesting photoelectrochemical system would be the one which uses the electric energy as lowest as possible. To date, the photoelectrochemical systems used for the water splitting have been inspired from the earlier work of Honda and Fujishima. In their photoelectrochemical system the water splitting was stimulated by using semiconductor (TiO$_2$) / liquid junction under UV-radiation.[46] The simplest description of photoelectrochemical water splitting using an n-type semiconductor is as follows; under irradiation with the energy greater than the bandgap of the semiconductor photoanode, electrons of the VB are excited into the CB. The electric-field at the depletion region separates the photogenerated electrons-holes pair and its direction is such that the holes migrate to the interface where they oxidize water to oxygen and on the other hand the photogenerated electrons reduce water to hydrogen. To achieve the overall water splitting the energy requirements imposes some limitations on the optical window of the semiconductor; such as the CBM must be located at more negative potentials than the reduction potential of water or hydrogen ion (0 V vs RHE) and VBM must be positioned more positive than the oxidation potential of water (1.23 V vs RHE). In other words, water oxidation and reduction potentials should be sandwiched between the CBM and VBM of the semiconductor. Theoretical value of the photon energy for water splitting is 1.23 eV (1010 nm) indicating that visible light possesses enough energy for water decomposition. For photoelectrochemical

water splitting, the photoelectrode is the main component of the cell; it´s material and structure play critical roles in the device performance. There are many oxides and non-oxide semiconductors that fulfill the condition of straddling the oxidation and reduction of water in the bandgap. Besides bandgap, a key challenge in photoelectrochemical solar conversion is the stability at the reactive electrolyte interface.[2][23] An ideal semiconductor would be the one that resists the chemical degradation by electrochemical corrosion; photo-corrosion etc. [47] **Fig. 1.12** displays bandgap and band edges of some photoelctrodes w.r.t normal hydrogen electrode (NHE) along with water oxidation/reduction potentials
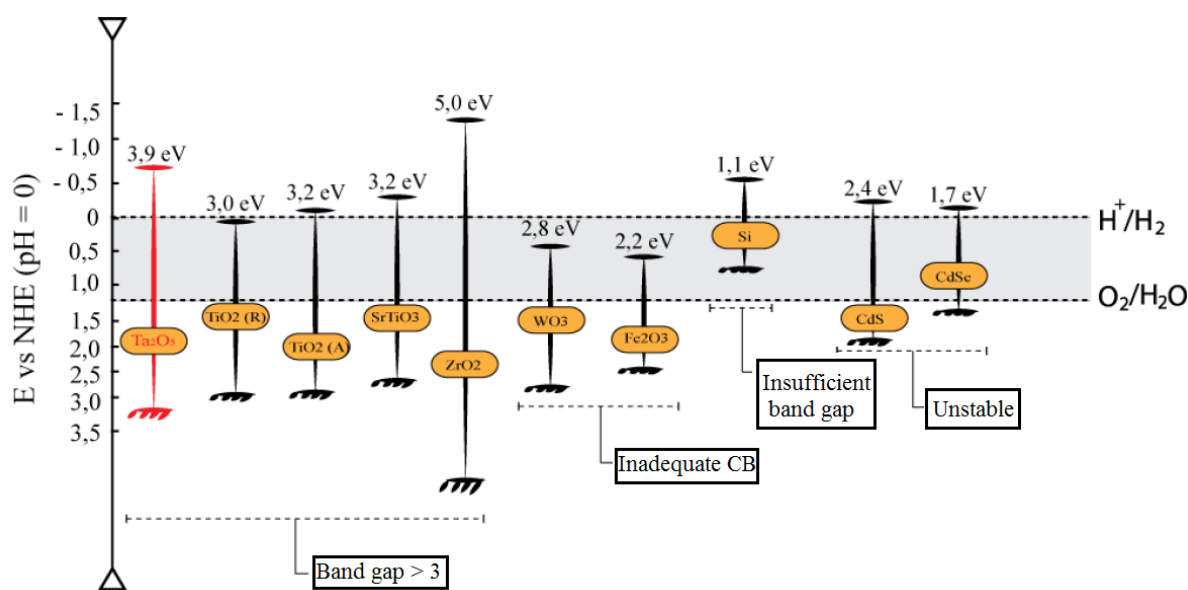
Fig.1. 12 Band gap energies of some selected semiconductors. [48]

It can be seen that many of them sandwich the water oxidation/reduction potentials like TiO_2, ZrO_2, $SrTiO_3$ and Ta_2O_5; unfortunately, they are active only in UV region. However, Fe_2O_3 (Hematite), WO_3 etc cannot reduce water due to inappropriate band edges. Besides, CdS, CdSe are unstable in aqueous solution.

Apart from improving the electronic properties of a semiconductor, nanostructuring can benefit to lessen the distance that minority carriers have to travel toward the reactive site i.e increasing the active surface area. Aside from lessening these distances, it can help separating the photogenerated e^-–h^+ pairs. Therefore, nanostructuring enhances the photoelectrochemical activity of the applied photoelctrodes. [23] Among many nanostructures, NTs have been studied widely for photoelectrochemical applications. [49] The vertically oriented nature and higher surface area of the NTs offer high charge transportation to the

collecting electrode. Therefore, a visible light driven semiconductor that is nanostuctured in the form of NTs would be a great choice for photoelctrochemical applications. [50]

1.7. Ta_3N_5 Photoanode

In Section. 1.6 we described the photoelectrochemical water splitting and some bandgap limitations for a semiconductor to be utilized for photoelectrolysis. Several oxide semiconductors such as $SrTiO_3$, $KTaO_3$, and ZrO_2 have E_{fb} above the H^+/H^2 potential. Unfortunately, oxides have large band gaps (3.4–3.5 eV), result of that is very low solar absorptivity; hence, they are inefficient (<1%) in systems for solar energy conversion. [26a] Therefore, strategies are needed to fine tune the energetics of oxide semiconductors for visible light activation. As an example, we have observed in **Fig. 1.12**, semiconductor like TiO_2 straddle the water oxidation/reduction potential. TiO_2 has a bandgap of 3.0 eV therefore; it would be activated in UV region (4% of solar spectrum) of the electromagnetic spectrum. Similarly, other oxide semiconductors such as Ta_2O_5 present wide bandgaps that make them active only within the UV region. Therefore, these semiconductors are not ideal for solar applications because the photoanode should absorb a wide range of visible light and contain appropriate band edges w.r.t water oxidation and reduction potentials. An ideal semiconductor material for the photoelectrode should have a band gap large enough (> 1.6 eV) to split water and, at the same time, small enough (< 2.2 eV) to absorb a wide range of the solar spectrum and lastly, the semiconductor should be stable. In this regard, several efforts have been made to fine tune the bandgap of oxide semiconductors so that it can absorb visible light and can be used as a photoanode for photoelectrochemical water splitting. One reason for the wide band gap of metal oxides is the composition of VBM which is O2p orbitals. An interesting way to narrow the oxide band gap for visible light response is to hybridize the O2p orbitals with N2p orbitals e.g. doping TiO_2 with nitrogen (N).[51] This approach would move up the VBM due to the O^{2-} substitution with N^{3-} and material would be responsive under visible light irradiation. Moreover, the oxidation-reduction of H^+/H_2 (0 Vs RHE) and O_2/H_2O (1.23 V vs RHE) must be straddled within the band gap of the semiconductor.

Among many nitrides, Ta_3N_5 has emerged as a promising photoelectrode candidate for PEC water splitting in recent years. Its band gap is 2.1 eV and it absorbs light up to ~ 600 nm. Theoretical value of STH (solar to hydrogen) efficiency is 15.9% at AM 1.5G illumination. [52] The isoelectric point for Ta_3N_5 has been found to be at pH 1. Therefore, it can be utilized above pH 1 for PEC applications.[41] Energy level diagram of Ta_3N_5 is shown in **Fig. 1.13**.
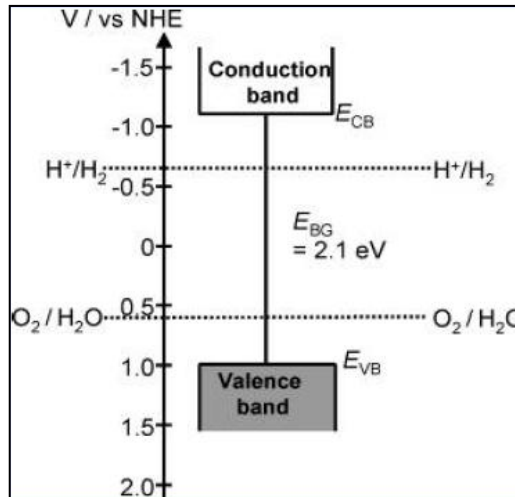
Fig.1. 13 Band positions of Ta_3N_5 estimated at pH (11). [53]

Clearly, water redox potentials are straddled in the bandgap of Ta_3N_5 and this semiconductor is capable of generating H_2 and O_2 from H_2O. **Table 1.1** summarizes the flat band potential of Ta_3N_5 photoelectrodes with different morphologies that clearly presents the ideal flat band positions of Ta_3N_5 photoelectrodes for water splitting applications. In addition, the flat band positions seem to be independent of morphology of Ta_3N_5.

Table 1. 1 Reported values of the flat band potential of some Ta_3N_5 photoelectrodes.

Sample	Technique	Freq/Amp	Solution (pH)	E_{fb}	Ref
Drop coating film	Mott-Shottky	0.5kHz, 1kHz, 3kHz/5mV	0.1M Na_2SO_4 (11)	-0.95V vs Ag/AgCl	54
Nanotubes	Mott-Shottky	200Hz, 500Hz, 1000Hz/5mV	0.1M Na_2SO_4 (11)	-0.93V vs Ag/AgCl	13
RBD film	Mott-Shottky	500Hz, 1000Hz, 3000Hz/-	1M KOH (13.6)	-1.05V vs Ag/AgCl	55
Thermally grown film	Mott-Shottky	-	0.5M K_2SO_4 (13)	-1.0 V vs Ag/AgCl	56

For the formation of Ta_3N_5 a precursor of Ta_2O_5 or $TaCl_5$ is heated under NH_3 flow (generally, Ta_2O_5 is the starting material). From Ta_2O_5 it is transformed to Ta_3N_5 by the following reaction scheme;[57]

$$\frac{3}{2} Ta_2O_5 + 5\,NH_3 \rightarrow Ta_3N_5 + \frac{15}{2} H_2O$$
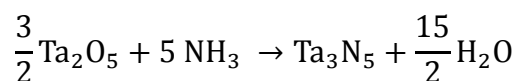
The ammonothermal conditions (temperature, NH_3 flow rate, and heat treatment time) define the phase transformation. Mild condition nitridation forms TaON, severe condition produces Ta_3N_5. It is widely accepted that upon heating under ammonia environment T_2O_5 is transformed to TaON followed by Ta_3N_5:[58]

$$Ta_2O_5 \rightarrow TaON \rightarrow Ta_3N_5$$

Under extreme conditions Ta_3N_5 decomposes into other nitride phases which are as follows:

$$Ta_3N_5 \rightarrow Ta_4N_5 \rightarrow Ta_5N_6 (\rightarrow TaN \rightarrow Ta_2N)$$
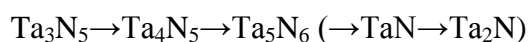
The N/Ta ratio decreases as $1.67 \rightarrow 1.35 \rightarrow 1.2$ and valence of Ta ions decreases from $+5 \rightarrow +4 \rightarrow +3$. The nitridation progresses from the surface to the core of the Ta_2O_5 that probably forms lattice defects and grain boundaries due to the crystal structure from oxide to nitride transformation. Additionally, the covalent character generated by substituting O with N makes the lattice more rigid so defects formation is most likely to happen on the surface, until nitrogen diffuses to the bottom of Ta_2O_5. Similarly, long time heating forms N vacancies through thermal reduction of Ta_3N_5. [59] Using high pressure nitridation [60] for synthesizing Ta_3N_5 and/or incorporating suitable co-catalyst to Ta_3N_5 have been suggested to improve the photocatalytic activities of Ta_3N_5. [9]

1.7.1. Crystalline Structure of Ta_3N_5

The vermillion (red colored) Ta_3N_5 was synthesized by *H. Funk and H. Bohland* in 1964 by heating Ta_2O_5 powder under flowing NH_3. [61] In 1966, Ta_3N_5 was proposed to be tetragonal and diamagnetic having a density of 9.85 g.cm^{-3}. According to the literature, by heating Ta_3N_5 in vacuum it starts loosing nitrogen at 500°C and decomposes to TaN. [62]
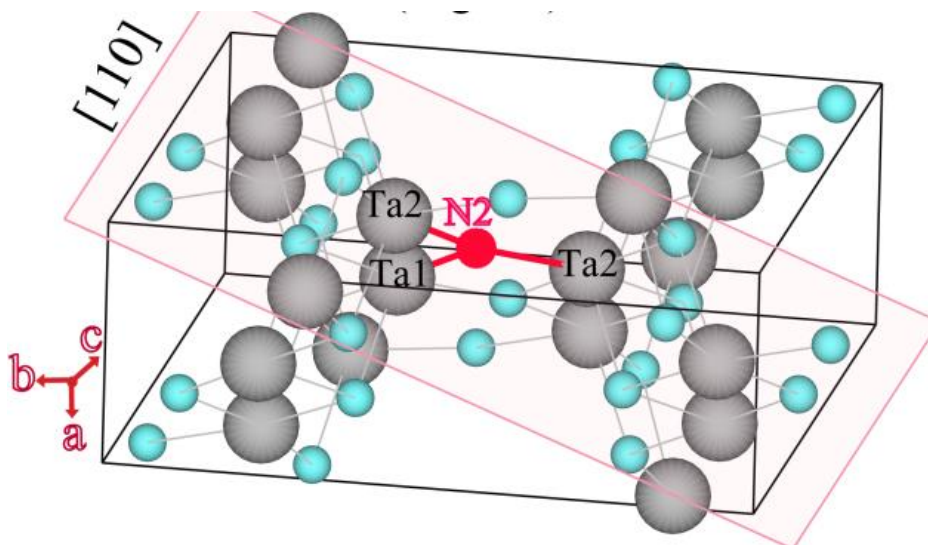
In 1973, Ta_3N_5 was proposed to be orthorhombic with a space group Cmcm. [63] Ta_3N_5 was synthesized by CVD (Chemical Vapor Deposition) and was suggested to be monoclinic and the resistivity of Ta_3N_5 was measured to be 6 Ω cm. [64] In 1977, space group C 2/m with monoclinic crystalline structure was introduced for Ta_3N_5. [65] In 1991, monoclinic transformation of orthorhombic model was applied but space group C2/m did not give better refinement statistically. Therefore, it was accepted that for Ta_3N_5 monoclinic and orthorhombic are too close to discern. The orthorhombic structure of Ta_3N_5 is composed of 5 atoms namely Ta(1), Ta(2), N(3),N(4) and N(5) with Wyckoff positions, 4(*c*), 8(*f*), 4(*c*), 8(*f*), and 8(*f*), respectively. Furthermore it consists of octahedral N atoms centered by Ta atoms. The octahedra are irregular because N atoms are three and four coordinated. The bond lengths are given in **Table. 1.2**. Both Ta atoms have six Ta–Ta contacts shorter than 3.8 Å (the next nearest neighbor distance). For tantalum based materials, the shortest Ta–Ta metal-metal bonds the distance is less than 3 Å; however, in case of oxynitrides or oxides that is almost 3.3 Å. In case of Ta_3N_5 it is 3.0 Å. [66]

Table 1. 2 Bond distances (in Å) and angles (in degree) for Ta_3N_5. [51]

Ta(1)—2Ta(2)	3·2353 (8)	Ta(2)—N(4)	2·0388 (9)
Ta(1)—4Ta(2)	3·2513 (7)	Ta(2)—2N(5)	2·0335 (3)
Ta(1)—2N(3)	2·0571 (5)	Ta(2)—N(5)	2·240 (1)
Ta(1)—2N(4)	2·035 (1)	N(3)—2Ta(1)	2·0571 (5)
Ta(1)—2N(5)	2·1372 (8)	N(3)—2Ta(2)	2·2203 (8)
Ta(2)—Ta(1)	3·2353 (8)	N(4)—Ta(1)	2·035 (1)
Ta(2)—2Ta(1)	3·2513 (7)	N(4)—Ta(2)	1·9550 (8)
Ta(2)—Ta(2)	3·004 (1)	N(4)—Ta(2)	2·0388 (9)
Ta(2)—2Ta(2)	3·287 (1)	N(5)—Ta(1)	2·1372 (8)
Ta(2)—N(3)	2·2203 (8)	N(5)—2Ta(2)	2·0335 (3)
Ta(2)—N(4)	1·9550 (8)	N(5)—Ta(2)	2·240 (1)
N(3)—Ta(1)—N(3)	141·67 (7)	N(4)—Ta(2)—N(5)	104·31 (3)
N(3)—Ta(1)—N(4)	104·31 (2)	N(4)—Ta(2)—N(5)	161·01 (4)
N(3)—Ta(1)—N(5)	79·93 (3)	N(5)—Ta(2)—N(5)	79·56 (3)
N(4)—Ta(1)—N(4)	82·30 (5)	N(5)—Ta(2)—N(5)	145·70 (5)
N(4)—Ta(1)—N(5)	81·05 (2)	Ta(1)—N(3)—Ta(1)	141·67 (7)
N(4)—Ta(1)—N(5)	163·35 (5)	Ta(1)—N(3)—Ta(2)	98·88 (1)
N(5)—Ta(1)—N(5)	115·60 (6)	Ta(2)—N(3)—Ta(2)	123·91 (5)
N(3)—Ta(2)—N(4)	99·55 (4)	Ta(1)—N(4)—Ta(2)	105·14 (4)
N(3)—Ta(2)—N(4)	177·96 (5)	Ta(1)—N(4)—Ta(2)	157·34 (4)
N(3)—Ta(2)—N(5)	78·48 (2)	Ta(2)—N(4)—Ta(2)	97·51 (4)
N(3)—Ta(2)—N(5)	99·44 (3)	Ta(1)—N(5)—Ta(2)	95·28 (4)
N(4)—Ta(2)—N(4)	82·49 (4)	Ta(1)—N(5)—Ta(2)	102·41 (2)
N(4)—Ta(2)—N(5)	78·52 (3)	Ta(2)—N(5)—Ta(2)	100·44 (3)
N(4)—Ta(2)—N(5)	101·06 (3)	Ta(2)—N(5)—Ta(2)	145·70 (5)

Fig. 1.14 displays the crystalline structure of Ta_3N_5 projected on (100).
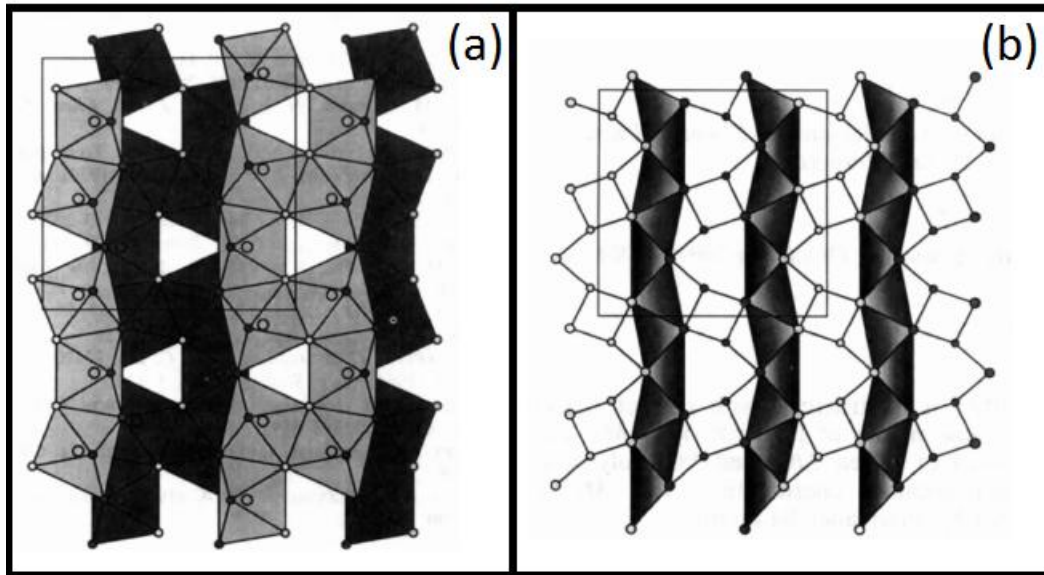
Fig.1. 14 Projection of Ta_3N_5 structure onto (100).(a) The b axis are horizontal and c axis are vertical. The dark shaded octahedral are displayed by a/2 from the lighter ones. Dark circles represent the four coordinated N atoms, while the lighter circles represent the three-coordinated N atoms. Larger circles represent Ta atoms within the octahedral. (b) Emphasizing anion coordination. The edge-sharing tetrahedral are centered by N atoms. The shading of the circles indicates displacement by a/2. [66]

1.7.2. Electronic structure of Ta_3N_5

In 2001, Fang et al used density functional theory (DFT) to study the electronic structure of Ta_3N_5. Orthorhombic Ta_3N_5 crystalline structure was used for the DFT calculations. It has been shown that the VB of Ta_3N_5 is mainly composed of N 2p states. The bottom of the CB is mainly composed of Ta 5d states. The density of Ta 5d is high all over the VB indicating a strong covalent interaction between Ta and N. The theoretically estimated direct and indirect band gaps for ideal Ta_3N_5 were 1.4 eV and 1.1 eV, respectively. However, experimentally the optical bandgap of Ta_3N_5 has been found to be 2.1 eV. [67] The reason to the discrepancy has been proposed to be the existence of oxygen content in Ta_3N_5 structure.[68]

1.7.3 Ta_3N_5 as a Photocatalyst

Ta_3N_5 was used as a visible light driven photocatalyst for the first time in 2003. It has been observed that Ta_3N_5 is better for oxidation of water as compared to the reduction in Photolysis system.[69] Later, while using Ta_3N_5 in Photolysis many efforts have been made to improve the water reduction as well as its oxidation ability by using different nanostructures and loading different cocatatlysts, etc. Ta_3N_5 semiconductor films as photoanode for photoelectrochemical water splitting were used for the first time in 2004.[53] Promising water splitting activities have been observed by using Ta_3N_5 as a catalyst in Photoelectrolysis. [7,8,10,70,71,72,73,74] Later, nanostructures of Ta_3N_5 like nanorods,[9] NTs,[13] nano-urchins,[10] have been reported as photoanodes for water oxidation. In recent years Domen´s group has presented the best PEC performance of Ta_3N_5 photoanodes by Ba doping resulting in to 1.5% solar energy conversion efficiency.[9] Based on the PEC results obtained by Ta_3N_5 it seems to be interesting to investigate the materials physico-chemical properties to fine-tune them for the improved PEC performance.

1.8 Anodization of tantalum

Anodization is an electrochemical process that produces a protective or decorative oxide layer on a metal. [75] Electrochemical anodization has proven to be a powerful tool to fabricate self-ordered oxide nanostructured patterns. To form different nano-architectures various metals such as Ti, Al, Ta have been anodized successfully.[76,77] Generally, anodization is performed in a two electrode configuration containing the oxide precursor metal as anode and Pt or Cu as cathode immersed in an electrolyte; all of them are mounted in a cell that is placed in an

ultrasound bath. A suitable DC voltage is applied across the two electrodes. The morphology, size and adherence of the anodized nano-structures can be controlled by tuning the electrolyte concentration and the type of species in the electrolyte, in addition to anodization time, applied voltage and temperature. [49, 78- 55]

In recent years Ta_2O_5 has emerged as a promising candidate for photocatalytic hydrogen production. Among many other nanostructures Ta_2O_5 nanotubes (NTs) synthesized by anodization have been studied extensively,[19, 42-46] as they present high aspect ratio (length to diameter) that makes them suitable for application in systems where favored electron flow across the nanostructure is an important factor.[79] Various reports have suggested the facile and controllable formation of highly ordered and vertically oriented NTs arrays of Ta_2O_5 over Tantalum foils immersed in organic and non-organic solutions. Recently, we have synthesized Ta_2O_5 NTs in a non-organic fluoride based electrolyte. [80 49] Generally, anodization is performed at potentials lower than the dielectric breakdown. The formation of NTs by anodization in fluoride based electrolyte is the result of three simultaneously occurring phenomena: (a) Field assisted oxidation of the metal to form the oxide (b) Field assisted dissolution of metal ions in the electrolyte and (c) Chemical etching of metal and its oxide by fluorine ions.[75] Typically, the anodization process can be monitored by using current density-time data for the given voltage as shown in **Fig. 1.15.** During anodization due to electrostatic field, the oxygen ions inside the solution migrate to the metal end and similarly metal ions migrate through the oxide layer towards the oxygen ion, where they react to form thicker oxide layer and hence the resistivity of the surface increases, that is why in the beginig large amount of current flows an then suddenly decays due to the formation of the oxide barrier on the metal.[79 81] In addition, flourine ions present in the electrolyte act as a drill for the oxide layer simultaniously with the formation of the oxide barrier due to electrochemical etching of the respective oxide layer. It is widely accepted that competition between oxide growth and dissolutions leads to the formation of porous oxide films.[7]
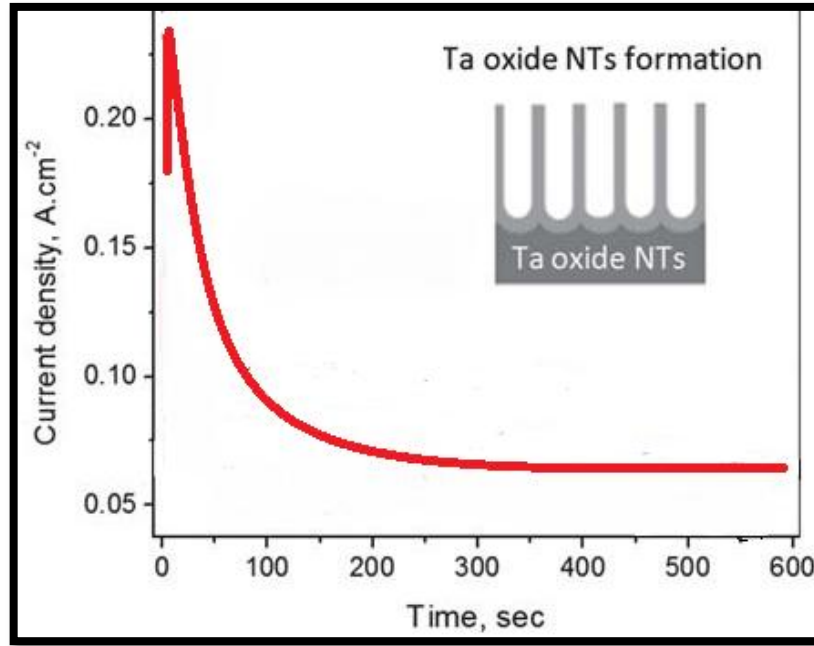
Fig.1. 15 Characteristic I-t anodization curve. [79]

Formation of Ta_2O_5 NTs in aqueous H_2SO_4/HF electrolyte follows two reaction schemes;

$$2Ta + 5H_2O \rightarrow Ta_2O_5 + 10H^+ + 10e^- \qquad (1.7)$$

$$Ta_2O_5 + 10H^+ + 14F^- \rightarrow 2[TaF_7]^{2-} + 5H_2O \qquad (1.8)$$
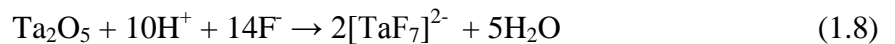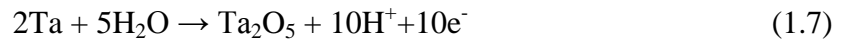
Reaction (1.7) is a pore based reaction where oxide film is thin enough for the applied field to traverse ions through it, while reaction (1.8) is the chemical dissolution occuring at the oxide surface (pore wall and pore base). The rate of Ta_2O_5 dissolution (reaction: 1.8) is expected to be much higher at the pore base versus the walls due to field focusing effect. Therefore, formation of high aspect ratio Ta_2O_5 NTs is related to the increase in dissolution rate of Ta_2O_5 at the pore base. **Fig. 1.16** shows the Ta_2O_5 NTs growth steps. The NTs grows from top to the bottom. In the first stage of anodization Ta_2O_5 grows on Ta without any significant fluoride incorporation. After some time, fluoride incorporation starts at oxide/solution interface and moves toward the Ta/Ta oxide interface. The incorporation of fluorine ions on the oxide layer forms localized dissolution of the oxide film as a result pits are generated on the oxide top surface.
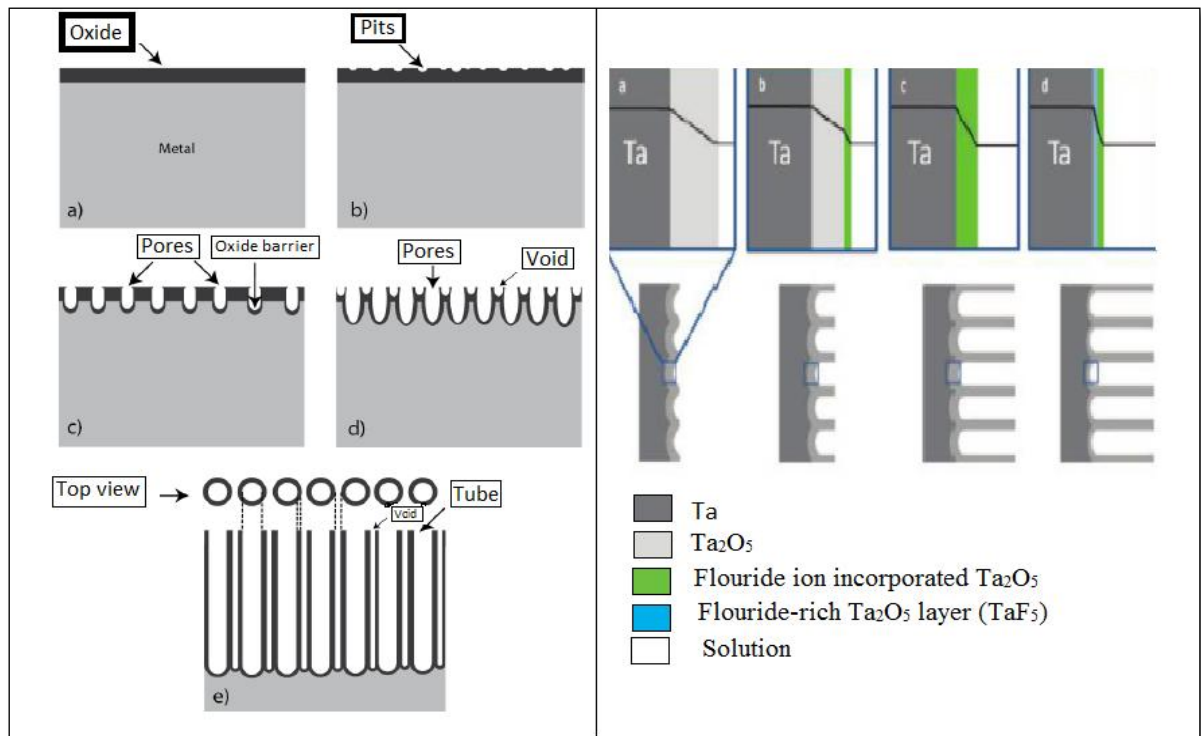
Fig.1. 16 Growth of Ta$_2$O$_5$ NTs via electrochemical Anodization. [77,75]

These pits grow further into scallop shaped pores. The pores grow deeper and electric field increases inside the pores which increases the oxide growth and oxide dissolution. Therefore, along with well-defined pores voids start growing. For further anodization time Ta$_2$O$_5$ layer becomes fully incorporated with fluorine ions. Now, voids and tubes grow in equilibrium. The NTs length increases if the electrochemical etch rate is equal to the chemical dissolution rate of the NTs top surface. In the next stage fluorine ions start to accumulate and form a TaF$_5$ layer at Ta/Ta oxide interface. For long anodization times the oxide film detaches from the substrate and a thin fluoride-rich layer (TaF$_5$) remains on the substrate surface. [77] To avoid the detachment of Ta$_2$O$_5$ NTs membrane, the anodization can be carried out in low concentration HF solution and low temperature. We have observed that the adherence of Ta$_2$O$_5$ NTs increases upon decreasing the electrolyte temperature. Therefore, anodizing Ta in low temperature produces adhered NTs that can be used as a phtoanode for photoelectrochemical applications. Furthermore, high temperature anodization produces free standing NTs membrane that can be used in Photolysis. [77] [75] Thus, anodization is a robust way to control the thickness, length, pore diameter and adherence of the NTs on the Ta substrate.

1.8.1. Ta_3N_5 nanotubes

The as-anodized Ta_2O_5 NTs are always amorphous. Therefore, annealing must be performed to crystallize them. However, to obtain Ta_3N_5 NTs, the as anodized Ta_2O_5 NTs are doped with nitrogen by replacing the oxygen in the Ta_2O_5 NTs lattice. Doping oxide NTs into nitride NTs can be performed by annealing Ta_2O_5 NTs in NH_3 environment. This process provides crystallization and phase transformation simultaneously. To date, there have been few reports on the synthesis of Ta_3N_5 NTs for photoelectrochemical water splitting.[17, 14] Ta_3N_5 NTs have been synthesized at 800°C for 3 hours [13] and 700°C for 10 hours.[12] At what temperature Ta_2O_5 NTs transforms to Ta_3N_5 and what could be the optimum annealing condition to obtain highly nanocrystalline Ta_3N_5 NTs are of great interest for enhancing water splitting activity. In this context, a detailed study for the phase transformation and crystallization for Ta_3N_5 NTs is warranted. In the current work we have comprehensively studied different nitridation conditions to obtain Ta_3N_5 NTs photoanodes that can be utilized in PEC cells.

CHAPTER 2
EXPERIMENTAL METHODS

2.1. Reagents

To clean the samples and reactors, isopropanol, (F. Maia Industry and Trade LTD, 99.5% min), acetone and distilled water were used. For Anodization, Ta foil was purchased from Alfa Aesar, (purity 99.95%) with dimensions 200 mm × 200 mm × 0.25 mm. H_2SO_4 (95.0 to 98.0%) and HF (38.0 to 42.0%) were purchased from Lab-Synth Products Laboratory LTD, and Modern Chemical Industry and Trade LTD, respectively. For photoelectrochemical measurements Na_2SO_4 (99.0% min), $K_3Fe(CN)_6/K_4Fe(CN)_6$, were purchased from F. Maia Industry and Trade LTD, Merck's Reagenzien, respectively. For phosphate buffer solutions; Na_2HPO_4 (99.0% min), NaH_2PO_4 (99.0%) and NaOH (98.0% min) were purchased from Sigma Aldrich. All of the reagents were analytical graded and used as received without further purification.

2.2. Anodization of Ta

For the anodization Ta foil was cut into 2 cm × 2 cm pieces and a modified way was used to clean the Ta substrate because we observed that the adherence of NTs is very sensitive to the cleaning process of the Ta foil. Firstly, the Ta discs were mechanically polished on both sides by (Pantec, poliplan 2) using silicon carbide adhesive paper. The mirror like Ta discs were soaked in HF (40%) for 1 min rinsed with water and after cleaned in distilled water mixed with detergent for 1 hour in ultrasound. After the Ta discs were again ultrasonically cleaned in Isopropanol and distilled water for 30 min. The ultraclean discs were removed from the ultrasound bath and immediately dried under nitrogen flow and then loaded to the home made Teflon reactor that was immersed in a mixed solution of H_2SO_4 + 1 vol% of HF and 4 vol% of distilled water and anodized in a conventional two electrode configuration cell.[49] The temperature was kept constant by immersing the reactor in a homemade Teflon cup with water circulation controlled by a Thermo Neslab-RTE7 (Electron Corp.). The anodization was carried out for 50 V fixed DC voltage by ramping the voltage from 1 to 50 V/s for different anodization times (5–20 min) under a temperature of 10°C. A polished Cu disc was used as cathode. The distance between the anode and cathode was maintained fixed at 1 cm. Both electrodes were connected to a DC power supply. The anodization I–V curves were monitored by the software (Ideial, Dalton Vidor) incorporated with the DC power supply. After anodization, the samples were removed from the reactor, the excess of acid residue from the

sample was removed by rinsing it with distilled water. The Anodization set up is shown in **Fig. 2.1** that consists of home-made Teflon reactor for the electrodes and Teflon cup having the water circulating facility, ultrasound bath, DC power supply and software controlled digital setup.
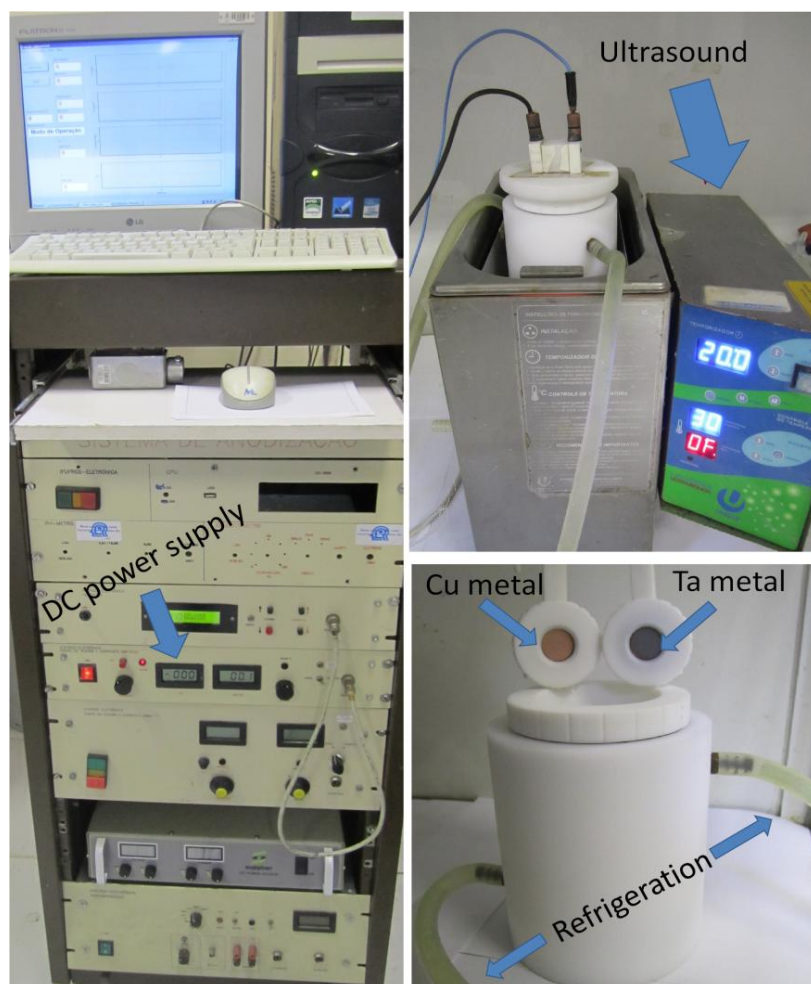
Fig.2. 1 Anodization setup used in the current study; comprising of DC power supply, homemade Teflon reactor having refrigeration facility, sonication bath and digital system to monitor and control the anodization parameters.

2.3 Preparation of Ta_2O_5 Thin films by magnetron sputtering

Prior to the film deposition, quartz, Si and Ti substrates were cleaned by sequential sonication for 30 min each in detergent mixed distilled water and isopropyl alcohol, rinsed with water and then dried under nitrogen flux. Thin films of Ta_2O_5 were sputtered on the substrates by using radio frequency magnetron sputtering (AJA ORION, 8- See **Fig. 2.2**) technique. The sputtering target consisted of 50.8 mm (2.0 in) diameter Ta_2O_5 (99.95% purity, AJA

International, Inc). The base pressure of the sputtering chamber was 3.2×10^{-11} mbar. The argon flow rate was 20 sccm such that the chamber pressure was maintained at 2.6×10^{-3} mbar during the sputtering process. The substrate temperature was kept 21 °C and RF power of 150 W with DC self-bias voltage around 2–10 V was used for deposition. The distance between the target and substrate was kept at 14.7 cm and the substrate holder was rotated at a frequency of 20 rpm. Before the deposition process, a pre-sputtering of 5 min was made to clean the target and afterwards the films were deposited for a deposition time of 300 min. The sputtering rate was 3 nm min^{-1}

Fig.2. 2 AJA Orion 8 sputtering system used to deposit thin films.

2.3 Nitridation process

Prior to nitridation, the as-anodized samples were etched in HF: H_2O (1: 9 vol/vol) for few seconds and subsequently rinsed with water and dried under nitrogen flux. For nitridation

process the samples were placed first on an alumina boat and then inserted into a quartz tube at the middle of the furnace and the flux of the gas was kept as 100 mL min^{-1}. Nitridation was carried out at temperatures ranging from 650–1000 °C for time of 1–10 h. A special gas mixture of NH_3:Ar in a volume ratio of (1:9) was used as a reaction gas. The pressure of the gas from the cylinder was kept at 5 bar (500 kPa). For all samples the heating and cooling rates of the furnace were maintained at 5°C/min under ammonia flow. A glass flow meter was used to estimate the flow rate of NH_3. The ammonia gas was allowed to enter from one side of the tube, after passing through the tube it was bubbled into aqueous HCl solution that neutralizes the gas and further the gas was allowed to exhaust in the environment. To synthesize Ta_3N_5 thin films nitridation was carried out at 900°C for 24 h. The nitridation set-up is shown in the **Fig. 2.3.**
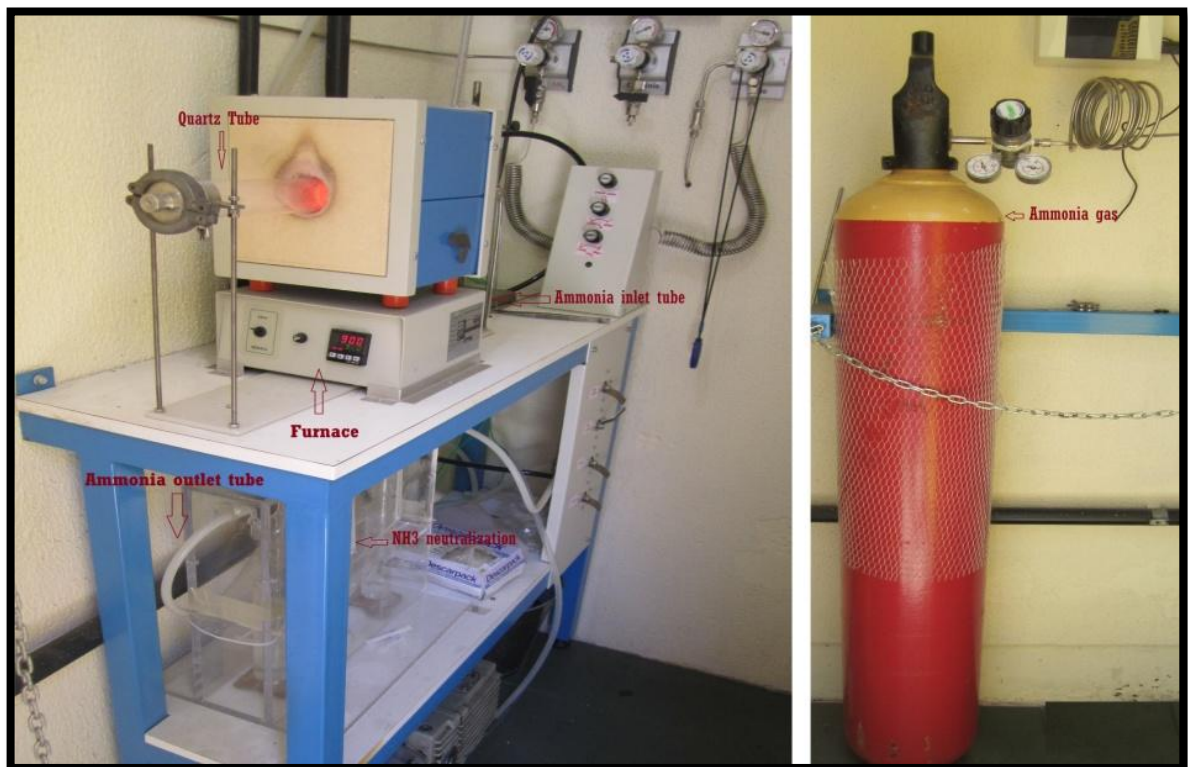
Fig.2. 3 Nitridation setup comprising of quartz tube furnace, flow meter, ammonia cylinder and ammonia neutralization chamber. Once the gas was neutralized; the gas flow was measured from the outlet valve by using glass flow meter.

2.4. Electrochemical and Photoelectrochemical measurements

2.4.1 Thin films

For Ta_3N_5 thin films four types of samples were prepared using different substrates; $Ta_3N_5/Pt/Ti/quartz$, $Ta_3N_5/Pt/Ti/Si$, $Ta_3N_5/Pt/Ti/SiO_2/Si$ and $Ta_3N_5/Pt/Ti$. Ti and Pt were deposited by DC Magnetron sputtering whereas SiO_2 was thermally grown on Si wafer under controlled oxygen flux. The thickness of Pt, Ti and SiO_2 layers was, 200, 7.2 and 150 nm, respectively. Ti layer helped for the adhesion and Pt served as electric contact.[24] Prior to each measurement the samples were etched to possibly clean the surface by HF/H_2O droplets on Ta_3N_5 part of the film and after 10 sec the samples were cleaned by distilled water and dried under nitrogen flux. The wires and the exposed conductive parts of the samples were sealed with an epoxy adhesive. We found that the using variety of substrates do not influence the PEC results; therefore, in this work we have applied $Ta_3N_5/Pt/Ti/quartz$ for the measurements.

The photoelectrochemical measurements were performed in a three electrode configuration employing $Ta_3N_5/Pt/Ti/quartz$ as working electrode, Pt wire as counter electrode and Ag/AgCl as a reference electrode. 0.1 M sodium phosphate buffer solutions adjusted to pH 4, 8 and 12 were used. The potentials of the working electrode were controlled by using Auto-lab. AM 1.5 filter was used to simulate the solar spectrum. The light intensity was calibrated using a silicon photodiode with known responsivity of 100 mW.cm^{-2} (1 Sun). Linear sweep voltammetry (LSV) curves were obtained at a scan rate of 10 mV/s. The Mott-Shottky plots were obtained at a frequency of 1k Hz with 10 mV of the signal amplitude for a range of applied potentials.

2.4.2. Nanotubes

Prior to the experiments the Ta_3N_5 NTs photoanodes were cleaned by immersing into $HF:H_2O$ (1:9) for 30 seconds, rinsing with distilled water and drying under nitrogen flux to remove surface contamination. The photoelectrochemical measurements were performed in a three electrode configuration with Ta_3N_5 as working electrode, Pt wobbling as counter electrode and Ag/AgCl (3.5 M) as a reference electrode. For preparing Ta_3N_5 NTs working electrode the sample was capsulated, except from the front, by a homemade Teflon reactor. An O ring was used to seal the front side of reactor to prevent any leakage. A copper disc was placed behind the Ta_3N_5 photoanode where a thin copper wire was utilized as path for the

current flow. The backside of the reactor was screwed tightly with the Teflon screw to prevent electrolyte entrance from the backside of the reactor to the Ta_3N_5 NTs/Ta photoanode. The electrodes were immersed in a homemade Pyrex cell having a quartz window. As a source of electromagnetic radiation Xe lamp (300W) was utilized. AM 1.5G filter was used to obtain solar spectrum. The electrolytes used for Photoelectrochemical measurements were 0.1 M Na_2SO_4 pH (7.85), [11] and redox couple of 0.1 M $K_4[Fe(CN)_6]$ and 0.1 mM $K_3[Fe(CN)_6]$ pH (7.5).[82] The solution pHs were recorded by digital pH meter. Prior to each photoelectrochemical measurement the electrolytes were purged by the argon gas flow. The Auto-lab (PGSTAT100/*AUT 84503*) potentiostat incorporated with software (GPES, V 4.9) was used as a power supply. Linear sweep voltammetry (LSV) curves in dark and under illumination (1 Sun) were obtained under scan rate of 10 mV/s. Similarly, hand light chopping with a 5 sec periodic interval was performed to record LSV curves. Cyclic voltammetry was performed under dark and illumination for the varying scan rates (10 mV/s to 200 mV/s).
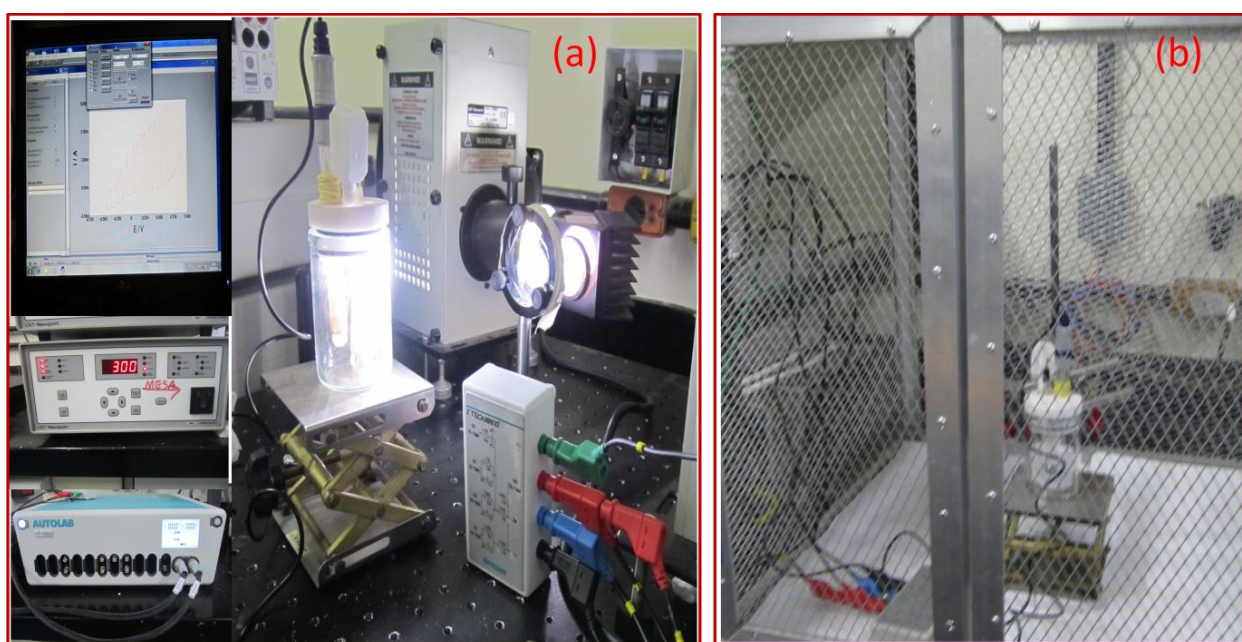
Fig.2. 4 (Photo)electrochemical setup comprising of potentiostat, Xe lamp and Faraday cage.

The light intensity was calibrated by using a silicon photodiode with known responsivity. Chronoamperometry experiments were performed under different values of constant applied potentials, under light and under dark which helped us to approximate the flatband of Ta_3N_5 NTs photoanode. Furthermore, impedance measurements were performed in a Faraday cage, by using the software FRA (frequency response analysis). Nyquist plots were obtained in a frequency range of 100 kHz–100 mHz at fixed amplitude of 5 mV by using different fixed

potentials. Circuit fitting was complied by NOVA software. Mott-Shottky plots were obtained at 5 mV of amplitude for a range of frequencies and applied potentials. **Fig.2.4a**. shows the setup for LSV, CV, chronoamperometry experiments while **Fig. 2.4b** displays the setup used for EIS.

Note: Solar radiation reaching the earth's surface varies significantly with location, atmospheric conditions including cloud cover, aerosol content and ozone layer, and time of the day, earth/sun distance, solar and ozone layer conditions etc. The irradiance of the sun on the outer atmosphere when the sun and earth are spaced at 1 astronomical unit (AU) is called solar constant, i.e mean earth/sun distance of 149,597,890 km and the radiation intensity at 1 AU is 1360 W m^{-2}. Air Mass (AM) represents how much atmosphere the solar radiation has to pass through before reaching the Earth s' surface. The AM number can be determined from the zenith angle of the Sun by the following expression:

$$AM = 1/\cos \Theta_{zenith}$$

AM 0 is defined as the spectrum outside the Earth's atmosphere at 1 AU from the Sun, and AM 1 represents sunlight reaching the Earth's surface (at sea level) when the Sun is directly overhead. AM 1.5 is defined as the irradiance arriving on a flat plate tilted at 37° from horizontal toward the Sun. Because Θ_{zenith} = 48.2° for AM 1.5 and the tilt angle is 37°, the angle of incidence is 11.2°. An intensity is specified, as well as the spectral distribution of illumination, the accepted total irradiance (intensity) of AM 1.5 is being 1000 W/m^2 (100 mW/cm^2). For PEC experiments AM 1.5 is simulated in the lab by using appropriate filter in front of the radiation source, because it is standardized and represents approximately the average annual AM value available at locations within the continental US. [83] Depending on the application utilizing AM 1.5 filter, the intensity of light can be calibrated to ½ Sun (50 mW/cm^2), 1 Sun (100 mW/cm^2), 2 Sun (200 mW/cm^2), 3 Sun (300 mW/cm^2) etc. However, for PEC applications mostly 1 Sun (100 mW/cm^2) is used.

2.5. Characterizations

2.5.1. Scanning Electron Microscopy

Surface structure and morphology of Ta_3N_5 thin films, as-anodized Ta_2O_5 NTs and Ta_3N_5 NTs were characterized by using a Scanning Electron Microscope (Zeiss, EVO 50) operated at 10 kV. The side view images of the NTs were obtained from the scratched off area of the sample. Where necessary, the samples were metalized by sputtering.

2.5.2. High resolution transmission electron microscopy

For Ta_3N_5 thin films; the samples were prepared in plan view and analyzed by JOEL JEM 2010 microscope.

For Ta_3N_5 NTs; the samples were prepared by scratching off the NTs to dissolve in acetone and later loaded onto carbon grid. For the TEM imaging JEM 1200 EXll was used. Scanning transmission electron microscopy (STEM), HRTEM, SAED, spatial-energy Dispersive X-ray (EDX) were performed using an XFEG Cs-corrected FEI Titan 80/300 microscope at INMETRO operated at 300 kV. High Z-contrast images were acquired through STEM using a high-angle annular dark-field detector (HAADF). The typical lateral resolution was greater than 0.01 nm. To simulate HRTEM spectra the software "CrystalKit" was used. For EDX spectra the intensity was normalized to the Ta signal.

2.5.3. UV –Vis spectrophotometry

UV-Vis spectrophotometry was performed by using CARY 5000. The absorption spectra of Ta_3N_5 NTs were obtained by diffuse reflectance by converting to the Kubelka-Munk function:

$$K.M\ (R) = \frac{(1-R)^2}{2R} \tag{2.1}$$

For Ta_3N_5 thin films deposited over quartz substrate, total reflectance and transmittance were obtained. The light absorption from the Ta_3N_5 film was calculated using the expression:

$$\%\,Abs = 100 - (\%\,T + \%\,R) \tag{2.2}$$

2.5.4. XRD (X-ray diffraction spectroscopy)

Conventional diffratograms of Ta_3N_5 NTs were obtained by using *Rigaku, Ultima IV diffractometer* with Cu K_α radiation ($\lambda = 1.54$ Å) at a 2θ range from $10°$ to $90°$ with a $0.05°$ step size and measuring time of 1s per step. Grazing angle XRD was recorded by *Shimadzu, Maxima XRD-7000 diffractometer* with an incident angle of $0.3°$ with Cu K_α radiation ($\lambda = 1.54$ Å) at a 2θ range from $10°$ to $70°$ with a $0.05°$ step size and measuring time of 5s per step. The powder XRD for free standing Ta_3N_5 powder and Ta_3N_5 sputtering film was obtained by using *a Siemens, D500 diffractometer* with Cu K_α radiation ($\lambda = 1.54$ Å) at a 2θ range from

10° to 70° with a 0.05° step size and measuring time of 5 s per step. All of the XRD patterns were recorded under "*Bragg-Brentano geometry*".

Data processing was performed by the Rietveld method using FullProf software.[84] The instrumental resolution function (IRF) of the diffractometer was obtained from the LaB6 standard. The pseudo-Voigt profile function of Thompson, Cox and Hastings was used with an asymmetry correction at low angles.[85] Corrections to the preferred orientation were performed using the Modified March's function.[86] [87] [88] The anisotropic size broadening effects, related to the coherence volume of diffraction, were simulated using a model of spherical harmonics.[84] To understand the crystalline structure of Ta_3N_5, Rietveld refinement were performed. The grain size has been calculated by modified Scherrer equation (2.3) considering the microstrain as minimum as possible.

$$\beta_h = \frac{\lambda}{D_h \cos\theta} = \frac{\lambda}{\cos\theta} \sum_{lmp} a_{lmp} y_{lmp}(\Theta_h, \Phi_h), \qquad (2.3)$$

where β_h is the size contribution to the integral breadth of reflection h, $y_{lmp}(\Theta_h, \Phi_h)$ are the real spherical harmonics with normalization.[89] The arguments are the polar angles of the vector h with respect to the Cartesian crystallographic frame. After refinement of the coefficients the program calculates the apparent size (in angstroms) along each reciprocal lattice vectors if the IRF is provided in a separate file. The preferential orientation has been identified by using the modified March´s function (equation, 2.4):

$$P_h = G_2 + (1 - G_2)\left((G_1 cos\alpha_h)^2 + \frac{sin^2\alpha_h}{G_1} \right)^{-3/2} \qquad (2.4)$$

where G_1 corresponds to the Bragg−Brentano geometry, G_2 represents the fraction of the sample without orientation, and α_h is the acute angle between the scattering vector and the normal to the crystallites. From the analysis of the Rietveld refinement, the grain size along different directions and the nominal stoichiometry were calculated.

2.5.5. X-ray photoelectron spectroscopy (XPS)

Chemical composition of the surface was studied by X-ray photoelectron spectroscopy (XPS) performed in an Omicron-SPHERA station using Al Kα radiation (1486.6 eV). The anode was operated at 225 W (15 kV, 15 mA). Survey spectra were recorded with 50 eV pass

energy. The Ta 4f, O1s and N1s regions were recorded with a higher resolution (pass energy of 10 eV). The detection angle of the photoelectrons (Θ) with respect to the sample surface (take-off angle) was fixed at 53° for all measurements. The C 1s signal from adventitious carbon was used as an internal energy reference. During the synthesis and transferring the samples into the spectrometer, the surface of the sample was exposed to air prior to the measurement (as were all of the samples) and, therefore, contained surface oxide. For the deconvolution of Ta4f, the spin-orbit doublet separation of 1.9 eV and the intensity ratio ($Ta4f_{7/2}/Ta4f_{5/2}$) of 4/3 were used in all peak assignments). The surface composition N/Ta was calculated by using relative sensitivity factor (RSF) method as follows:

N/Ta = (Area of N1s / RSF) ÷ (Area of Ta4f / RSF)

Similar procedure was followed for O/Ta and N/O composition ratios. Although, the Ta 4f signal is known to overlap with the minor O 2s signal and the ratio of the total cross section for the Ta 4f / O 2s is around 66. Therefore, the contribution from O 2s was neglected in this study.

For Ta_3N_5 thin films similar procedure was followed.

2.6. Spectroscopic Ellipsometry

Ellipsometry is one of the most powerful tools to investigate optical properties of materials, [90] the technique usually performs analysis of the reflected light polarization state, which is related to the optical properties of the material by the expression (the Ellipsometry fundamental equation):

$$\rho = \frac{r_p}{r_s} = \tan(\psi) * \exp(i\Delta), \tag{2.5}$$

where $\tan(\psi)$ and Δ are the amplitude ratio and phase shift difference, respectively, between values associated with the p and s polarization components of light (parallel and perpendicular to the plane of incidence). The r_p and r_s are the correspondent Fresnel coefficients when a unique interface reflects the light under study [91] and they depend on: the angle of incidence (ϕ) and wavelength (λ) of the light and the dispersion curves of air $N_0(\lambda)$ and bulk material $N(\lambda)$. In the case of thin films, r_p and r_s are the correspondent Drude reflection coefficients

and are dependent of: the angle of incidence (ϕ) and wavelength (λ) of the light, film thickness (d) and dispersion curves of air $N_0(\lambda)$, substrate $N_s(\lambda)$ and film $N_f(\lambda)$. [91] The dispersion curves present the form $N(\lambda) = n(\lambda) + ik(\lambda)$, where $n(\lambda)$ and $k(\lambda)$ are the real and imaginary parts of the refractive index, respectively. **Fig.2.5** displays the experimental setup normally used for the Ellipsometry in which the s and p polarised lights are incident on the sample; thereby they reflect and becomes elliptically polarized.
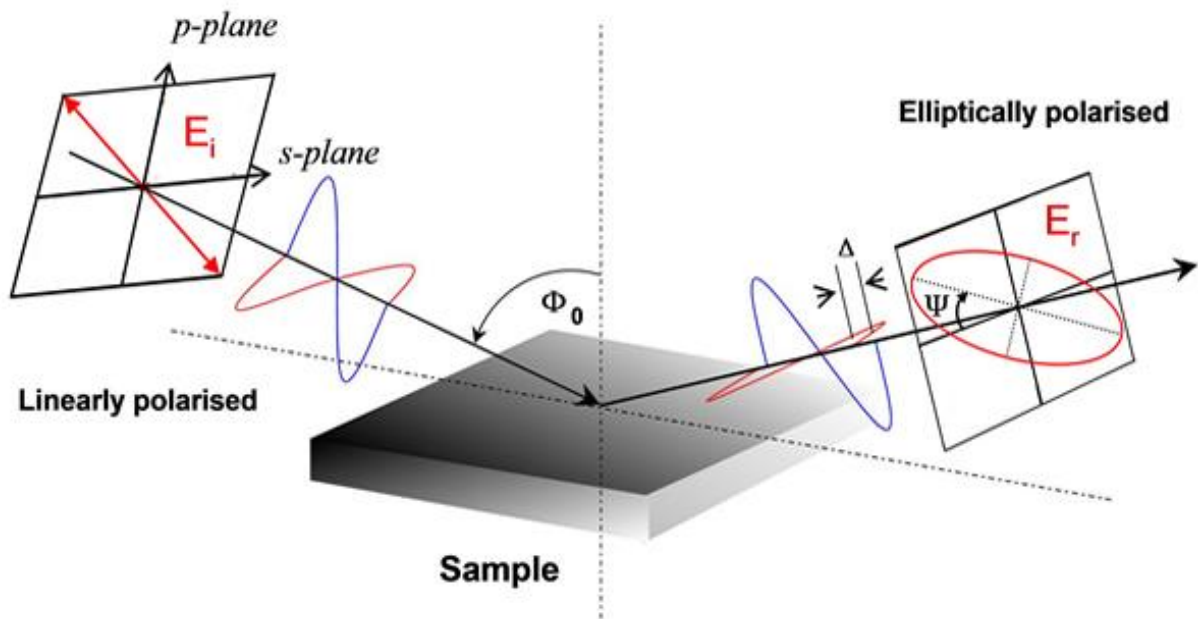
Fig.2. 5 Experimental setup for Ellipsometry.

Upon reflection from the sample, the phase difference between the two incident lights and the *tanΨ* that are the characteristic of the sample under study are determinate. Experimental data are modeled according to the suitable parameterization that reflects the physical characteristic of the sample under study.

2.6.1 Rotating Polarizer Technique

There are many different experimental configurations of Ellipsometers as, for example, the ellipsometers of light extinction.[90] However, the Ellipsometer used in this work has a different approach to characterize the optical constants of a material; it uses the rotating polarizer technique, where only two optical components are used: one polarizer (rotating with a fixed frequency of 5Hz) and an adjustable polarizer (analyzer) that is employed to maximize the intensity of the light reflected from the sample. The amplitude of the electric field of light

is split into the s and p components and it is possible to represent the effects of each element of the ellipsometer over these fields by the Muller Matrix notation [92]:

$$\text{Lamp: } L = \begin{pmatrix} E_0 \\ E_0 \end{pmatrix} \tag{2.6}$$

$$\text{Polarizer: } Pol = \begin{pmatrix} 1 & 0 \\ 0 & 0 \end{pmatrix} \tag{2.7}$$

$$\text{Theta angle rotation (polarizer): } R(\theta_{Pol}) = \begin{pmatrix} cos\theta_{Pol} & -sin\theta_{Pol} \\ sin\theta_{Pol} & cos\theta_{Pol} \end{pmatrix} \tag{2.8}$$

$$\text{Sample: } E = \begin{pmatrix} r_p & 0 \\ 0 & r_s \end{pmatrix} \tag{2.9}$$

$$\text{Analyzer: } Ana = \begin{pmatrix} 1 & 0 \\ 0 & 0 \end{pmatrix} \tag{2.10}$$

On the detector, the electric field amplitude assumes the value:

$$E_d = Ana * R(\theta_{Ana}) * E * R(-\theta_{Pol}) * Pol * L \tag{2.11}$$

Finally, the intensity registered on the detector can be expressed by:

$$I = I_0(\alpha * cos2\theta_{Pol} + \beta * sin2\theta_{Pol} + 1) \tag{2.12}$$

with

$$\alpha = \frac{tan^2\psi - tan^2\theta_{Ana}}{tan^2\psi + tan^2\theta_{Ana}} \tag{2.13}$$

$$\beta = 2 * cos\Delta * \frac{tan\,\psi * tan\,\theta_{Ana}}{tan^2\psi + tan^2\theta_{Ana}} \tag{2.14}$$

$$I_0 = \frac{|r_s|^2 * |E_0|^2}{2} * \frac{cos^2\theta_{Ana}}{tan^2\psi + tan^2\theta_{Ana}} \tag{2.15}$$

θ_{Pol} and θ_{Ana} are, respectively, the angle between the transmission axis of the polarizer, and analysis polarizer, and the light incidence plane. The coefficients α and β do not depend on the lamp intensity, so there is no necessity of a reference measurement for the intensity and the ellipsometric parameters can be expressed as:

$$tan\,\psi = \sqrt{\frac{1+\alpha}{1-\alpha}} * tan\theta_{Ana} \qquad (2.16)$$

$$cos\,\Delta = \frac{\beta}{\sqrt{1-\alpha^2}} \qquad (2.17)$$

To analyze the signal and extract the two components (α and β), the Hadamard method [93] is used and the signal is integrated every quarter of polarizer period and each sum can be calculated as follow (it is considered a complete turn of the polarizer, two regions of the sums S1 to S4), as showed in **Fig. 6.2**:

$$S_1 = \int_0^{\pi/4} I(\theta_{Pol})\,d\theta_{Pol} = \frac{I_0}{2} * (\alpha + \beta + \pi/2) \qquad (2.18)$$

$$S_2 = \int_{\pi/4}^{\pi/2} I(\theta_{Pol})\,d\theta_{Pol} = \frac{I_0}{2} * (-\alpha + \beta + \pi/2) \qquad (2.19)$$

$$S_3 = \int_{\pi/2}^{3\pi/4} I(\theta_{Pol})\,d\theta_{Pol} = \frac{I_0}{2} * (-\alpha - \beta - \pi/2) \qquad (2.20)$$

$$S_4 = \int_{3\pi/4}^{\pi} I(\theta_{Pol})\,d\theta_{Pol} = \frac{I_0}{2} * (\alpha - \beta + \pi/2) \qquad (2.21)$$
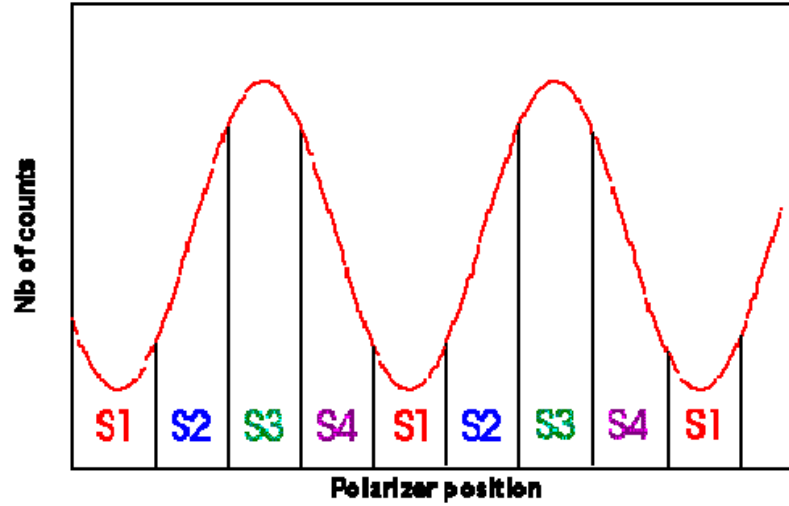
Fig.2. 6 Intensity of light reflected by the sample as a function of the polarizer angle (θ_{Pol}) and the 4 polarizer regions.

Then the parameters of the signal can be expressed versus the sums as follow:

$$\alpha = \frac{1}{2I_0}(S_1 - S_2 - S_3 + S_4) \tag{2.22}$$

$$\beta = \frac{1}{2I_0}(S_1 + S_2 - S_3 - S_4) \tag{2.23}$$

$$I_0 = \frac{1}{\pi}(S_1 + S_2 + S_3 + S_4) \tag{2.24}$$

The equipment used was an ellipsometer SOPRA GES-5E with a special microspot accessory for thin films: two sets of lenses (numerical apertures of 3^0), one is used to focus the light beam in a small region of the film surface (an ellipse area of approximately 365 μm × 270 μm) and the second one is used to collect the reflected light that will be analyzed. The ellipsometer employs one rotating polarizer (frequency of 5Hz) and one analysis polarizer to maximize the reflected light by the sample to obtain the ellipsometric parameters ψ and Δ,. More details can be seen in references. [90, 93]. The ellipsometry measurements were performed in the wavelength range from 215 to 800 nm and at an angle of incidence $\phi_0 = 68^0$. The collected data in the measurements (the state of polarization) was analyzed by the equipment's software WinElli 2.2.0.6 using a model that will be described in details in chapter 3.

CHAPTER 3

OPTICAL AND PHOTOELECTROCHEMICAL PROPERTIES OF MONOCLINIC Ta$_3$N$_5$ THIN FILMS

3.1 Objectives

Recently, RF magnetron sputtering has attracted much attention as a clean route to synthesize materials.[50] The direct sputtering of Ta$_2$O$_5$ for its transformation to Ta$_3$N$_5$ has not been reported in the literature. The literature reports that Ta$_3$N$_5$ presents two different crystalline phases, monoclinic (JPCDS file 89-5200) and orthorhombic (JPCDS file 79-1533). The phases are very close to each other as their unit cell parameters (a, b and c) present almost the same magnitudes; therefore, their diffraction patterns look very similar and a special attention is necessary to assign the crystalline phases of Ta$_3$N$_5$. The easiest approach to assign any of these phases from the XRD patterns is to observe the relative intensity between the 2θ peaks of 24.52° and 36.16°which are different for both of the phases.[66] The crystalline phases of Ta$_3$N$_5$, largely depend on the route of synthesis, choice of precursor and the underlying substrate. The orthorhombic phase of Ta$_3$N$_5$ has been widely reported, but there are few reports regarding the monoclinic phase. [94 65 95] The dielectric constant of a material plays an important role in many physical processes. Technical applications such as capacitors, insulating coatings transducers are strongly determined by the dielectric properties. In addition, to calculate the density of states by Mott-Schottky curves, there is a need of reliable data on dielectric constants of a material.[9 96] After searching the literature, we have not found any work describing the experimental determination of the dielectric constant of Ta$_3$N$_5$.

Herein, thin films of Ta$_2$O$_5$ have been deposited on quartz substrate by RF magnetron sputtering and thermally nitrided to obtain Ta$_3$N$_5$ thin films, which exhibited monoclinic crystalline phase. Using Spectroscopic Ellipsometry technique, the light absorption coefficient and the dielectric constants of Ta$_3$N$_5$ films were experimentally determinate. Using Mott-Schottky analyses flat band and effective density of states were calculated for monoclinic Ta$_3$N$_5$ thin films.

3.2 Results and Discussion

3.2.1 Surface and structure of Ta_3N_5 thin films

The SEM images of the samples before and after the nitridation are shown in **Fig.3.1** It can be seen that as-deposited Ta_2O_5 film presents a smooth, homogenous and flat surface. However, after annealing, the film was cracked and some patches appeared on the entire surface (**Fig. 3.1b**). The diameters of these patches were calculated by estimating the average of longest and shortest distance inside each patch, which was ~10.4 μm and the average spacing between them was approximately ~24 nm. The cracks observed in the films at higher temperature are attributed to the interfacial stress caused by the difference in thermal expansion of the film and substrate.[97] Besides, the surface of Ta_3N_5 is rough (**Fig. 3.1 c**), which is related to the density difference between Ta_2O_5 and Ta_3N_5.[98] The HRTEM (**Fig. 3.1 d**) image shows the interplanar distance of 0.512 nm in agreement with the monoclinic crystalline structure of Ta_3N_5. The grain size from the HRTEM image was estimated to be 46 nm. In addition, some amorphous layer can be observed on the edges of the grain.
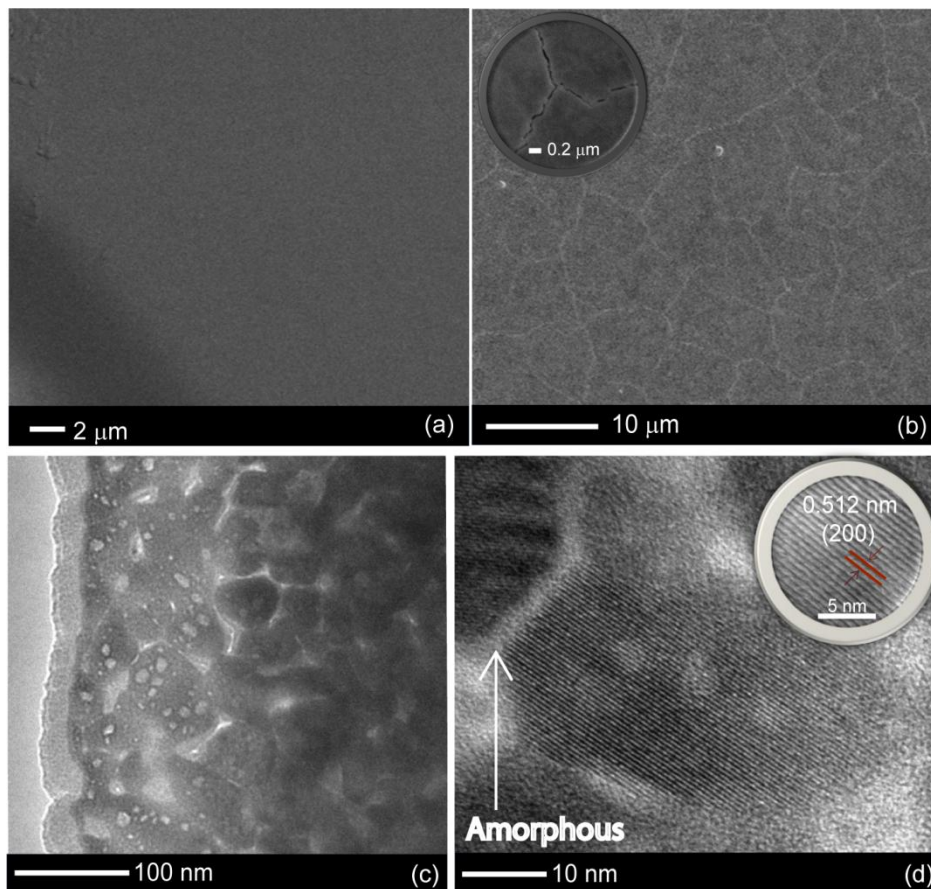
Fig.3. 1 SEM images of (a) as-deposited Ta_2O_5 and (b) Ta_3N_5 thin films. TEM (c) and HRTEM images (d) of Ta_3N_5 thin films.

The XPS spectra of the as-nitrided thin films are presented in **Fig. 3.2** One can observe the presence of oxygen on the surface of the films, which is a natural impurity in Ta_3N_5.[68] The O1s and N1s peaks were observed at 529.8 eV and 395.5 eV, respectively (**Fig. 3.2a**). The deconvoluted Ta 4f doublet and N1s region of the film are shown in **Fig. 3.2b & c,** respectively. The $Ta4f_{7/2}$ and $Ta4f_{5/2}$ appeared at 25.3 eV and 27.2eV which are closed to the previously reported values for oxynitride species of tantalum[99] In addition, high-energy-side small doublet was also detected; suggesting the presence of low energy states (Ta^{4+}, Ta^{3+}) of Ta.[100,101] The formation of reduced tantalum species in Ta_3N_5 obtained by thermal nitridation, has been reported earlier. [102] Subtracting the area of the small Ta4f doublet and considering the sensitivity factors for N1s and Ta4f, the nominal surface composition from the XPS analysis was found to be $Ta_{2.66}N_{4.32}O_{0.17}$ which indicates the surface of film does not possess complete stoichiometry of Ta_3N_5.[103]
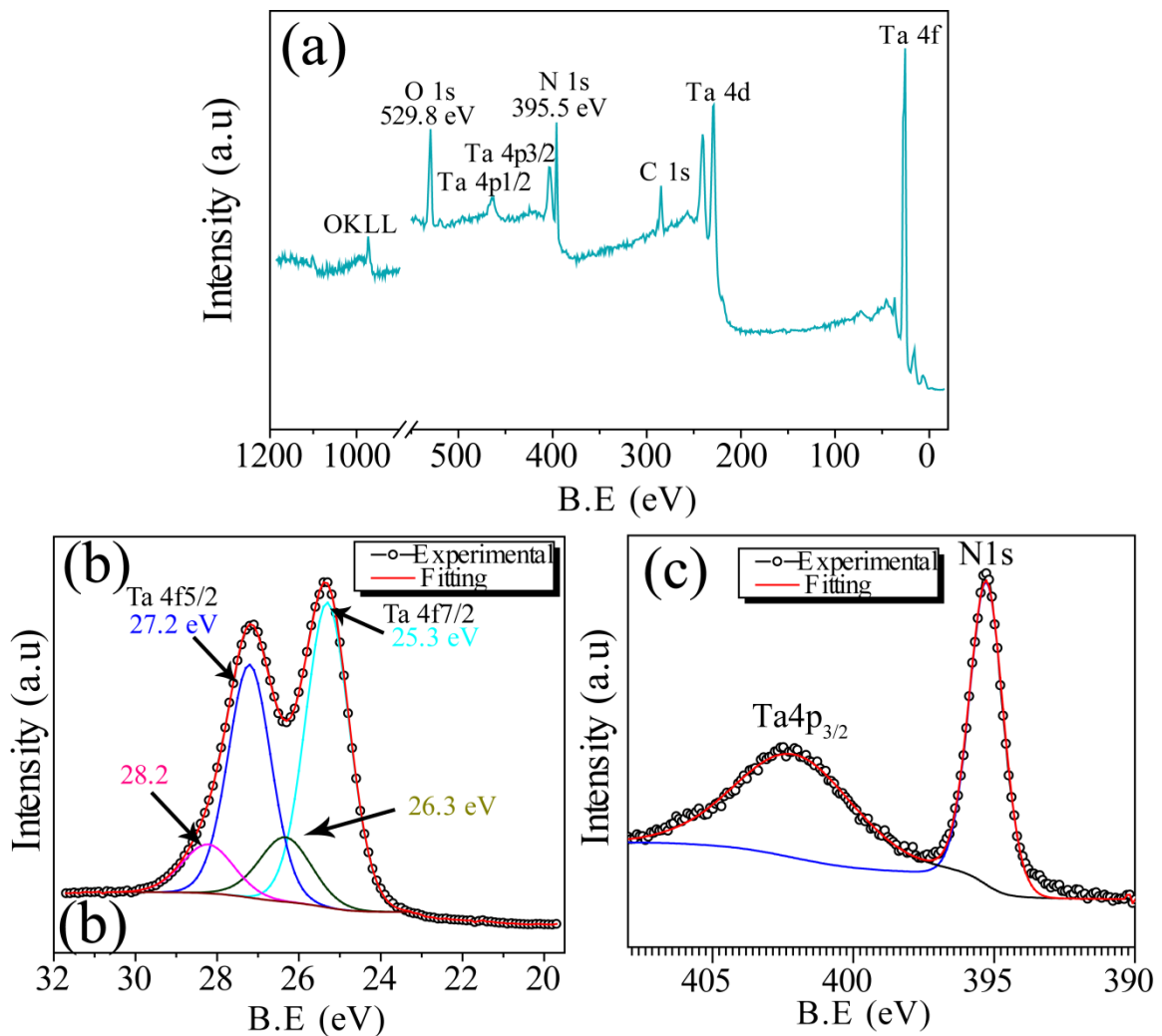
Fig.3. 2 XPS (a) survey and (b) deconvoluted Ta4f and (c) N1s spectra of the as-nitrided films.

From the results shown above, we infer that the defective nature of the surface and the amorphism around the grain should be considered carefully if Ta_3N_5 is used as a photocatalyst as they can act as recombination centers for photogenerated carriers. We suggest a proper surface cleaning before applying Ta_3N_5 thin films in photoelectrochemical applications.

The XRD patterns of as-sputtered Ta_2O_5 and Ta_3N_5 films are shown in **Fig. 3.3**. It can be seen that Ta_2O_5 thin films are amorphous. However, after thermal nitridation at 900°C for 24 hours under 100 mL/min of NH_3 flow, clear changes in the XRD patterns can be observed.
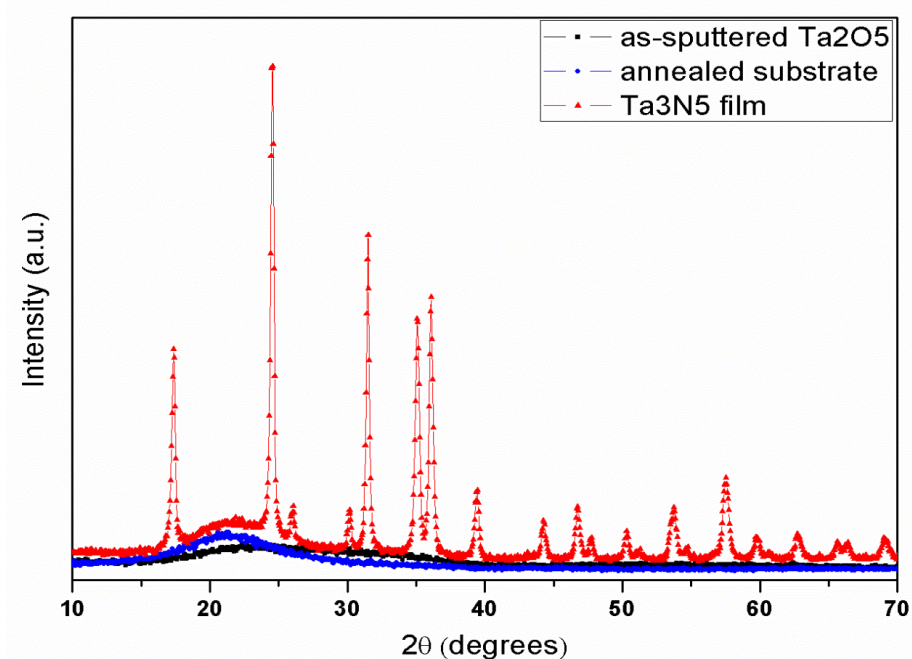
Fig.3. 3 XRD patterns of as-sputtered Ta_2O_5 thin films, substrate nitrided at 900°C and the Ta_3N_5 thin films.

The amorphous Ta_2O_5 is transformed into Ta_3N_5 presenting very sharp diffraction peaks. This result indicates that the nitridation condition used was sufficient to transform Ta_2O_5 thin film into Ta_3N_5. All peaks observed in the XRD diffractograms are in a good agreement with the monoclinic phase of Ta_3N_5 (JPCDS file 89-5200). The average grain size calculated through the Scherrer´s equation from the most intense peak was approximated to 43 nm. Furthermore, in the XRD patterns of Ta_3N_5 film a wide background at ca. 22° was observed that is related to the substrate nitridation as shown in the figure (blue color line).

3.2.2 Optical constants of Ta₃N₅ thin film

The absorbance of the Ta$_3$N$_5$ thin film was determined by the equation 2.2 using experimental data from total transmittance and reflectance measurements. The calculated film absorbance is shown in **Fig. 3.4a**. One can observe a strong absorption band between 200 and 557 nm and a dramatic drop from 558 to 800 nm, displaying an oscillatory pattern, which may be related to the light interference in thin films. In order to obtain the optical constants of the Ta$_3$N$_5$ thin film all these optical behaviors were taken into account to build the model in the ellipsometer analysis software,. Within the region presenting strong absorption (215 to 557 nm), a bulk like behavior is assumed, so the refractive indices are directly related to ellipsometric parameters by the expression:

$$n(\lambda) + i\kappa(\lambda) = sin\,\phi_0 \sqrt{1 + tan^2\phi_0 \frac{(1-\rho)^2}{(1+\rho)^2}}, \tag{3.1}$$

where n(λ) and κ(λ) are the real and imaginary parts of the refractive index, respectively, and ϕ_0 is the angle of incidence. The calculated dispersion curves for n(λ) and κ(λ) using the bulk model are represented in **Fig. 3.4b**.
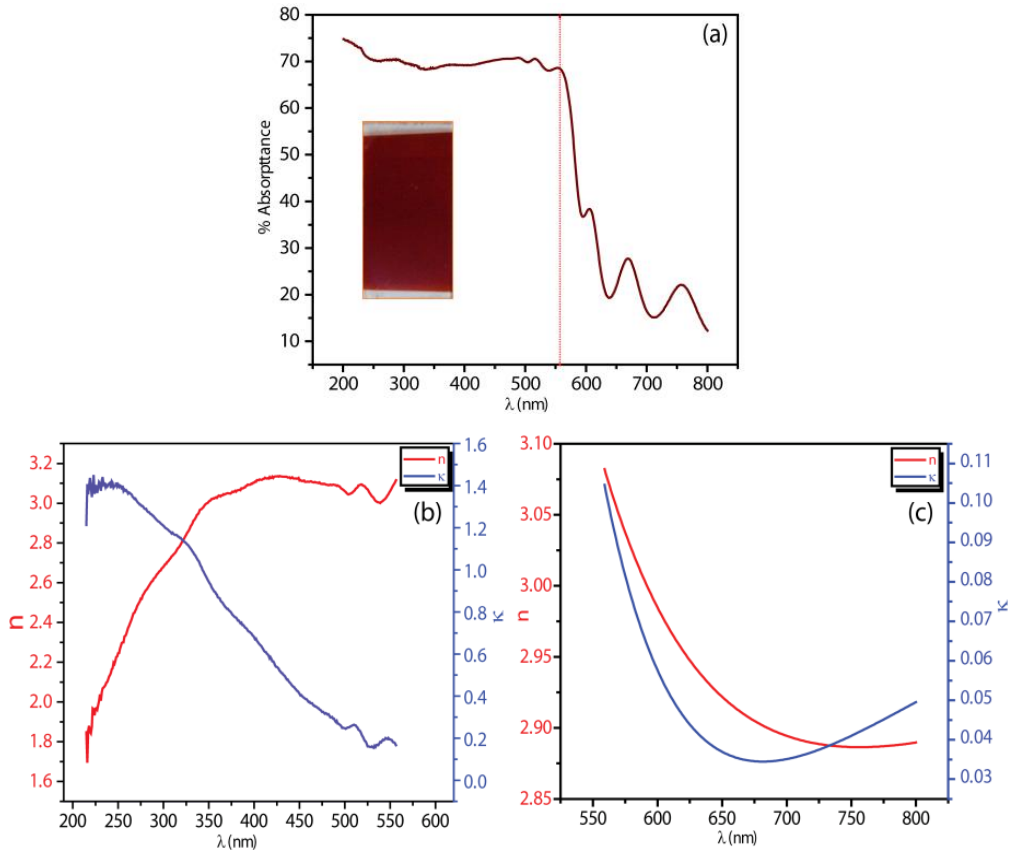
Fig.3. 4 Absorbance spectrum of Ta$_3$N$_5$ thin film (a). Real and Imaginary dispersion curves obtained for the Ta$_3$N$_5$ film assuming bulk model (b) and Cauchy model (c).

In the wavelength range of 558 to 800 nm, it was assumed that the sample is an isotropic and homogeneous film with dispersion curves (**Fig. 3.4c**) following the well-known Cauchy model, as follow: [104]

$$n(\lambda) = A + \frac{B}{\lambda^2} + \frac{C}{\lambda^4} \tag{3.2}$$

$$\kappa(\lambda) = \frac{D}{\lambda} + \frac{E}{\lambda^3} + \frac{F}{\lambda^5}, \tag{3.3}$$

where A, B, C, D, E and F are constants which are adjusted by the analysis software to perform the fitting to the experimental data. The optical constants from the film (dispersion curves and physical thickness) were obtained through the equation 2.5 with the terms given by equation 2.16 and 2.17 following the above proposed model. These constants were obtained by curve adjusting with the fitting of $R^2 = 0.928158$, where $R^2 = 1$ represents a perfect fitting and their values can be seen below:

A = 3.170 ± 0.005   B = -0.324 ± 0.002   C = 0.0929 ± 0.0003

D = 0.2071 ± 0.0003   E = -0.165 ± 0.001   F = 0.0371 ± 0.0004

As a result, the calculated film thickness was 890.1 ± 0.2 nm. Furthermore, from the dispersion curves of **Fig. 3.4** (**b** & **c**), the dielectric constants (real and imaginary) from the film were calculated using the following relations:[91]

$$\varepsilon_r(\lambda) = n^2(\lambda) - \kappa^2(\lambda) \tag{3.4}$$

$$\varepsilon_i(\lambda) = 2 * n(\lambda) * \kappa(\lambda) \tag{3.5}$$

Plugging the values of n(λ) and κ(λ) obtained from both models in equations 3.4 and 3.5 the dielectric constants were calculated and presented in **Fig. 3.5**.
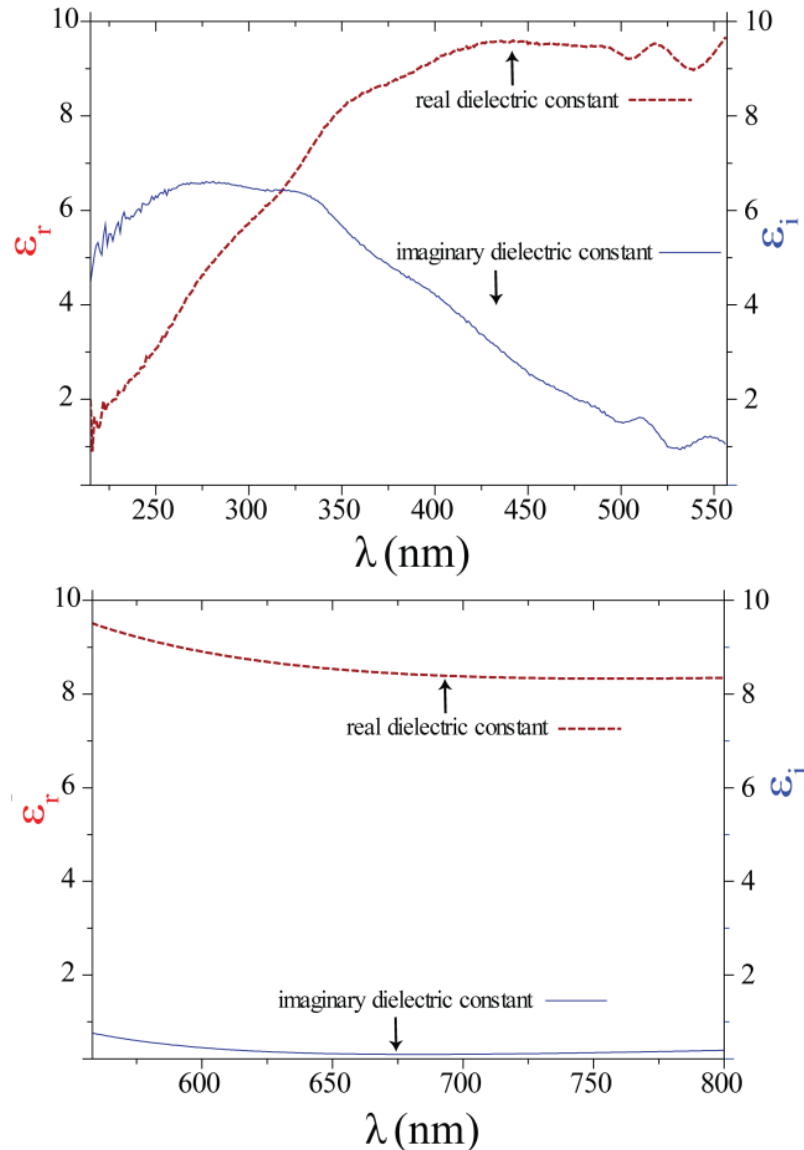
Fig.3. 5 Dielectric constants (real and imaginary) of Ta$_3$N$_5$ film, assuming bulk model (left) and Cauchy model (right).

A slight divergence within the region where the models merge together (at 558 nm) can be observed and is attributed to the combined effects of bulk and film behavior. As observed for other substances, the dielectric constants change with the wavelength. This frequency dependence ignites from the different polarizability which arises from different mechanisms driven by the change in the frequency.[96] From **Fig.3.5**, the dielectric constant presents values between 7 and 9. Interestingly, these values match the theoretically measured dielectric constant of Ta$_3$N$_5$ where the presence of oxygen impurities were taken into account.[68]

According to the Beer-Lambert law, the absorption coefficient "α" of a material is related to the imaginary part of the refractive index $\kappa(\lambda)$ by the following expression:

$$\alpha \;=\; \frac{4\pi\kappa}{\lambda} \tag{3.6}$$

From the values of κ (λ) obtained from the two models as shown in **Fig. 3.4 (b, c)**, the α values were calculated by equation 3.6 and shown in **Fig. 3. 6a**. According to the literature, for the theoretical dispersion energy bands obtained for Ta_3N_5, the top of the valence band was found to be along the Γ–X line and the bottom of the conduction band was located at Y in the BZ, which indicates that Ta_3N_5 is an indirect semiconductor.[67] By using the values of α, the indirect bandgap considering the Tauc´s plots have been estimated as ~1.92 eV, which is smaller than the theoretically predicted value. The corresponding spectrum is shown in **Fig. 3.6b**. The difference between theoretical and experimental bandgap is related to the presence of oxygen in the structure of Ta_3N_5. [68]
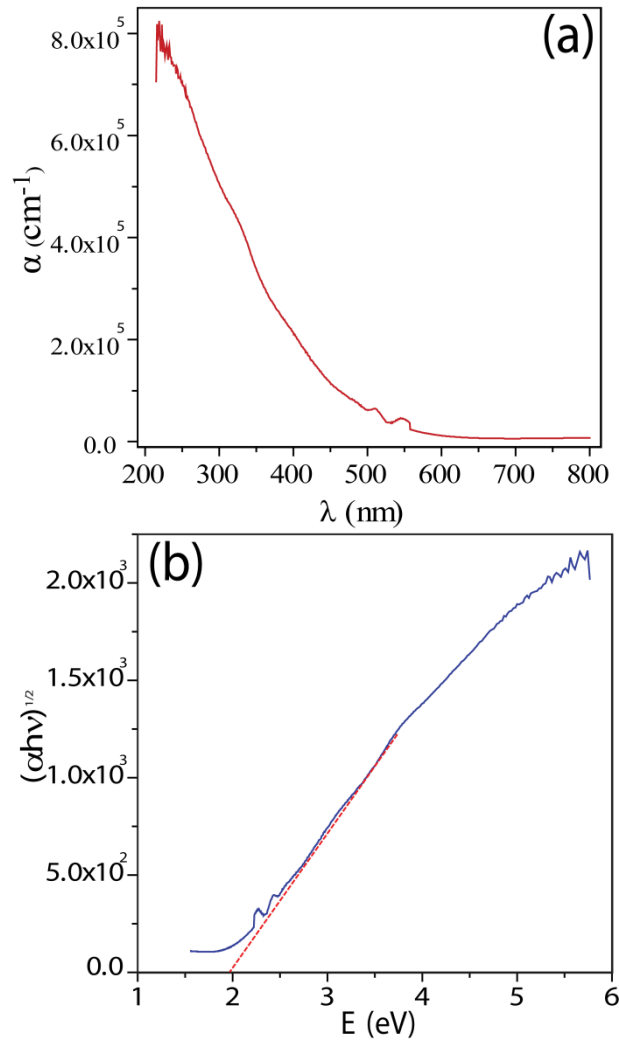
Fig.3. 6 Variations of α with wavelength (a) and $(\alpha h\nu)^{1/2}$ with energy (b).

3.2.3 Photoelectrochemical properties of Ta_3N_5 thin film

The bandgap energy of Ta_3N_5 overcomes the endothermic 1.23 eV requirement for the water splitting.[68] However, the positions of band edges relative to the water redox potentials influence the water splitting activity. The flat band position that helps to find the conduction band position can be calculated by the Mott-Schottky equation. The Mott-Schottky equation is [105]

$$\frac{1}{C^2} = \frac{2}{\varepsilon\varepsilon_0 A^2 e N_D} \left(V - V_f - \frac{K_b T}{e} \right) \qquad (3.7)$$

Where C, e, ε, ε_0, V, K_b and V_f are the space charge capacitance, the electronic charge, the dielectric constant i.e 8 (**Fig. 3.5**), vacuum permittivity, applied potential, Boltzmann constant and the flat band potential, respectively. The intersection of the linear dependence of $1/C^2$ versus V provides the flat band and the slope of the curve contains the information on the effective donor density (N_D). **Fig 3.7** compares the Mott-Schottky plots of the Ta_3N_5 thin films measured in phosphate buffer electrolytes adjusted to pH 4, 8 and 12. It can be seen that V_f is strongly influenced by the pH of the solution, as pH is increased, the V_f is shifted toward more negative potentials. In addition, the positive slope of observed in the Mott-Schottky curves clearly indicate that monoclinic Ta_3N_5 is an n-type semiconductor. Using equation 3.7 the values of N_D were also calculated and were found to be 1.2×10^{18}, 5.1×10^{19} and 1.3×10^{20} cm^{-3} for pH 4, 8 and 12, respectively.
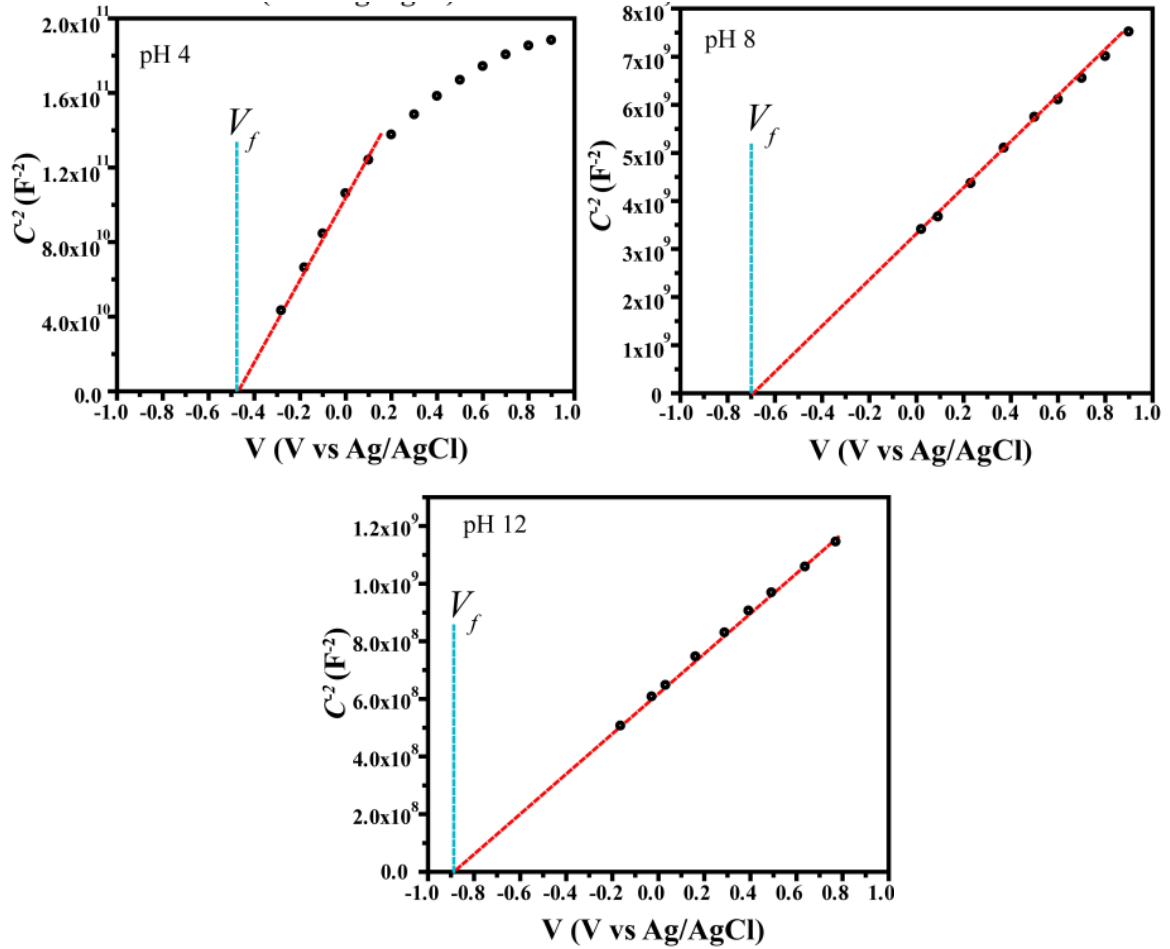
Fig.3. 7 Mott-Schottky plots obtained at pH 4, 8 and 12 for Ta_3N_5 thins films.

For an n-type semiconductor when negative biasing is applied the band bending decreases. For higher negative biasing a blocking potential arrives, where the space charge region is absent or more likely the semiconductor responds like a metal once the Helmholtz layer dominates the interface and the system under stake exhibits a lack of electrochemical dependence on the light illumination. At that instance the photocurrent onset is achieved and the applied potential is called flat band potential (V_f).[20] It can be seen from **Fig. 3.8**, the photocurrent onset i.e V_f strongly depends on the pH. In addition, the values estimated from the photocurrent onset corroborate the values obtained by Mott-Schottky curves of **Fig.3.7**.
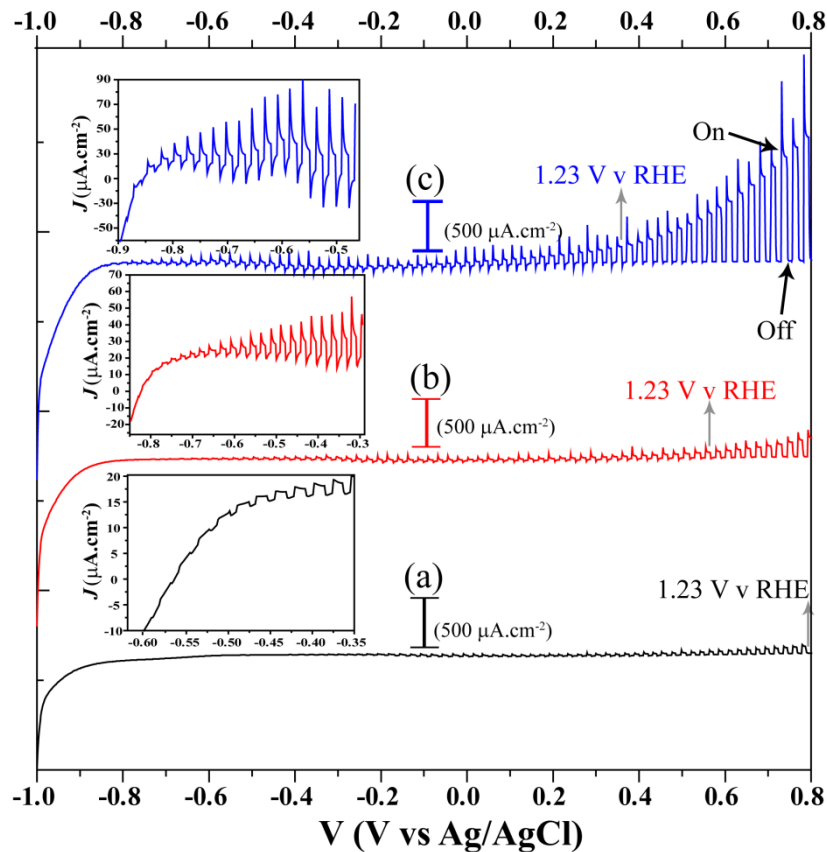
Fig.3. 8 Chopped LSV curves obtained at pH (a) 4 (b) 8 and (c) 12.

Furthermore, compared to other electrolytes, pH 12 presents an enhanced photocurrent. The conduction band minimum (CBM) of an n-type semiconductor is $0.1-0.3$V more negative than the V_f. [106] Therefore, adding -0.25V, the positions of CBM are calculated that were -0.46V, -0.70V and -0.89V at pH 4, 8 and 12, respectively.

3.3 Partial Conclusions

In this work, we described that Monoclinic Ta_3N_5 thin films can be synthesized by thermal nitridation of directly sputtered Ta_2O_5 thin films deposited by RF-magnetron sputtering on quartz substrate. From optical characterization, the dielectric constant of Ta_3N_5 film was found to be in between 7 and 9; which is in accordance to the previously reported theoretical values. Using the value of the dielectric constant, the effective density of states was calculated from the Mott- Schottky curves. The photoelectrochemical analyses revealed that the band structure of Ta_3N_5 strongly depends on the pH of the electrolyte. It was found that the enhanced photocurrent was observed in alkaline conditions.

CHAPTER 4

THE PRESENCE OF TRAPS IN THE STRUCTURE OF Ta_3N_5 NANOTUBES

4.1 Objectives

The solid state properties of an ideal semiconductor are modeled by the band theory where the forbidden region called bandgap separates the valence band (maximum oxidization power of photogenerated holes) and the conduction band (maximum reduction power of excited electrons). However, at semiconductor–electrolyte interface the electrode structure is different chemically and physically from the bulk. These inhomogeneities give rise to another density of states within the bandgap.[29,30,31] There have been numerous reports on quantifying and identifying these states employing variety of techniques including photocurrent transient,[32] dynamic PEC measurements,[33] impedance spectroscopy,[34] photoluminescence [35]. As an example, for nano-structured TiO_2 these states are associated with low coordinated Ti sites,[36,37,38] grain boundaries,[39] oxygen vacancies.[40] For hematite they are proposed to be Fe^{III}–OH/Fe^{IV}=O [41] and for GaN they are related to the morphology.[42] For some materials they act as current flow sites[43] and for others; recombination centers.[41] However, the exact nature of these states remains controversial.

Using semiconductor–electrolyte interface for overall water splitting, the semiconductor should straddle the redox potentials of water. It should be stable in aqueous electrolytes, absorb large fraction of visible light, separate the photogenerated charge carriers and collect them efficiently.[2,107] Apart from meliorating the optical and electronic properties, nanostructuring a semiconductor benefits the charge separation through lessening the distances that the minority carriers have to travel to the reactive sites.[108] In this regard, nanotubular semiconductors possess enormous potential for improved photocatalysis.[80,49] Nanotubes (NTs) of Ta_3N_5 have been employed for photoelectrochemical (PEC) water splitting.[13,12] However, the pristine Ta_3N_5 NTs have required the external biasing > 1.23V vs RHE to drive water oxidation.[14,17] In addition, not only the NTs but also the pristine Ta_3N_5 photoelectrodes have been adversely affected without co-doping and loading co-catalysts.[9,16,109] In standard electrolytes such as Na_2SO_4 and NaOH; the photocurrent overshoot to spikes and decreased momentarily presenting instability and sluggish water oxidation.[110,111] On the other hand, Ta_3N_5 photoelectrodes when used in $Fe(CN)_6^{3-/4-}$ (aq) presented an improved as well as stable PEC activity.[112,113,53] Furthermore, for other devices such as hematite the $Fe(CN)_6^{3-/4-}$ has been found to be efficient sacrificial agent.[41] Now, the question arises why

pristine Ta_3N_5 photoelectrodes utilized in standard electrolytes without adding a sacrificial reagent result in a poor PEC activity. Therefore, a detailed investigation is warranted to understand the Ta_3N_5 NTs-electrolyte interface.

Herein, we study and compare semiconductor–electrolyte interfacial properties of pristine Ta_3N_5 nanotubes in standard Na_2SO_4 (aq) electrolyte [13] and the one containing sacrificial reagent of $Fe(CN)_6$ $^{3-/4-}$ (aq). Thorough photoelectrochemical investigations are provided to understand the necessity of higher onset potential for improved water splitting. To compare our findings to the literature, we have focused our study on the pristine Ta_3N_5 NTs obtained at 800°C for a nitridation time of 3 h or otherwise noted.[13] Henceforth, for the sake of simplicity we will name standard Na_2SO_4 (aq) electrolyte as Water and the sacrificial reagent as $Fe(CN)_6$ $^{3-/4-}$ (aq).

4.2 Results and discussion

4.2.1. Morphology and structure

4.2.1.1 The as-anodized Ta_2O_5 nanotubes prepared in the current study

Fig.4.1a shows J-t curves obtained during anodization carried out for voltage ramps of 1, 5, 10, 25 and 50 V/s to a constant value of 50 V during 20 minutes. The temperature during the anodization was kept constant at 10°C. In the J–t curves (**Fig.4.1**) one can observe a maximum current of ca. 200 mA/cm^2 at the beginning of the process, followed by a sudden drop to a constant current density of 8 mA/cm^2, which is a characteristic behavior of anodization process. This behavior is related to the formation of a Ta_2O_5 barrier on the Ta substrate due to Ta oxidation in the acidic solution. In fact, all the J-t curves presented similar feature, except for anodization carried out by ramping of 1 V/s (**Fig.4.1a**) that will be explained later. It can be seen that J-t curves for ramping of 5 – 50 V/s are simply overlapped from which it can be inferred that the morphology of the NTs obtained under these conditions can not differ from each other. **Fig. 4.1b** shows the anodization curves obtained by using 10 V/s of ramping until 50 V during 5, 10 and 20 minutes and the overlapping can be confirmed too for the NTs obtained for different times of anodization.
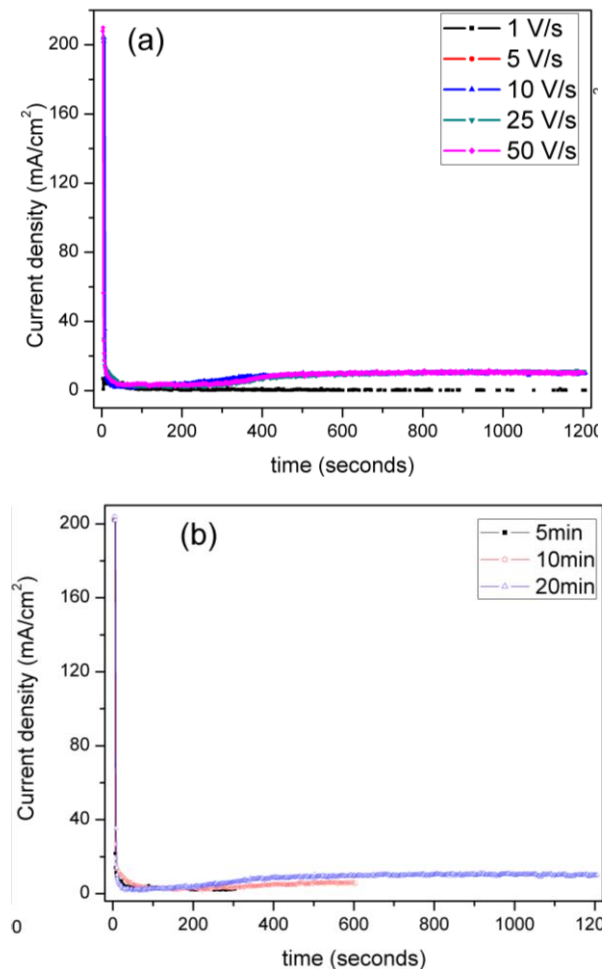
Fig.4. 1 J-t curves of 50V of anodization under (a) different scan rates at fixed anodization time of 20 min, (b) fixed scan rate of 10V/s for different times of anodization.

It can be seen that the J-V curves present the same current densities. SEM images of as-anodized samples were obtained from the scratched area of the oxide layer. From the SEM images (not shown); the magnitudes of diameter, length and wall thickness of the NTs prepared at different ramping rate from 5 V/s to 50 V/s were not influenced by the ramping. **Fig. 4.2** displays the SEM and TEM images of the nanotubes obtained during anodization carried out for voltage ramps of 10 V/s to a constant value of 50 V during 20 minutes. The NTs are vertically oriented and the average length, outer diameter and wall thickness are 1.60 μm, 130 nm and 34 nm, respectively. It can be seen that the walls of the NTs are smooth The J–t curve and the geometric parameters of the Ta_2O_5 NTs prepared at 10 V/s to a constant voltage of 50 V during 20 minutes are consistent with the literature. [49]
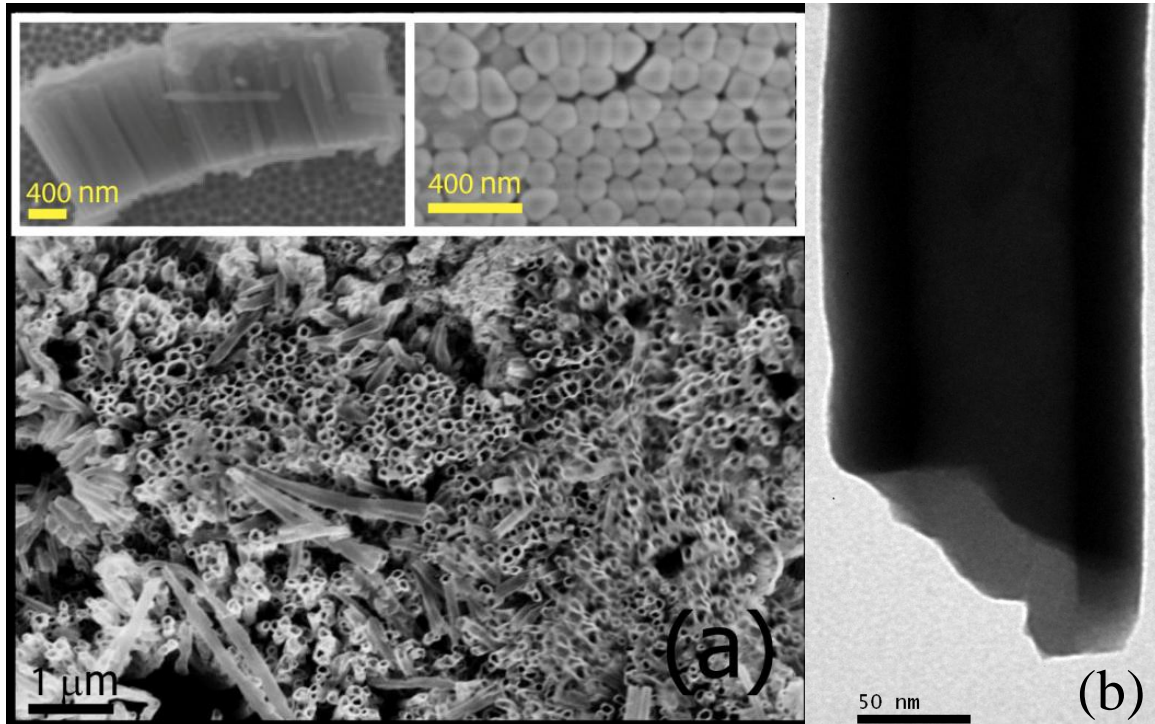
Fig.4. 2 SEM (a) and TEM (b) images of as – anodized Ta_2O_5 nanotubes/Ta obtained by a voltage ramping of 10 V/s to a constant value of 50 V during 20 minutes.

Fig.4.3 displays the SEM images of the Ta_2O_5 NTs anodized for 5 and 10 min, presenting length of ca. 460 nm and ca. 900 nm, respectively and the wall thickness and the tube length were almost the same as been observed for 20 min of anodization time. These results are in line to the literature where the length of the Ta_2O_5 nanotubes in H_2SO_4/HF electrolyte was found increased upon increasing the anodization time.[79]
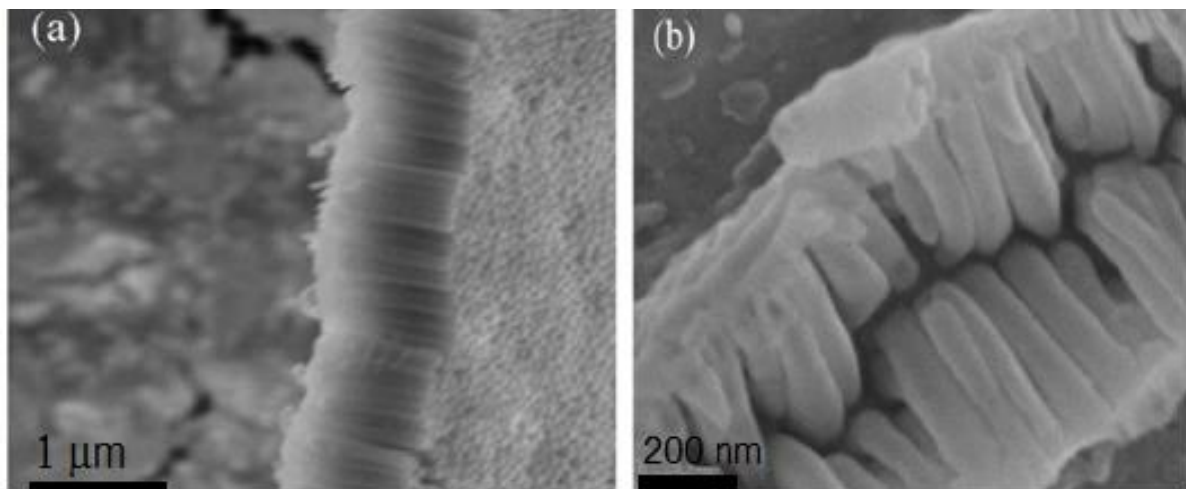
Fig.4. 3 SEM images of Ta_2O_5 NTs obtained by (a) 10 min and (b) 5 min of anodization time by 10 V/s ramp to constant voltage of 50 V.

The estimated geometrical parameters of the nanotubes are displayed in **Fig. 4.4** that shows the average length of nanotube increases with increasing anodization time, but the average outer diameter and wall thickness of nanotube are not affected for experiments conducted with the same applied anodization voltage. These results corroborate the literature.[114]
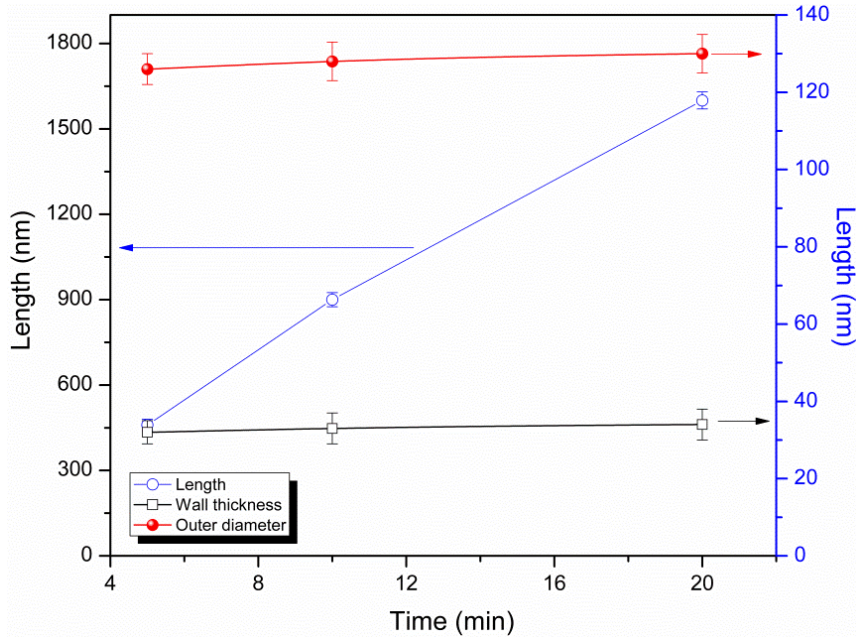
Fig.4. 4 Variation of length, diameter and wall thickness of Ta$_2$O$_5$ NTs with anodization time.

As mentioned earlier in this section, the J-t curve for anodization performed under 1 V/s of ramping presented a different behavior as compared to the other curves (**Fig. 4.1a**). In order to further investigate this result we have obtained SEM images of the sample (**Fig.4.5**). It can be seen that under the applied conditions the nanotubes could not be formed, instead one can observe the formation of nanodimples on the tantalum surface.[79] As we have discussed earlier in **Section 1.8,** during anodization process the high etching rates will not favor the growth of regular NTs instead the forming oxide layer will be dissolved into the acidic electrolyte. For 1 V/s ramp it takes 50 seconds to reach 50 V, which results in a very slow growth of the Ta$_2$O$_5$ layer in the first step of the anodization process, due to low electric field. When the applied potential reaches the value of 50 V, the templates for the nanodimples will already be formed on Ta surface and these templates will hinder the growth of oxide layer. [77] Therefore, further anodization process will be dominated by etching rates as compared to oxide formation rates, resulting into the conversion of the templates into the dimples (**Fig.4.5**).
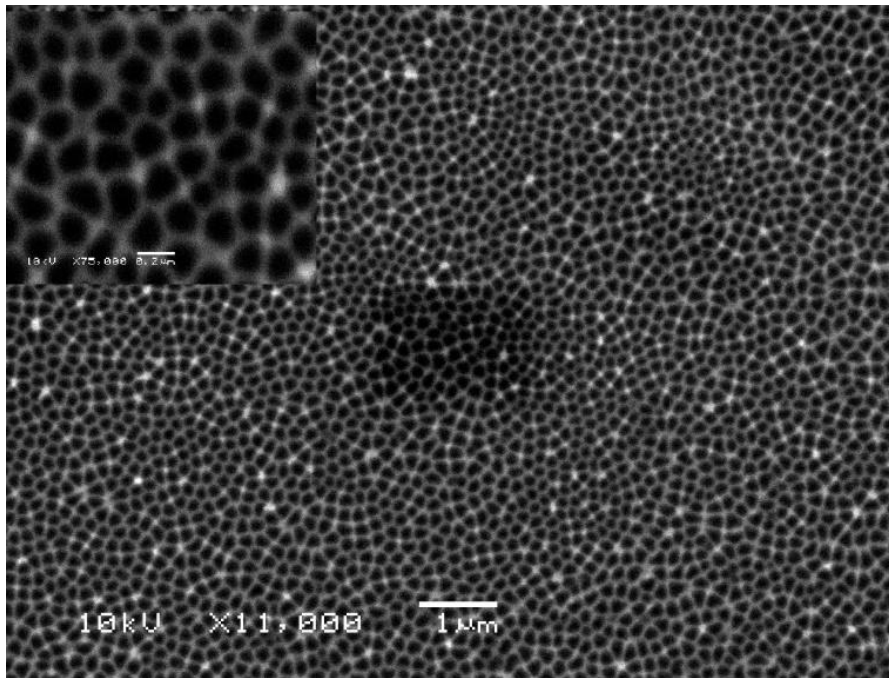
Fig.4. 5 SEM image of nano-dimples formed on the Ta surface at ramping of 1 V/s.

The anodization time will enable the dimples to grow in diameter and due to the strong stress among the neighbor dimples the diameter would be equalized. In simple words 1 V/s ramping of anodization results into the electropolishing of the Ta surface in the form highly regular dimpled surface. Moreover, it has been reported that the dimpled tantalum is ductile, highly melting, and chemically inert, and they can easily be used as a mold for nanostructure synthesis. [77,81] One of the most important parameters to be considered when applying nanotubes as photoanodes for photoelectrochemical cells is their adherence on the substrate. According to the literature, for the anodization of Ta_2O_5 nanotubes conducted in H_2SO_4/HF electrolyte, the adherence of the nanotubes on the substrate can be controlled by the temperature of the electrolyte during the synthesis.[49] Ta_2O_5 NTs start to adhere at 20°C and further increase in adherence is obtained by decreasing the medium temperature. Along with the adherence, decreasing the temperature increases the wall thickness of the nanotubes. In addition for TiO_2 NTs the literature describes an enhancement in photoelectrochemical activity from samples anodized at low temperatures.[115] According to previous work for the transformation of Ta_2O_5 nanorods into Ta_3N_5 under high temperature during nitridation, the morphology was preserved due to their strong adherence on the substrate.[9] Based on the above discussion, we can assume that Ta_2O_5 NTs should be well adhere to the substrate in order to obtain Ta_3N_5 NTs conserving the tubular morphology at higher temperatures. Hence, we might expect that the Ta_2O_5 NTs prepared at low temperature of 10°C that are vertically

oriented, well adhere and thick walled would withstand to higher temperatures under ammonia flow, resulting in Ta_3N_5 NTs with improved crystallinity and enhanced photoelectrochemical performance. [13, 49]

4.2.1.2 The Ta₃N₅ nanotubes prepared by nitridation at 800°C for 3h

Fig. 4. 6 displays the morphology of the Ta_3N_5 nanotubes (NTs) synthesized at the nitridation temperature of 800°C for 3h. The average length and pore size of the NTs are 1.4 µm and 30 nm; respectively. Furthermore, the HRTEM image displays the d–spacing of 3.6 Å in agreement with the (110) plane of the orthorhombic Ta_3N_5 crystalline structure. The XRD patterns of **Fig. 4. 7a** match with the JCPDS card no: 79-1533 i.e. orthorhombic crystalline phase of Ta_3N_5 corroborating the HRTEM results. From Rietveld refinement (See Section 5.2.2) the average overall grain size was found to be 19.7 nm. It was found that the nitridation results in to nitrogen vacancies in the crystalline structure of Ta_3N_5 NTs. In addition, 3-coordinated nitrogen atoms have shown oxygen substitutions; and the nominal stoichiometry estimated from the Rietveld refinement for the sample was found to be $Ta_{2.89}N_{4.18}O_{0.84}$. These results clearly indicate that the nitridation is a defect generative process. These defects can influence the water splitting activity of the photoelectrode.
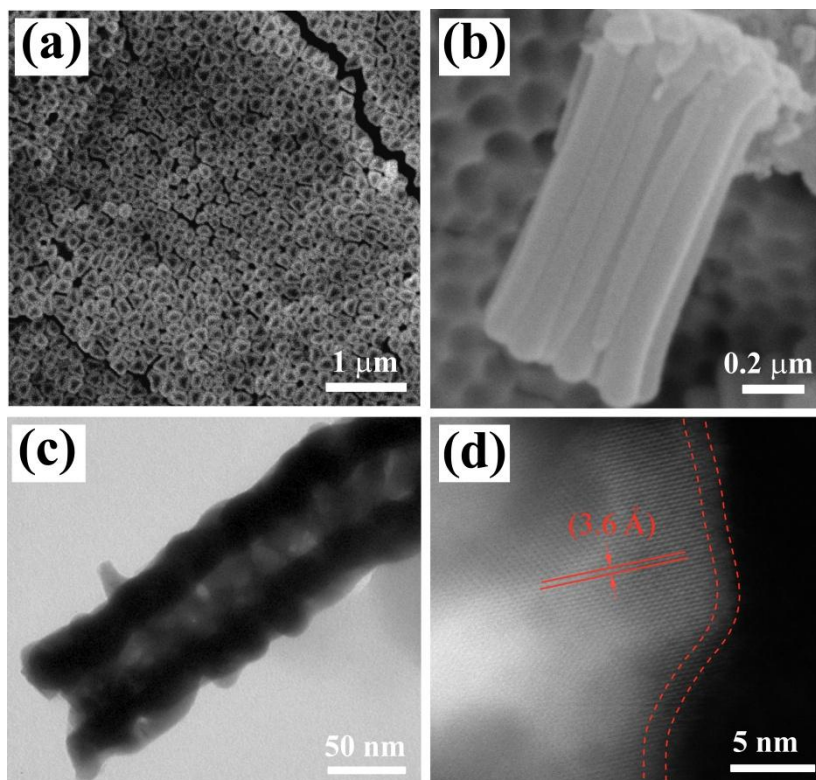
Fig.4. 6 SEM images; (a) and (b). TEM image (c) and HRTEM micrograph viewed along [1-10] zone axis (d) for Ta_3N_5 NTs.

Furthermore, thermal nitridation has red-shifted the band edge from Ta_2O_5 NTs (ca. 320 nm) to Ta_3N_5 NTs (ca. 600 nm) (**Fig. 4. 7b**). One can observe a broad absorption mode above ca. 600 nm for Ta_3N_5 NTs which is attributed to the formation of defects such as reduced tantalum species Ta^{4+}.[73a,8] Dabirian and Van de Krol have attributed this region to the ionic defects.[59] In addition, along with the main transition; the UV-Vis spectrum of Ta_3N_5 NTs displays a shoulder at ca. 540 nm related to the oxygen content in the Ta_3N_5 structure. It may be expected that the presence of these defects give rise to the recombination centers for photogenerated carriers. The optical bandgap for Ta_3N_5 NTs is 2.1 eV consistent with the previous report.[56] To further confirm the bandgap, we have performed chronoamperometry under monochromatic irradiation in Water (**Fig. 4. 7c**).
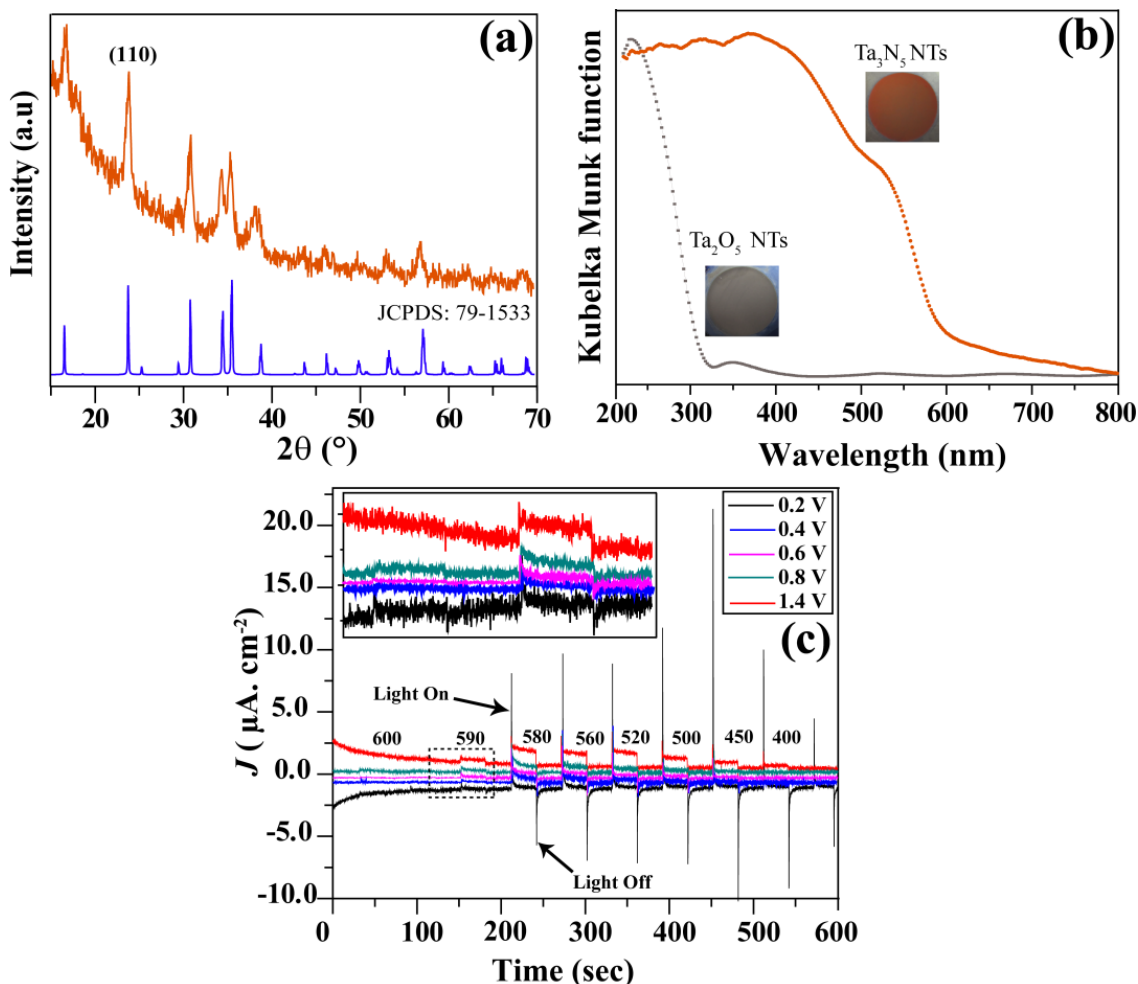
Fig.4. 7 Grazing angle XRD diffractogram of Ta_3N_5 NTs (a), UV-Vis spectra of Ta_2O_5 and Ta_3N_5 NTs (b) and Chronoamperometry of Ta_3N_5 NTs obtained as a function of applied biasing and monochromatic irradiation in Water (c)*.

* For Chronoamperometry, the sample was left under dark for 25 sec and chopped to irradiation for 25 sec each consecutively; the wavelengths (in nm) of the incident radiations are displayed next to each chopped curve.

The sample has started to respond for the photocurrent at ca. 590 nm (Inset of **Fig 4.7c**). This result shows that the photon of 2.1 eV is energetic enough to excite the electron from valence to the conduction band of Ta_3N_5 NTs thereby resulting in to photocurrent corroborating the optical bandgap value obtained by UV-Vis analysis. Furthermore, for each applied potential similar bandgap was observed; however, the photocurrent increases with increasing biasing. In addition, for lower potentials prominent spikes can be observed that presents higher recombination of the photogenerated carriers. These results suggest the application of higher biasing for improved photocurrent; however, the bandgap is the same at all applied potentials. [44,116,117]

4.2.2. Linear sweep voltammetry and Chronoamperometry

Fig. 4. 8a & 8b contrasts the linear sweep voltammetry (LSV) curves of pristine Ta_3N_5 NTs photoanode obtained by chopping AM 1.5G (1 Sun) illumination in Water and $Fe(CN)_6^{3-/4-}$ (aq). Compared to $Fe(CN)_6^{3-/4-}$ (aq) larger biasing potential is applied in Water; however, enhanced photocurrent can only be observed in $Fe(CN)_6^{3-/4-}$ (aq). These results suggest low hole transfer ability of Water to sustain the Faradic current for pristine Ta_3N_5 NTs. In addition, upon turning the light On one can observe "overshoot" transient anodic spikes, decaying momentarily (**Fig. 4. 8a**) resulted from the recombination of photogenerated electron-hole pairs. Furthermore, upon light interruption, sharp transient cathodic spikes are also observed that are more prominent at lower potentials. These results agree in essence with the earlier reports; as the cathodic spikes have been observed at lower biasing in J-V curves for pristine Ta_3N_5 photoanodes in standard electrolytes; however, origin of these spikes was not explained. [111,118,119,120,121] Under illumination the migration of photogenerated holes to the interface decreases the band bending and in the presence of intermediates the photogenerated holes will be trapped.[44] Immediately after light interruption, the electrons from the conduction band overcome relatively low energy barrier; thereby, reducing the trapped holes and produce transient cathodic peaks. The cathodic spikes have been observed for other semiconductors such as hematite,[44] $n-TiO_2$[116] and n-CdTe [117] and have been attributed to the reduction of the trapped holes. Interestingly, under higher positive potentials, the appearance of cathodic spikes is minimized since the applied potential is high enough to induce a strong electric field at the interface to increase bulk/surface energy improving electrons transportation. Therefore,

higher positive biasing separates the photogenerated charge carriers and decreases the hole trapping; thereby promoting water oxidation. In addition, in $Fe(CN)_6^{3-/4-}$ (aq) (**Fig. 4. 8b**) the absence of anodic and cathodic spikes show that the hole collection efficiency of $Fe(CN)_6^{4-}$ is very high. The result of hole trapping in Water is the non-reproducibility of photocurrent since the LSV curves obtained with and without light chopping do not overlap (**Fig. 4. 8a**). On the other hand, these curves overlap in $Fe(CN)_6^{3-/4-}$ (aq) (**Fig. 4. 8b**). The discrepancy of photocurrent compared to $Fe(CN)_6^{4-}$ and the non-reproducibility of LSV curves in Water absolutely indicate the presence of trapping states at Ta_3N_5–Water interface. The scanning voltage perturbation in LSV measurements offer a continuous band bending at the semiconductor–electrolyte interface. To obtain further insight towards water oxidation the photocurrent transient decay was deconvoluted using Chronoamperometry method in Water.
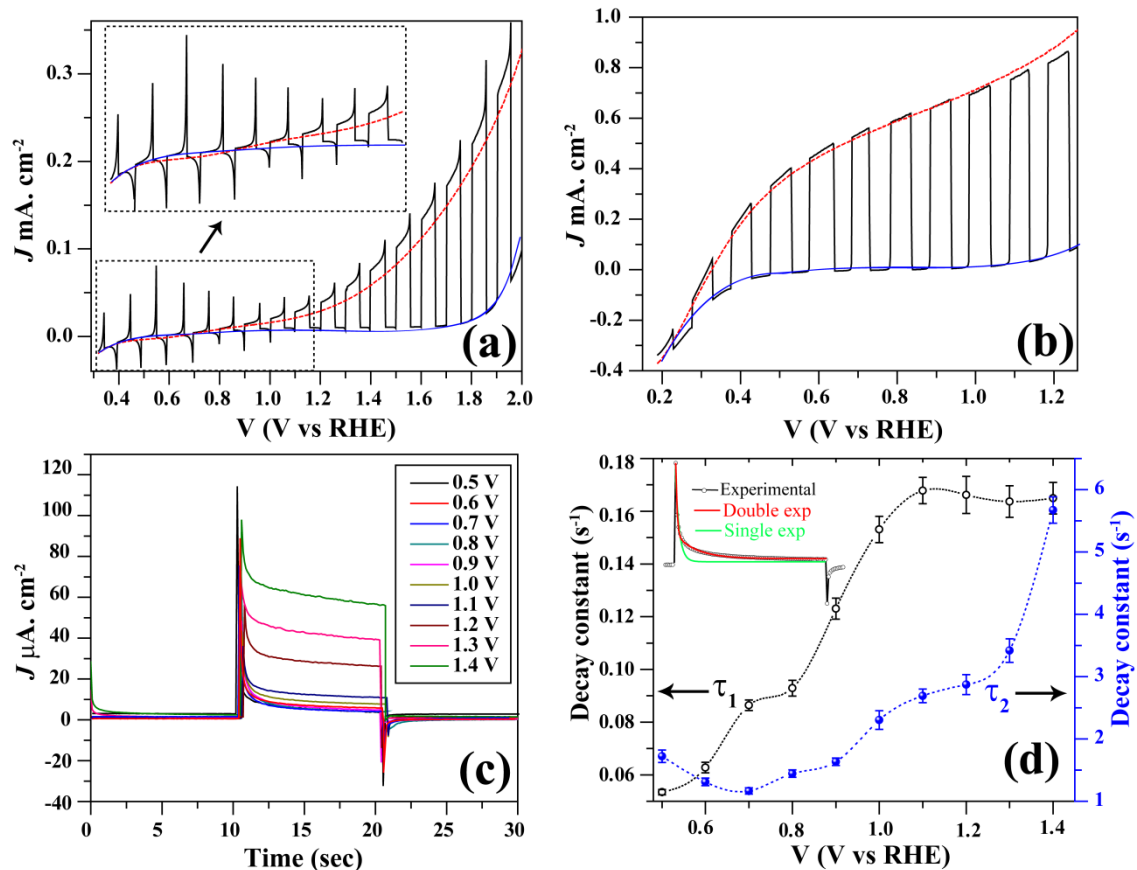
Fig.4. 8 LSV curves of pristineTa_3N_5 NTs obtained in Water (a) and (b) $[Fe(CN)_6]^{3-/4-}$(aq). Chronoamperometry of pristine Ta_3N_5 NTs obtained in Water (c) and their decay constants (obtained by double exponential curve fittings) vs applied potential against RHE*.

*The photoanode was left under dark for 10 seconds at fixed applied potential vs RHE, and after illuminating (AM 1.5G) for 10 s the light pulse was chopped off.

The measurements were performed applying constant potential (fixed band bending) as a function of time, in response to anodic (On) and cathodic (Off) current transients (**Fig. 4. 8c**). The shape of the transients photocurrent curves markedly differ from the ideal square response. The value of transient photocurrent and the rate of decay seem to present a strong dependence on the applied potential. Low biasing potential results in large anodic and cathodic spikes and a dramatic decay of photocurrent (**Fig. 4. 8c**). On the other hand, for high positive potentials the decay is nominal and cathodic spikes are minimized and the photocurrent is improved as well. In the literature, for many other semiconductors transient photocurrent curves have been examined by fitting the decay to a mono-exponential function.[32,122,123,124] However, for pristine Ta_3N_5 NTs good fits were achieved for the double exponential function using equation 4.1 (plotted in the inset of **Fig. 4. 8d**); composed of two relaxation processes with time constants τ_1 and τ_2.

$$J_{ph} (t) = J_{ph}(\infty) + J_{ph}(0)_1\, e^{-t/\tau_1} + J_{ph}(0)_2\, e^{-t/\tau_2} \qquad (4.1)$$

Where; $J_{ph}(\infty)$ represents the steady state current reached after full decay of these two processes and $J_{ph}(0)_1$ and $J_{ph}(0)_2$ correspond to their initial values. Physical meaning of these processes can be rationalized by the knowledge of other semiconductor devices. One of the relaxation process is related to the recombination of the free electron-hole pairs that is faster and the second process which is quite slower is related to the lattice relaxation of the trapping states.[32,41,125,126] **Fig. 4. 8d** compares the time constants obtained by equation 4.1 from the photocurrent transients of **Fig. 4. 8c** that differ remarkably from each other in order of magnitude. Both of them increase with the applied potential; however, from ca. 1.1V to more positive potentials $\tau_1(s^{-1})$ saturates but $\tau_2(s^{-1})$ keeps increasing. Furthermore, $\tau_1\ (s^{-1})$ is slower and $\tau_2(s^{-1})$ is faster. It can be seen that at lower potentials both of these processes last longer. These results suggest that the recombination and hole trapping is phenomenal at lower potentials. When the applied potential increases, initially the traps with highest relaxation probability undergo relaxation process, therefore, those states that are not neutralized are still accessible for the electrons of the conduction band thereby presenting cathodic spike upon light interruption.[126] Once the majority of the traps have undergone the relaxation with a higher energetic barrier at sufficiently large positive potentials the water oxidation will be improved; thereby the time constant τ_1 saturates and the cathodic spikes will not be observed. These analyses corroborate the appearance of cathodic spikes observed at lower potentials in **Fig. 4. 8a**. Furthermore, from the increasing nature of τ_2 w.r.t the applied potential it can be

inferred that the recombination of the photogenerated carriers is not completely inhibited; matching the appearance of anodic spikes obtained at all applied potentials in **Fig. 4. 8a**; however, at lower potentials recombination is high as the anodic spikes are bigger too. Hence, from the LSV and transient photocurrent curves; hole accumulation can be confirmed in Water upon light irradiation. On the other hand, in case of $[Fe(CN)_6]^{3-/4-}$(aq) i.e efficient hole scavenger; the photocurrent is not only improved but also the anodic as well as cathodic spikes do not appear (**Fig. 4. 8b**). Therefore, for Ta_3N_5 NTs, efficient hole scavenging from its surface is a key factor to improve its PEC activity. Hence, it can be inferred that first step for actual water oxidation using pristine Ta_3N_5 NTs is the relaxation of the traps and higher positive biasing is necessary to comply that. Unfortunately, necessary voltage drop for these trapping events is not feasible as the applied biasing should not rise above 1.23 V vs RHE for the efficient solar energy conversion.

4.2.3. Cyclic voltammetry

To investigate the location of these traps; the cyclic voltammetry (CV) runs were performed in Water and $[Fe(CN)_6]^{3-/4-}$ (aq) at various scan rates. For cathodic scans in Water from ca. 0.7 V toward more negative potentials, the current starts to increase along with the appearance of peaks; a small local peak at ca. 0.5 V (Peak I) followed by a distinctive peak at ca. 0.2 V (Peak II) (**Fig. 4. 9a**). Once the scan direction is reversed two peaks appear; Peak III at ca. −0.1V followed by an anodic peak (Peak IV) at 0.25 V. The heights of the peaks as well as their positions change with the scan rates except for peak III for which the respective cathodic peak is not observed during the cathodic scan. Therefore, it's no merely be related to the water redox process (water reduction at 0 V vs RHE) but also to the charging of distribution of states.[127] Peak II and Peak IV appear to be filling and depopulation of the trapping states. When the CV is performed under illumination the peak I hardly visible under dark becomes more distinctive (**Fig. 4. 9b**). The Peak IV gets broader under illumination and the other peaks have been shifted from their previous positions under dark showing light activation dependence of the trapping states. It has been known that when cathodic scan is carried out Fermi level shifts up and gets closer to the conduction band and traps that exist on the semiconductor will be filled by electrons inducing the first cathodic peak.[128,129] Under dark slight invisibility of Peak I implies that the trapping states are partially filled with electrons, while under illumination, these traps are depopulated by holes allowing higher charge accumulation that makes it more distinctive. If the trapping is fast and detrapping is

slow the respective anodic peak will not appear that is the case of Peak I.[59] Its shape after illumination indicates not only the slow charge transfer from the traps, but also shows a sluggish detrapping thereby actuating recombination centers to limit oxygen evolution and implying higher biasing potential.[42, 130]
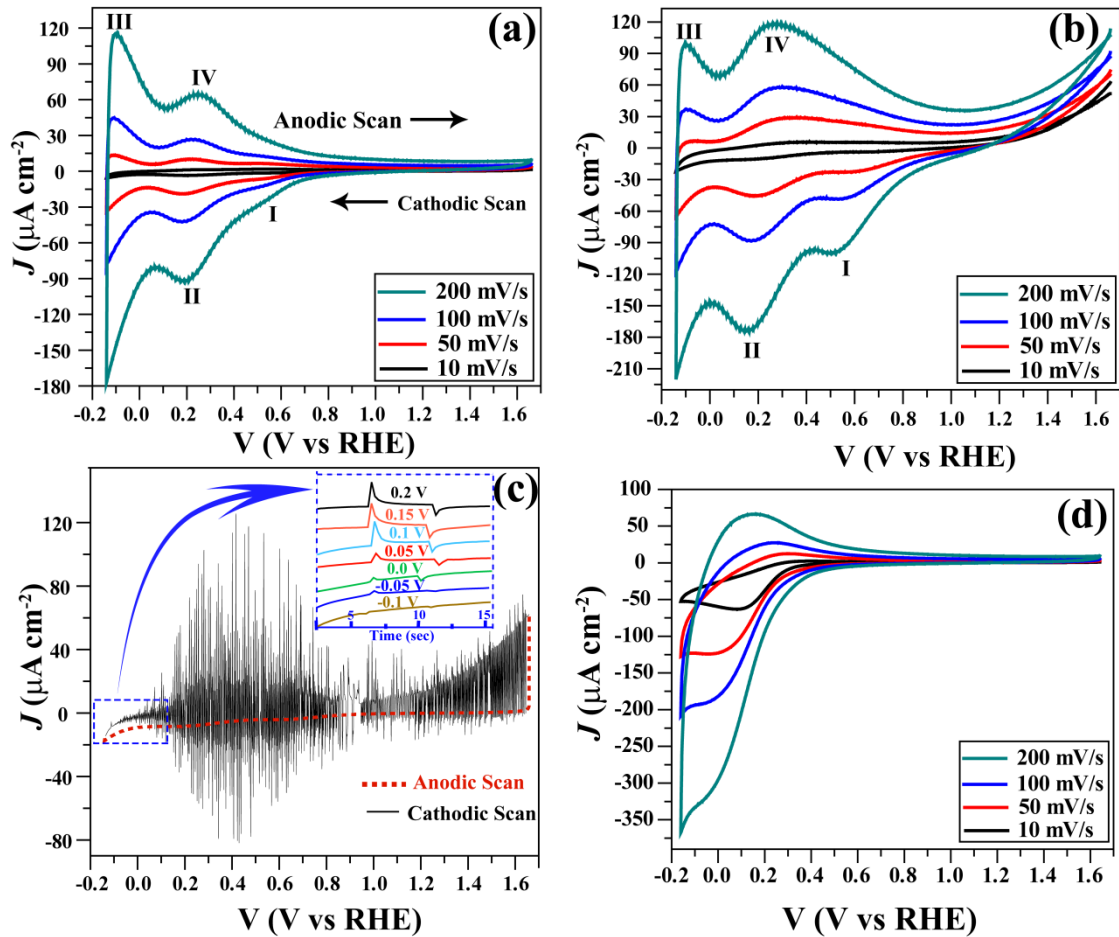
Fig.4. 9 Cyclic voltammetry curves of pristineTa$_3$N$_5$ NTs (a) in Water under dark, (b) under AM 1.5G (1 Sun) continuous illumination and (c) 1.5G (1 Sun) Chopping at 10 mV/s scan rate and (d) in Fe(CN)$_6$ $^{3-/4-}$ (aq) under dark.

Therefore, this process is not desirable for PEC devices because it implies higher applied potential. The case where the detrapping is comparable to the velocity of charging the trapping states, reversible peaks appear that is the case of Peak II with its counterpart (Peak IV) where the traps are more likely in equilibrium with the conduction band.[130] Furthermore, the intensity of peak I, Peak II and Peak IV present a quasi–linear dependency to the scan rate under illumination; suggesting an additional circuit component related to the trapping states for pristine Ta$_3$N$_5$ NTs under water oxidation conditions.[44] The findings on the trapping states

are further confirmed by CV runs of **Fig. 4. 9c** performed in a novel fashion at 10 mV/s of the scan rate, the red colored dotted line is the anodic scan. Once the cathodic scan starts, a high frequency light chopping was performed. It can be seen that at lower applied biasing the spikes are highest in magnitude, on the other hand at higher applied potentials they decreases and water oxidation improves. These results further confirm that at lower potentials the trapping states are highly activated and to depopulate them higher biasing is needed corroborating the analyses of **Fig. 4.7c** and **Fig. 4.8 (a & c)**. A striking feature of **Fig. 4. 9c** is the photocurrent onset that was observed at ca. –0.05 V highlighted in the figure by blue colored dotted box at the negative vertex of the CV; that yields the flat band (E_{fb}) position of Ta_3N_5. And same E_{fb} position was observed by deconvolution of the potentials applying chronoamperometry as the Light dependence PEC activity almost disappears for the potentials that lie in between –0.05 and 1 V (Inset of **Fig. 4. 9c**).

By considering the above discussion it can be suggested that due to the presence of trapping states the holes accumulation on Ta_3N_5 NTs will result in sluggish water oxidation. Under water oxidation conditions for long time irradiation these holes will induce self-oxidation of pristine Ta_3N_5 NTs due to releasing the lattice nitrogen thereby devastating the PEC activity. [131] Therefore, the photocurrents will not be reproducible for the new scans in LSV curves (**Fig. 4. 8a**).When the CV runs were performed in $Fe(CN)_6{}^{3-/4-}$ (aq) for pristine Ta_3N_5 NTs; no distinctive peaks are observed that further confirms the trapping states are related to water oxidation conditions. From the two peaks observed in the CV runs in Water it can be suggested that there are two types of species that act as trapping states for Ta_3N_5 NTs and one of which offers large recombination centers and these states present a strong dependence on illumination. However, what exactly are these species; demands further investigations. The suitable candidate species seem to be related to the formation of Water intermediates that are incorporated to the reduced Ta species such as Ta^{4+}, [132] and/or with oxygen content in the lattice and around the NTs borders, [95,68]. In the literature, for TiO_2 the species such as Ti^{4+} presented just the cathodic peak in CV, however, respective anodic peak was not observed.[38] On the other hand for Ta_3N_5 the incorporated Co ions have proposed to decrease the Ta^{4+} defects that not only enhanced the gap-transition absorption but also improved the PEC performance of Ta_3N_5.[132] Therefore, we suggest that Peak I is related to the reduced Ta species and Peak II is more reasonably related to the oxygen content in Ta_3N_5. [68]

4.2.4. Electrochemical Impedance Spectroscopy

The defects originated due to thermal nitridation play an important role in the PEC activity of Ta_3N_5 NTs. Schottky defects of nitrogen confirm the n-type semiconducting behavior as well as resulting in to reduced Ta species in the adjacent sites. For photoelectrochemical water splitting, the flat band position of the semiconductor is one of the most important parameter that helps to predict whether semiconductor should be biased externally or not. One of the most widely used technique to estimate the flat band of a semiconductor is the Mott-Shottky plot. [133] The Mott-Schottky plots not only confirm the type of the semiconductor but also provide the doping density.[26a, 20, 134] According to the Mott-Shottky approximation under depletion conditions, the extrapolation of $1/C^{-2}$ vs V gives the flat band of the semiconductor at the X-intercept where $1/C^{-2}$ is zero. Positive slope of the Mott-Shottky is a characteristic of an n-type semiconductor; whereas the negative slope presents a p-type semiconductor. Another important parameter extracted from the Mott-Shottky plot is the density of states N_D. The Mott-Shottky relationship is as follows;

$$\frac{1}{C^2} = \frac{2}{\varepsilon\varepsilon_0 A^2 e N_D} \left(V - V_{fb} - \frac{K_b T}{e}\right)$$

(4.2)

Where:

C = space charge capacitance.

e = electronic charge = 1.6×10^{-19} C

ε = dielectric constant of the semiconductor = 8 for Ta_3N_5. (see **Fig. 3.5**)

ε_0 = vacuum permittivity = 8.85×10^{-14} C V^{-1} cm^{-1}

V = applied potential

K_b = Boltzmann constant = 1.38×10^{-23} m^2 kg s^{-2} K^{-1}

A = area shown to the electrolyte.

V_{fb} = flat band potential.

Fig. 4. 10 contrasts the Mott-Schottky plots obtained for pristine Ta_3N_5 NTs in Water and $Fe(CN)_6$ $^{3-/4-}$(aq)   at various frequencies. From the positive slope of the plots; n-type semiconducting behavior can be confirmed. On each graph the flat band potential (E_{fb}) was obtained by extrapolation of the linear region presented as a bordeaux red colored solid line.
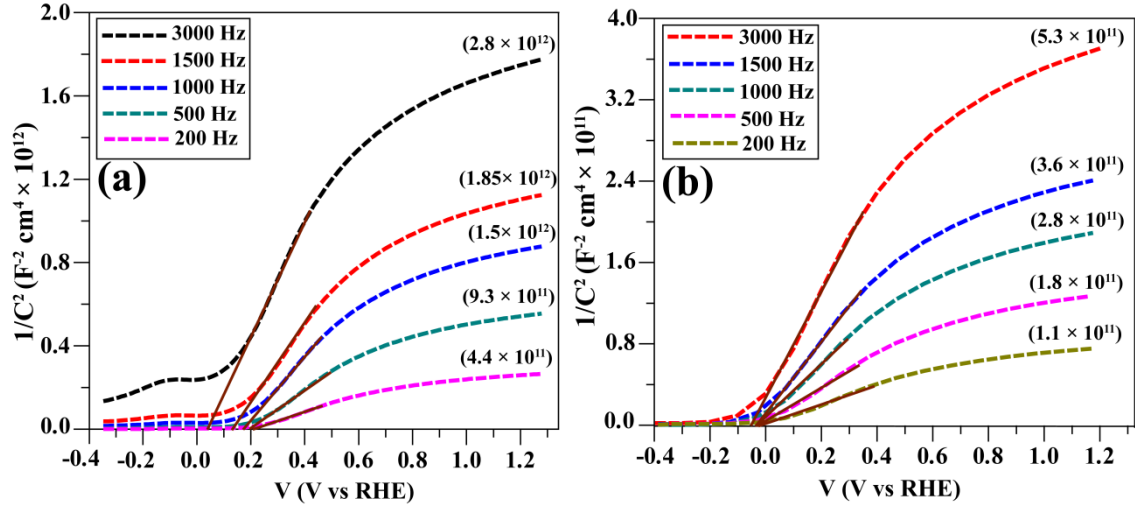
Fig.4. 10 Mott-Schottky plots of pristineTa$_3$N$_5$ NTs in (a) Water and (b) Fe(CN)$_6$$^{3-/4-}$(aq).

It can be seen in **Fig. 4. 10** that the intercepts for the flat band (E$_{fb}$) potentials do not converge at one point in Water. Previously in the literature; for pristine Ta$_3$N$_5$ NTs in Water the Mott-Schottky plots presented frequency dispersion and origin of that was not explained.[13] From the analyses of LSV and CV curves the frequency dependence of E$_{fb}$ in Water can be clearly related to the trapping states.[135] In addition, the position of the E$_{fb}$ obtained by Mott-Schottky curves is different than the photocurrent onset observed in **Fig. 4. 9c**. These results show that for pristine Ta$_3$N$_5$ NTs immersed in Water; utilizing simplified equivalent circuit (R$_s$–C$_s$) for Mott-Schottky curves do not generate reliable values of the E$_{fb}$. Therefore, further investigations are required to obtain the correct values of the E$_{fb}$ for Ta$_3$N$_5$ NTs immersed in Water. On the other hand, for Fe(CN)$_6$$^{3-/4-}$(aq) the E$_{fb}$ potentials seem to be independent of the applied frequencies and almost converge to one value i.e. –0.05±0.03 V corroborating the obtained E$_{fb}$ by photocurrent onset in CV run of **Fig. 4. 9c**.

If we consider the tubular morphology of a sample it is important to note that the real surface area of the nanotubes is different than the area in contact with the electrolyte. As the nanotubes are attached to the Ta substrate, it is difficult to do Brunauer Emmett Teller (BET) measurements for the surface area. Therefore, we have estimated the effective surface area utilizing the geometric parameters of the NTs. Assuming an idealized nanotubular structure with inner diameter D, wall thickness W, and tubular length L, the roughness factor can be calculated as; [136]

$$1 + \left[\frac{4\pi L(D + W)}{\sqrt{3}(D + 2W)^2} \right] \qquad (4.3)$$

Above equation assumes that the nanotubes are perfectly smooth. In reality, the NTs are not smooth therefore the roughness factor of the real NTs would be different. Using L = 1.4 μm, D = 72 nm and W = 30 nm, we have estimated the roughness factor equal to 60 for our NTs. Therefore effective electrode area would be;

$$\text{Effective electrode area} = \text{Roughness factor} \times \text{Area of the electrode} \qquad (4.4)$$

Generally, the slope of the Mott-Schottky curve can be written as follows;

$$Slope = \left[\frac{2}{\varepsilon\varepsilon_0 A^2 e N_D}\right] \qquad (4.5)$$

where A is the area of the electrode shown to the electrolyte normalized to 1 cm^2. Considering the roughness factor of the NTs, the area presented in the slope of the Mott-Shottky equation would be replaced by the effective electrode area i.e.;

$$Slope = \left[\frac{2}{\varepsilon\varepsilon_0 (\text{effective area})^2 e N_D}\right] \qquad (4.6)$$

In the current case that effective area is 60 cm^2. In simple words, for the geometric area of 1 cm^2, the real surface area will be 60 cm^2. Therefore, using the equation 4.6 we have estimated the value of N_D. Recently in the literature, similar procedure has been followed to estimate the effective surface area for the TiO$_2$ NTs.[137,138] The slopes, E_{fb} potentials, effective donor densities (N_Ds) and the open circuit potential (V_{oc}) values obtained for all curves are summarized in **Table 4.1**. The values of N_D obtained here are in accordance to those suggested for the semiconductor devices .[83] Furthermore, both of the electrolytes have almost the same pHs; however, compared to Water the N_D values are higher in Fe(CN)$_6$$^{3-/4-}$(aq) and that can be related to different chemical compositions at the semiconductor–electrolytes interfaces. Nevertheless, the V_{oc} values are also different and the reason of that might be the flat band position in Water. The square of the depletion region width for Semiconductor–electrolyte interface is inversely proportional to the N_D. Based on the higher N_D values in Water the depletion region width is thicker than in Fe(CN)$_6$$^{3-/4-}$(aq); result of that will be higher mobility of the charge carriers that might improve the PEC performance in Fe(CN)$_6$$^{3-/4-}$(aq) (**Fig. 4. 8b**). The discrepancy of the E_{fb}, N_D and lower V_{oc} values in Water compared to

$Fe(CN)_6{}^{3-/4-}$(aq) (**Table 4.1**) can be attributed to the trapping states related to Ta_3N_5 NTs–Water junction.

Table 4. 1 Comparison of PEC parameters and Mott-Schottky analyses of Ta_3N_5 NTs in Water and $Fe(CN)_6{}^{3-/4-}$(aq).

Analyses	Water			$Fe(CN)_6{}^{3-/4-}$(aq)		
V_{oc} (dark)/ V vs Ag/AgCl	0.01			0.10		
V_{oc} (1 Sun)/ V vs Ag/AgCl	–0.23			–0.36		
Frequency	E_{fb}/ V vs RHE	Slope	N_D*/ cm^{-3}	E_{fb}/ V vs RHE	Slope	N_D*/ cm^{-3}
200 Hz	0.20	4.4×10^{11}	7.7×10^{15}	–0.05	1.1×10^{11}	3.1×10^{16}
500 Hz	0.18	9.3×10^{11}	3.7×10^{15}	–0.05	1.8×10^{11}	1.9×10^{16}
1000 Hz	0.16	1.5×10^{12}	2.3×10^{15}	–0.05	2.8×10^{11}	1.2×10^{16}
1500 Hz	0.13	1.9×10^{12}	1.8×10^{15}	–0.05	3.6×10^{11}	9.4×10^{15}
3000 Hz	0.05	2.8×10^{12}	1.2×10^{15}	–0.06	5.3×10^{11}	6.4×10^{15}

*To measure the N_D from Mott-Schottky equation; the dielectric constant ε of equation 4.6 was taken as **8**, and the effective area of the nanotubes was estimated by the geometric roughness factor of the nanotubes considering that the NTs are perfectly smooth; however in actual it's not the case and the effective area of the electrode might be different.*

To elucidate the mechanism of charge transfer across the Ta_3N_5 NTs-Water interface as a function of applied potential, Nyquist plots were obtained in Water (**Fig. 4. 11**). It can be seen that increasing biasing potential has decreased the charge transfer resistance (R_{ct}) across the Ta_3N_5 NTs–Water interface (Inset of **Fig. 4. 11**). As discussed earlier, applying more positive potentials in Water, photocurrent was improved as well as the cathodic transient spikes were overcome (**Fig. 4. 8a** & **9c).** The Nyquist plots clearly indicate that low charge transfer resistance is obtained at higher applied potential and that can be one another reason to drive water oxidation at higher external potentials for pristine Ta_3N_5 NTs in Water. In addition, the poor fill factor of the LSV curves of **Fig. 4. 8a** can be further related to the R_{ct} values.
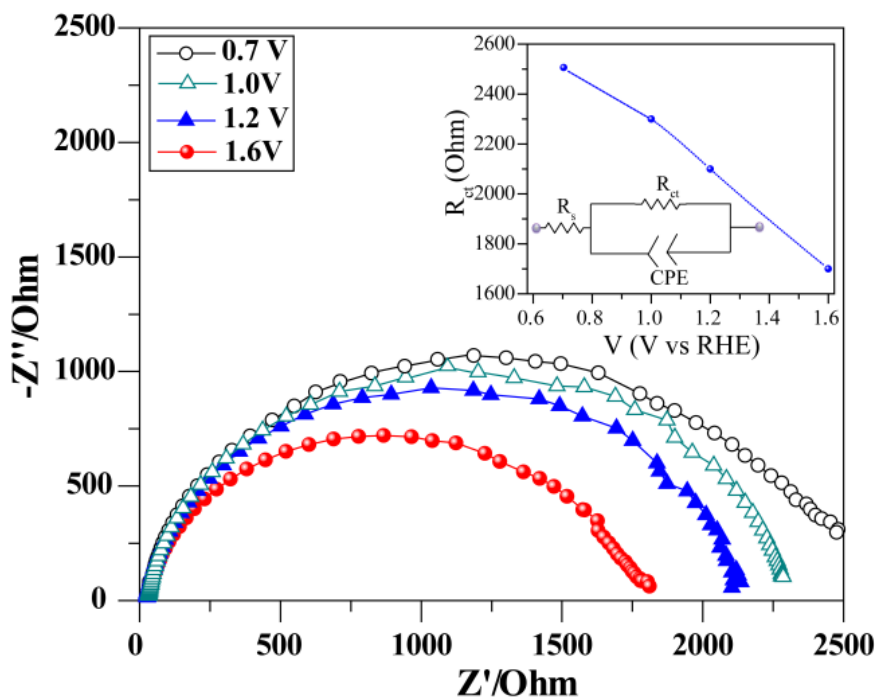
Fig.4. 11 Nyquist plots for pristineTa₃N₅ NTs in Water as a function of applied potentials.*

* Inset: The equivalent circuit and R_{ct} vs applied potential graphs extracted from circuit fitting.

For the analyses discussed above we have used Ta₃N₅ NTs synthesized for 20 min of anodization and nitrided at 800°C for 3 h. [13] To investigate if decreasing the length of the NTs influence the photocurrent to compensate for the hole trapping; length of the NTs is decreased by anodization of 5 min and further nitriding them at 800°C for 3 h. The LSV curve obtained for this sample in Water is shown in **Fig. 4. 12a** (red color solid line). Comparing the photocurrent with the longer length Ta₃N₅ NTs obtained at the same nitridation conditions (**Fig. 4. 8a**, highlighted potential window), no significant improvement can be observed. Therefore, short length NTs; that are expected to present lower resistance to the back contact thereby decreasing the recombination could not compete with the trapping states. To study if; higher temperature nitridation that decrease the oxygen content and improves the crystallinity; could cope with these trapping events to improve the photocurrent, we have obtained LSV curves of the sample anodized for 20 min and nitrided at 900°C for 3 h (**Fig. 4. 12a** - blue color line). The cathodic and anodic spikes can be observed clearly and the photocurrent is still not improved within water splitting potential window. However, a slight improvement was obtained at higher potentials > 1.23 V vs RHE. Therefore, the trapping states are independent of the length and the crystallinity of the NTs and application of large biasing for improved charge transfer is necessary. On the other hand, when these samples are tested in

[Fe(CN)$_6$]$^{3-/4-}$ (aq); compare to **Fig. 4. 8b** dramatic enhancement in the photocurrent can be observed.
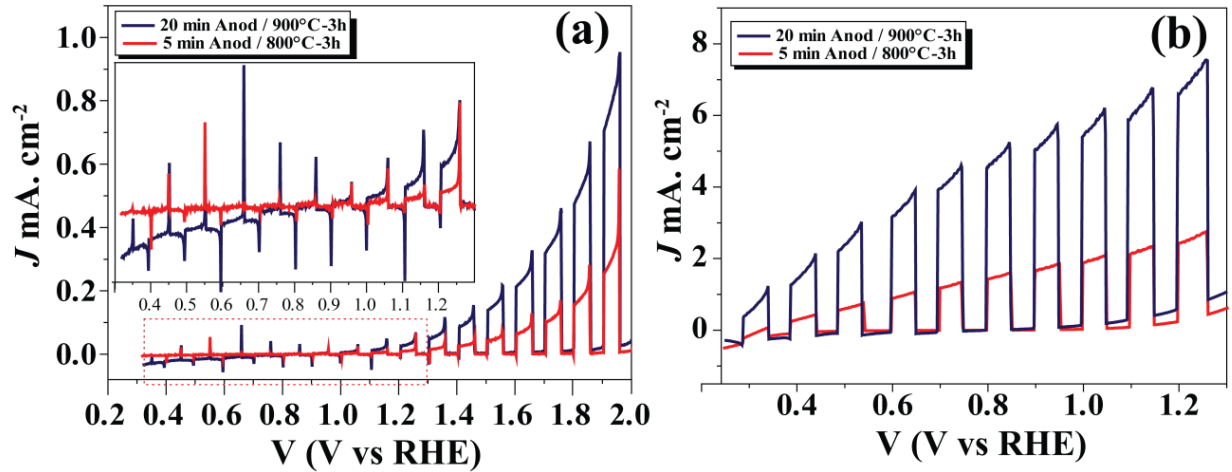
Fig.4. 12 LSV curves of pristineTa$_3$N$_5$ NTs in (a) Water and (b) Fe(CN)$_6^{3-/4-}$ (aq).

The photocurrent discrepancy for the same samples measured in two different electrolytes clearly indicates the critical role of the trapping states on the photogenerated carriers. Therefore, pristine Ta$_3$N$_5$ NTs are not suitable without the presence of efficient hole scavenging species in the electrolyte. Based on the **Table 4.1** and the CV analyses shown above; the band structure of pristine Ta$_3$N$_5$ NTs is constructed in **Fig. 4. 13** showing the energetics when holes are scavenged efficiently by Fe(CN)$_6^{3-/4-}$ (aq) and when they are trapped in Water.
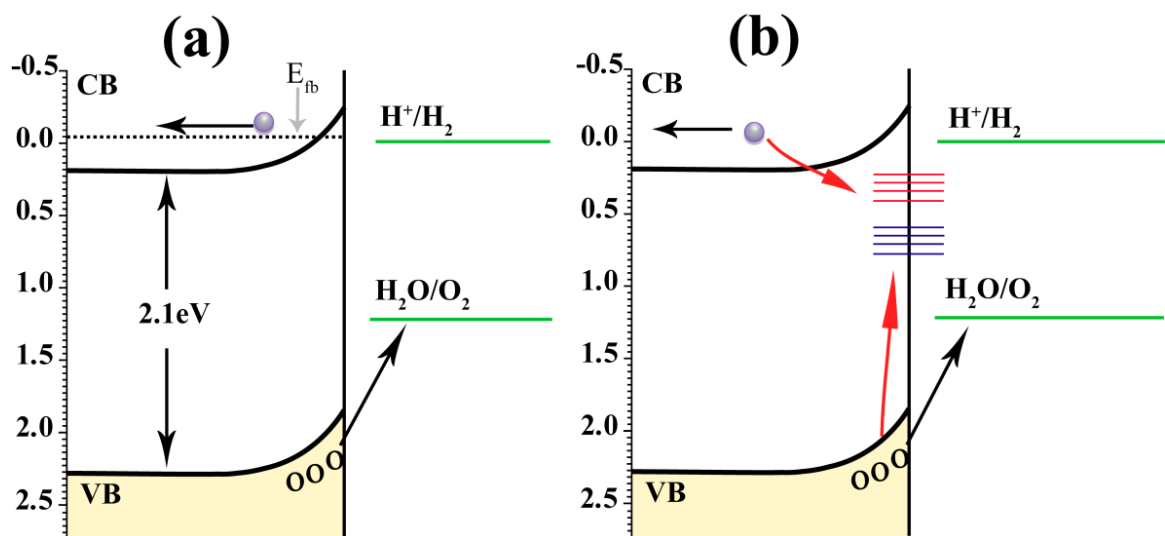
Fig.4. 13 Schematic representation of the energetics for pristine Ta$_3$N$_5$ NTs for (a) efficient hole scavenging in Fe(CN)$_6^{3-/4-}$ (aq) and (b) hole trapping in Water.

Now the question arises how to improve Ta_3N_5 NTs electrodes for PEC devices? One of the main circumventing approach is to incorporate suitable oxidizing co-catalysts, such as Co_3O_4, $Co(OH)_x$, IrO_2, Co-Pi etc.[9, 112, 111, 121 119] We suggest that for Ta_3N_5 NTs, the hole scavenger should be in the form of redox specie or a co-catalyst to avoid hole trapping. Therefore, avoiding the hole accumulation to accelerate the water oxidation kinetics are pivotal to improve PEC performance of the Ta_3N_5 NTs.

4.3. Partial conclusions

In summary, the insight to the PEC performance of pristine Ta_3N_5 NTs is provided by studying the semiconductor–electrolyte interface in Water and competitive sacrificial reagent. It was found that in Water the pristine photoanode presents large anodic and cathodic spikes upon light chopping; of that the later was more prominent at lower biasing potentials. On the other hand, the photocurrent was not only improved in the sacrificial agent but also the anodic and as well as the cathodic spikes were not observed demonstrating simple outer sphere valence band hole scavenging. By thorough investigations, it was confirmed that the PEC activity of pristine Ta_3N_5 NTs is highly dependent on the interfacial hole scavenging. We observed for the first time that pristine Ta_3N_5 NTs are highly affected by the trapping states related to Ta_3N_5 NTs–Water junction. It was observed that these trapping states are activated under light illumination and photogenerated holes are either recombine or trapped in these states and higher biasing potential is required to improve the photocurrent, albeit very little. It has been suggested that these trapping states are the Water intermediates with reduced tantalum species and/or the oxygen content in the tubular matrix. In the literature, for pristine Ta_3N_5 NTs higher external biasing (> 1.23V vs RHE) has been reported for improved water oxidation [14,17] and we found that the large onset potential required in Water for pristine Ta_3N_5 NTs is related to these trapping events. Furthermore, when the anodization and nitridation conditions were modified; the conditions of large applied biasing were still required; showing that the trapping states are intrinsic drawback of pristineTa_3N_5 NTs–Water junction. Therefore, for improved PEC activity at lower external biasing efficient hole scavenger or suitable water oxidation co-catalysts should be used. Thus, in addition to providing new insight into the water oxidation process for pristine Ta_3N_5 NTs photoanode, the investigation methodology presented in this work, will be of great utility in further studies on other semiconductor electrodes, aiming to understand their charge transportation and photocatalytic properties.

CHAPTER 5

EFFECT OF THERMAL NITRIDATION ON THE PROPERTIES OF Ta$_3$N$_5$ NANOTUBULAR PHOTOANODES

5.1. Objectives

In recent years, much more efforts have been devoted to the development of technologies to generate and store clean energy. The search for new materials is constantly growing and semiconductors have been the focus of intensive study.[9,139,140,50] Tantalum nitride (Ta$_3$N$_5$) has received an increasing attention for application in water splitting, mainly due to its near optimal band structure. [17,8] In addition, Ta$_3$N$_5$ nanotubes (NTs) have been found to present an enormous potential for applications in photoelectrochemical (PEC) devices.[12,11,14] To synthesize Ta$_3$N$_5$ that presents tubular morphology at high temperature nitridation; the precursor (Ta$_2$O$_5$ NTs) should be synthesized in conditions that result in thick walled nanotubes with increased adherence to the Ta substrate. For Ta$_3$N$_5$ presenting tubular morphology, a thorough investigations on lower and higher temperature nitridation at which pristine Ta$_3$N$_5$ with tubular morphology can be obtained and conditions at which it presents improved crystallinity are warranted.

Electrochemical impedance spectroscopy (EIS) is a powerful tool to study the semiconductor–electrolyte interface. The equivalent circuit (EC) analogy simplify the elucidation of electrochemical systems; provided the particular arrangement of circuit elements in a network possesses physical meaning.[41,141] Using EIS and EC to investigate the interfacial charge transportation of Ta$_3$N$_5$ NTs synthesized under different nitridation conditions are interesting to understand their PEC activity and to optimize them for improved performance.

In this part of the work, we study the effect of nitridation temperature and time on the morphology, crystalline structure, interfacial charge transfer, PEC activity and flat band potential of Ta$_3$N$_5$ NTs. Samples were obtained at nitridation temperature ranging from 650°C to 1000°C and nitridation times from 1 to 10 h. Three sets of samples have been synthesized: i) performing nitridation for 10 h at the temperatures of 650°C, 700°C, 750°C, 800°C and 900°C, ii) at constant nitridation temperature of 800°C during nitridation times of 1, 2, 3, 5 and 10 h and iii) performing nitridation for 3 h at the temperatures of 800°C, 850°C, 900°C and 1000°C. For simplicity, the samples will be denoted following the format ***T°C-time, e.g. the sample nitrided at 800°C for 1 hour is represented as 800°C-1h.***

5.2 Results and Discussion

5.2.1. Morphology

Fig. 5. 1 displays the SEM and TEM images of the samples synthesized by nitridation for 10 h at 650°C, 800°C and 900°C. One can observe an increase in roughness on the walls of the NTs with the temperature. However, upon thermal nitridation for 10 h at 900°C; a remarkable collapse in the tubular morphology is observed as the nanotubes are shrunk and turn into an urchin–like structure (**Fig. 5. 1c**). As most of the literature on Ta_3N_5 describes the synthesis at 800°C, we have obtained nanotubes at this temperature and varied the nitridation times for; 1, 2, 3, 5 and 10 h.[11,113]
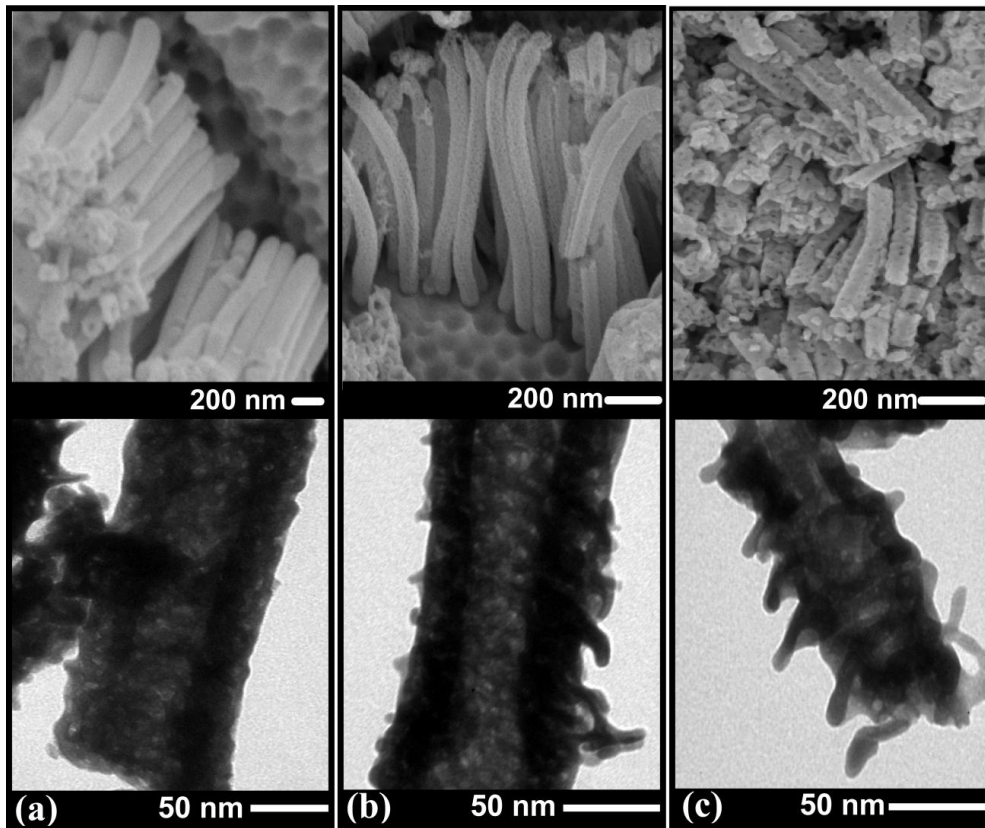
Fig.5. 1 SEM (Top) and TEM (Bottom) images of the samples prepared at (a) 650°C (b) 800°C and (c) 900°C for a time of 10h.

As tubular morphology is observed for 800°-10h; therefore, regardless the nitridation time all the samples maintained tubular morphology. **Fig. 5.2** compares the morphology of the samples prepared at 850°C, 900°C and 1000°C obtained for the nitridation time of 3 h. It can be seen that the tubular morphology is only sustained at the temperature as high as 900°C,

once at 1000°C the nanotubes collapsed and the walls are cracked. The nitridation temperatures and times have changed the geometrical dimensions of the Ta_3N_5 NTs compared to the anodized NTs (**Table 5.1**) that is related to the density difference between Ta_2O_5 and Ta_3N_5.[98]

Table 5. 1 Estimated geometrical dimensions of Ta_3N_5 nanotubes as a function of nitridation temperature and time.*

Sample	Wall thickness/nm *	Diameter/nm *	Length/µm †
As-Anodized	34	130	1.60
650°C-10h	34	128	1.58
700°C-10h	33	125	1.52
750°C-10h	32	110	1.40
800°C-2h	33	120	1.50
800°C-3h	30	100	1.40
800°C-5h	28	95	1.35
800°C-10h	28	90	1.20
850°C-3h	28	90	1.25
900°C-3h	25	75	1.10
900°C-10h	-	-	-
1000°C-3h	-	-	-

* Wall thicknesses and Diameters of the NTs were calculated from TEM images taken from different locations.

† Lengths of the NTs were calculated from SEM images.

The key to preserve the morphology of the Ta_3N_5 NTs for nitridation at higher temperatures lies in the low temperature anodization to prepare Ta_2O_5 NTs; resulting in strong adhesion to the Ta substrate and presenting thick walls.[80] The results show that for both conditions of long nitridation time of 10 h at 900°C (**Fig. 5. 1c**) and for short periods of 3 h at 1000°C (**Fig. 5. 2**) the nanotubes collapsed. Therefore, to preserve the tubular morphology low temperature anodization of the precursor is beneficial for sufficiently high nitridation temperature applied for short enough time. Hereafter, we will discuss the structural characterization for the samples that preserved tubular morphology; however, for comparison the PEC performances of all synthesized samples have been studied.
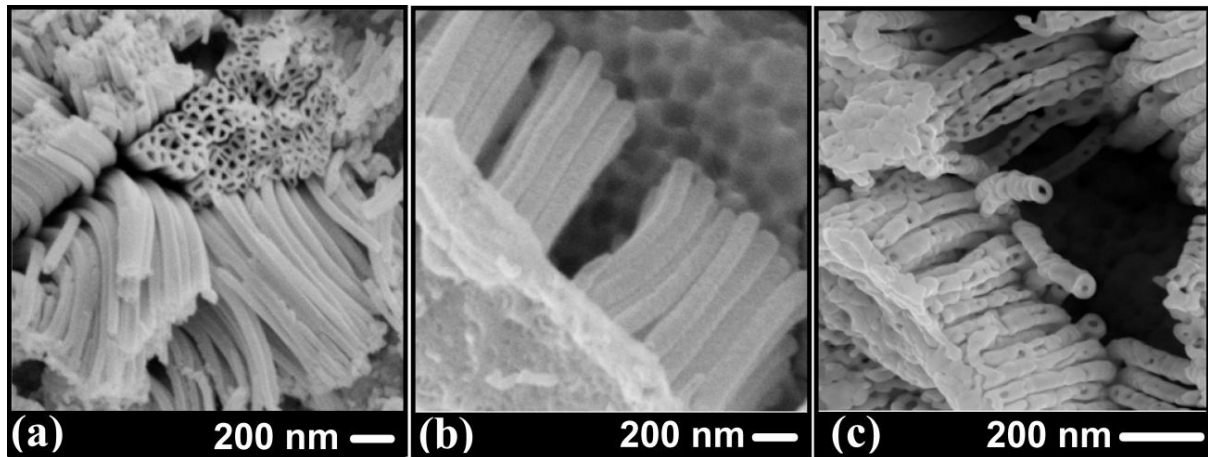
Fig.5. 2 SEM images of the samples prepared at (a) 850°C (b) 900°C and (c) 1000°C for a time of 3h.

5.2.2 Crystalline structure of Ta₃N₅ nanotubes

Studying the crystalline structure of Ta_3N_5 NTs adhere to the Ta substrate by XRD is a challenge task as the Ta foil presents plastic deformation. From the XRD patterns recorded by three different approaches; we have provided a comprehensive methodology to study this system (**Fig. 5.3**). For comparison, the XRD of the precursor Ta_2O_5 is displayed in **Fig. 5. 3a.** Only diffraction peaks characteristic of Ta can be observed as expected; as the as–anodized Ta_2O_5 NTs are amorphous.[80] After thermal nitridation the grey colored Ta_2O_5 NTs turns into red colored Ta_3N_5 NTs.[11] To investigate the Ta_3N_5 we firstly performed conventional XRD of the NTs adhere to the Ta substrate (**Fig. 5. 3b**). One can observe three different species in the samples; Ta_3N_5 (PDF# 79-1533), sub–nitride $TaN_{0.1}$ (PDF# 25-1278) and Ta (PDF# 4-788); their corresponding peaks are marked as *, Δ and Θ; respectively. In addition, the relative intensity of $TaN_{0.1}$ peaks increases with the temperature suggesting the increase in the concentration of sub–nitride phases at higher temperatures (**Fig. 5. 3b**).[110] The presence of sub–nitride phase has been earlier reported;[11] however, no information is available on the position or interface where it lies in the sample neither on how this phase is formed. The SEM images in **Fig. 5. 1 and 2** show that Ta_3N_5 NTs present a vertically oriented porous structure, allowing the NH_3 to diffuse from top to bottom to readily replace oxygen by nitrogen resulting in Ta_3N_5 NTs over the entire nanotube. It has been earlier observed that for the NTs of Ta_3N_5 the oxygen diffuses to the walls of the NTs and higher temperature nitridation decreases oxygen content. Furthermore, according to the literature, pristine tantalum metal cannot readily react under flowing ammonia to form any nitride of tantalum (*XRD patterns of pure Ta before and after nitridation under flowing ammonia for high temperatures were*

exactly the same).[131] Therefore, we suggest that the oxygen content that diffuses to the bottom Ta substrate reacts with the Ta atoms forming non–stoichiometric oxides which then react with the NH_3 to transform into $TaN_{0.1}$.
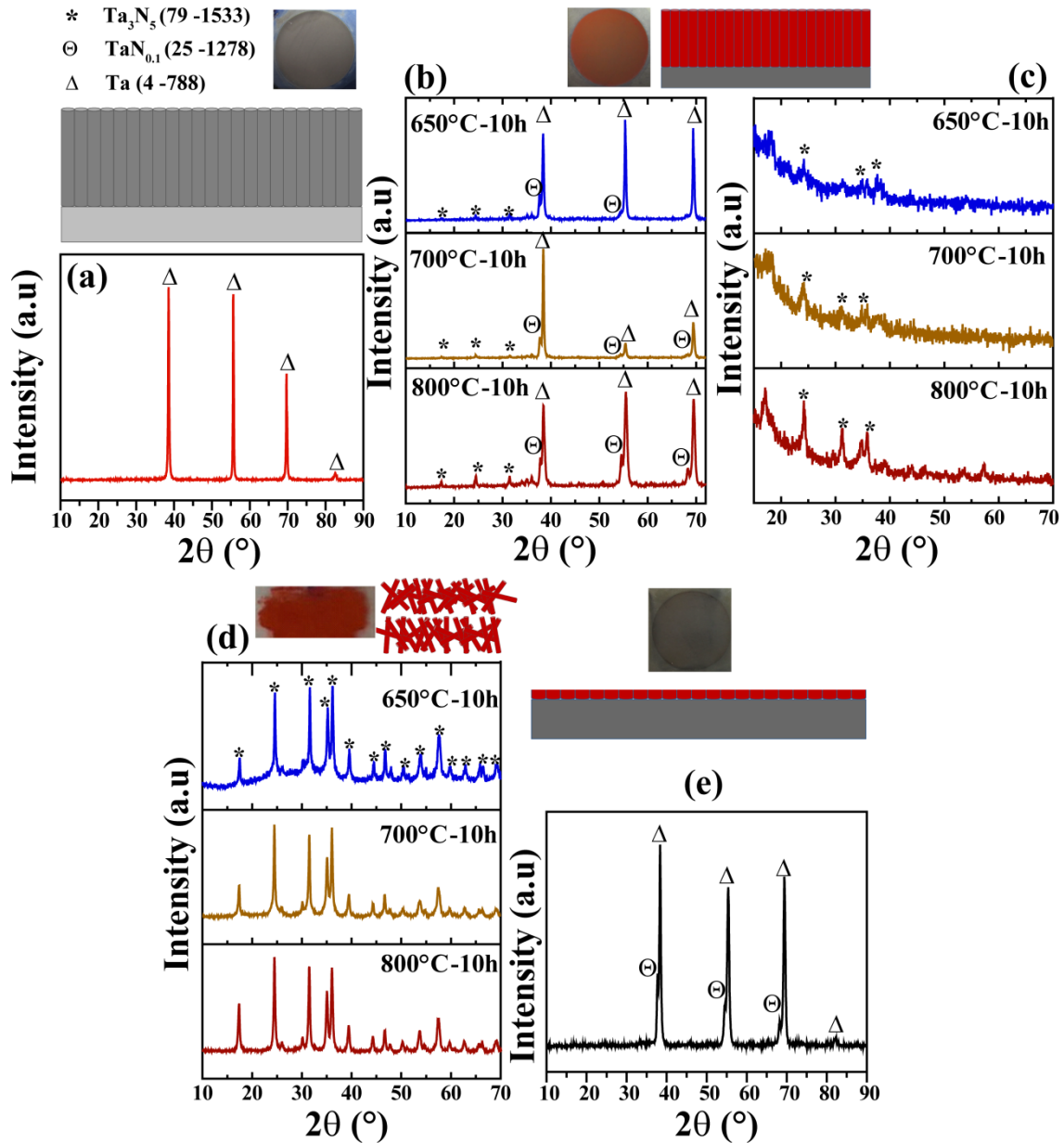
Fig.5. 3 XRD patterns of (a) as-anodized Ta_2O_5 NTs/Ta, (b) and (c) Ta_3N_5 NTs/Ta, (d) Ta_3N_5 NTs removed from the substrate and (e) the substrate of which the Ta_3N_5 NTs are scratched off.

The Ta and $TaN_{0.1}$ peaks have higher relative intensity compared to Ta_3N_5 phase; therefore, a complete characteristic diffractograms for the whole 2θ range of Ta_3N_5 could not be observed, instead; Ta_3N_5 peaks are visible up to $2\theta \sim 36°$. In order to remove the substrate contribution, we have obtained the grazing angle XRD diffractograms of the nanotubes at a very small

grazing angle of 0.3° (**Fig. 5.3c**). The substrate contributions are almost completely removed and the subnitride $TaN_{0.1}$ (present in conventional XRD) is absent in the grazing angle XRD, showing that $TaN_{0.1}$ is in fact a substrate contribution. In addition, for 650°C-10h the Ta_3N_5 peaks visible in **Fig. 5. 3b** are nearly absent in **Fig. 5. 3c** that shows the presence of Ta_3N_5 crystalline grains in amorphous Ta_2O_5 tubular matrix. Grazing angle XRD helped to minimize the contribution from the Ta substrate, however; at the same instant the signal resolution from Ta_3N_5 NTs have been lost. Hence, the NTs were removed from the Ta substrate and powder XRD diffractograms have been obtained for the scratched off NTs (**Fig. 5. 3d**). The signal resolution is highly improved and all of the observed peaks correspond to Ta_3N_5. Finally, XRD patterns obtained from the substrate of which the NTs were removed have shown just the $TaN_{0.1}$ and Ta characteristic peaks (**Fig. 5. 3e**) strongly confirming the presence of $TaN_{0.1}$ at the substrate. Nevertheless, we found that $TaN_{0.1}$ is metallic; however, we suggest developing a certain strategy that can help to avoid these phases to synthesize Ta_3N_5 NTs for PEC applications. With the aim to study pristine Ta_3N_5 NTs free from any other contribution from now onward we will discuss the XRD patterns obtained from the scratched off powders.

To investigate the minimum nitridation conditions to obtain Ta_3N_5 NTs we started thermal nitridation at 650 °C for 1 h and 3 h. However, at these conditions the presence of a mixed structure of Ta_2O_5 (PDF# 25-922) and Ta_3N_5 (PDF# 79-1533) was observed and by increasing the nitridation time from 3h to 6h at 650°C (**Fig. 5.4**), clear changes in the XRD patterns are observed once pristine Ta_3N_5 phase is obtained at these conditions.

Nevertheless, for 650°C-6h one can observe a huge background in the spectrum along with wide diffraction patterns presenting amorphism in the sample. Therefore, to further improve the crystallinity, we have increased the nitridation time to 10 h at 650°C (**Fig. 5. 3c**). The diffraction peaks are sharper when compared to 650°C-6 h; therefore, we fixed the nitridation time for 10 h and varied the temperatures to 700°C, 750°C, 800°C and 900°C. Furthermore, impurities were observed for 800°C-1h (**Fig. 5.4**); and by increasing the time to 2 h at 800°C pristine Ta_3N_5 NTs are obtained.
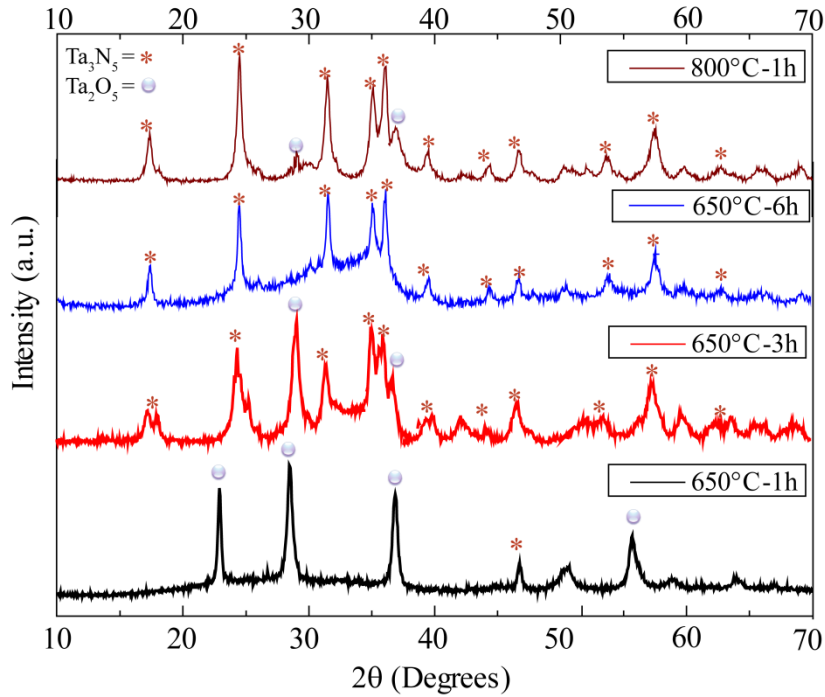
Fig.5. 4 XRD patterns of the samples prepared at 650°C and 800°C

Fig. 5.5 displays the XRD patterns of phase-pure orthorhombic Ta_3N_5 NTs; corresponding to the PDF# 79-1533. Interestingly, when compared to commercial Ta_2O_5 powders which are crystalline in nature, the transformation from Ta_2O_5 NTs to Ta_3N_5 NTs is found to take place at a lower temperature of 650°C.[98] We may suggest that amorphous nanotubular precursors of Ta_2O_5 are easy to transform to Ta_3N_5 at low temperature.
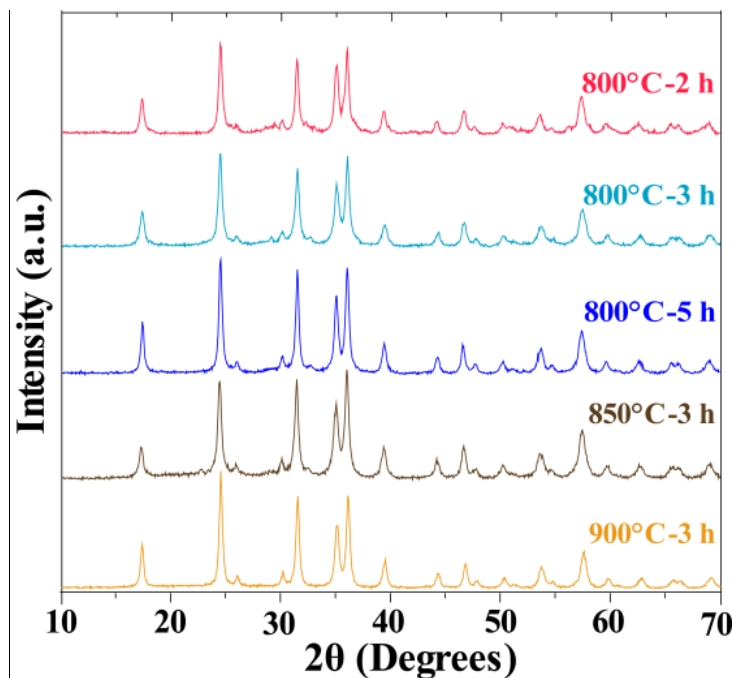
Fig.5. 5 XRD patterns of Ta_3N_5 NTs prepared by thermal nitridation.

Crystalline structures were refined by the Rietveld technique. Simulated patterns (**Fig. 5.6**) and the respective parameters are shown in **Table 5.2** and **Table 5.3.** For the set of samples prepared for 10 h, in addition to slight increase in the grain size the strain is increased with the temperature (**Table 5.3**).
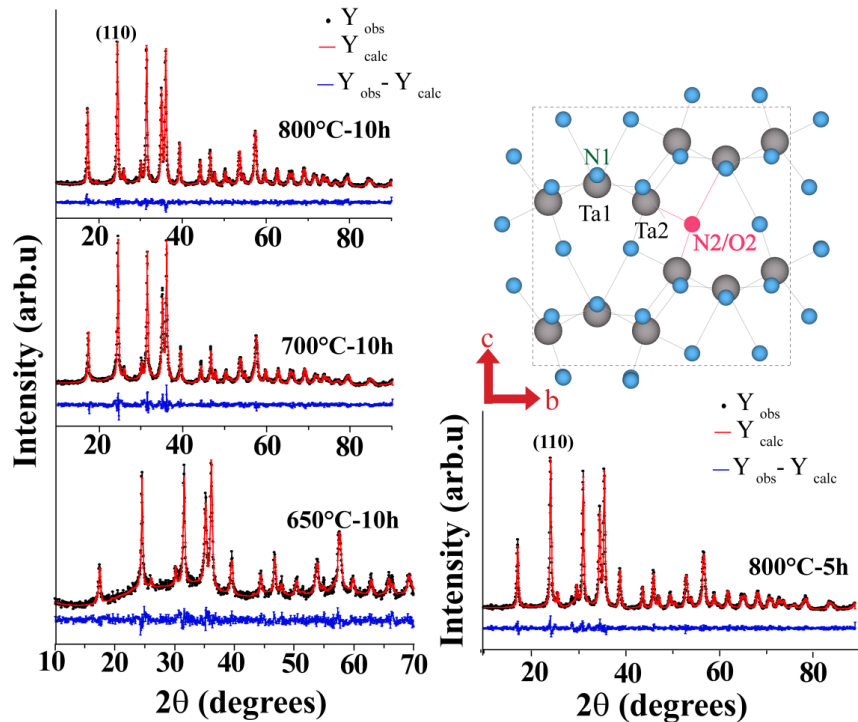
Fig.5. 6 Rietveld refinement profile for Ta_3N_5 NTs; (•) observed Y_{obs}, (red solid lines) calculated Y_{calc}, (blue solid lines) Y_{obs}–Y_{calc} difference of phase.

The increase in the strain might be related to the morphology preservation and increasing the roughness on the walls of the NTs. The larger crystalline grains and improved crystallinity were obtained from the 900°C-3h Ta_3N_5 NTs. Unlike earlier report on Ta_3N_5 thin films, the grain size for Ta_3N_5 NTs found here presents a dependence on the nitridation conditions.[94] This behavior can be rationalized on the basis of different crystal growth phenomena for thin films and tubular morphology. Once thin films are compact and during the crystal growth; the grains exhibit stress from their neighbor grains that may limit their further growth due to the compact nature of thin films. Therefore, within the limit of stability of Ta_3N_5 phase the grains become independent of the nitridation temperature.[94]

Table 5. 2 Percentages of vacancies (vac), occupancies (occ), substitutions (sub) in the Wyckoff positions, cell parameters and agreement factors deduced from the Rietveld refinements.

Sample	Ta1 (4c)	Ta2 (8f)	N1 (4c)	N2/**O2** (8f)	N3 (8f)	R_{bragg^-} factor	R_{f^-} factor	Chi^2	*a* *b* *c*
650°C-10h	97.98 occ 2.02 vac	99.89 occ 0.11 vac	71.33 occ 28.67 vac	0 – occ **100 subs**	99.98 occ 0.02 vac	6.19	4.06	1.43	3.88516 10.16713 10.24118
700°C-10h	94.60 occ 5.40 vac	99.97occ 0.03 vac	69.71 occ 30.29 vac	37.10 occ **62.90 sub**	100 occ 0 – vac	3.33	1.94	1.99	3.89520 10.19483 10.26891
800°C-3h	93.25 occ 6.744 vac	99.15 occ 0.846 vac	95.32 occ 4.68 vac	49.73 occ **50.27 sub**	100 occ 0- vac	2.72	1.61	1.63	3.89551 10.21312 10.27800
800°C-5h	93.87 occ 6.128 vac	98.32 occ 1.68 vac	94.40 occ 5.60 vac	66.01 occ **33.99 sub**	100 occ 0 – vac	2.70	1.45	1.51	3.89962 10.20950 10.27345
800°C-10h	94.58 occ 5.42 vac	98.39 occ 1.61 vac	95.03 occ 4.97 vac	80.01 occ **19.99 sub**	100 occ 0 – vac	4.14	2.41	1.37	3.89325 10.20868 10.26509
850°C-3h	99.14 occ 0.852 vac	99.65 occ 0.35 vac	86.00 occ 14.00 vac	71.18 occ **28.82 sub**	100 occ 0- vac	3.78	2.27	2.36	3.89547 10.21895 10.28788
900°C-3h	99.68 occ 0. 32 vac	100 occ 0- vac	89.83 occ 10.17 vac	86.81 occ **13.19 sub**	100 occ 0 – vac	2.31	1.53	1.35	3.88879 10.21532 10.26565

On the other hand, NTs are isolated from their surrounding exhibiting lower stress from the neighboring grains during the growth; thereby, high temperature nitridation facilitates to increase their size. However, care must be taken for tubular morphology as the morphology can be collapsed under very harsh nitridation conditions. The percentages of defects in the crystalline structure of Ta_3N_5 NTs are calculated considering the occupation factors obtained by Rietveld refinement (**Table 5.2**). At the Wyckoff sites Ta1(4c), Ta2(8f) and N1(8f) Schottky defects were found. Following the methodology proposed by Henderson et al,[95] the refinements were improved when oxygen substitutional defects are incorporated at the 3-coordinated Wyckoff site N2(4f). These results confirm that oxygen in the crystalline structure of Ta_3N_5 cannot be completely removed by thermal nitridation.[95,142] Based on the refinements, nominal stoichiometries of the samples were calculated from the percentages of site occupancy and vacancy (**Table 5.2**) obtained from the occupation factors; and are displayed in **Table 5.3**.

Table 5. 3 Grain size, lattice strain and nominal stoichiometry obtained by the refinements.

Sample	Av. Grain Size (nm)	Strain($\times 10^{-4}$)	Stoichiometry
650°C-10h	29.59	12.15	$Ta_{2.97}N_{2.71}O_{2.0}$
700°C-10h	32.56	19.93	$Ta_{2.94}N_{3.43}O_{1.25}$
800°C-3h	19.71	13.85	$Ta_{2.89}N_{4.18}O_{0.84}$
800°C-5h	31.53	18.67	$Ta_{2.90}N_{4.26}O_{0.67}$
800°C-10h	37.46	22.00	$Ta_{2.91}N_{4.55}O_{0.39}$
850°C-3h	34.03	32.43	$Ta_{2.98}N_{4.29}O_{0.48}$
900°C-3h	43.51	36.90	$Ta_{2.99}N_{4.61}O_{0.22}$

In the set of samples prepared for the nitridation of 10 h, one can observe a decrease in oxygen content by increasing the temperature. However, for 650°C-10h the Ta stoichiometry is "2.97" i.e greater than the other samples but oxygen content are highest; suggesting the presence of large oxide content in the sample. Therefore, we may suggest; for sample 650°C-10h, the Ta_3N_5 crystalline grains are distributed in the amorphous tubular matrix of Ta_2O_5. In addition, the stoichiometry was not ideal even for 800°C-10h. These results strongly suggest that indeed nitridation temperature of 800°C is not an optimum condition for the synthesis of Ta_3N_5.[11,113] Therefore, the temperature should be increased; however care must be taken to choose an appropriate nitridation time, in order to preserve the tubular morphology. Further details on the crystalline structure of the nanotublar samples prepared for 3 h of nitridation as a function of nitridation temperature are discussed elsewhere (See Appendix 1).

5.2.3 Optical characterization

After nitridation a red color was visually observed for the samples indicating the formation of Ta_3N_5 NTs.[56,67] **Fig. 5. 7** displays the UV–Vis diffuse reflectance spectra of Ta_2O_5 and some selected samples of Ta_3N_5 NTs. The absorption edges of the Ta_3N_5 have been red shifted from the Ta_2O_5 edge due to narrowing of the band gap.
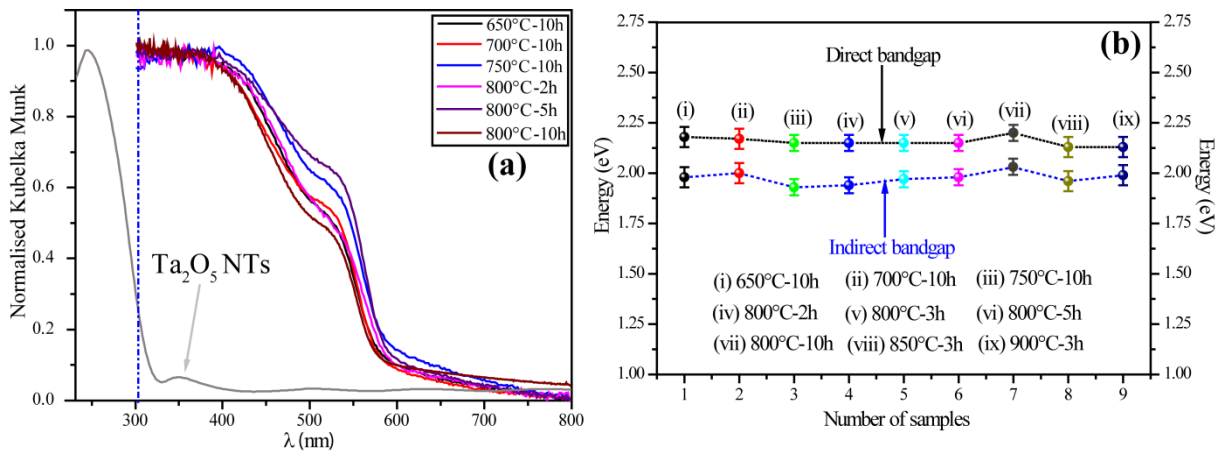
Fig.5. 7 Absorption spectra (a). Direct bandgap obtained from $[K.M (R)h\nu]^2$ vs hν and Indirect bandgap obtained from $[K.M (R)h\nu]^{0.5}$ vs hν for Ta_3N_5 NTs (b).

The direct and indirect band gaps were obtained by extrapolating the linear region on the UV-Vis spectra and were found to ca. 2.1–2.2 and 1.93–1.98 eV, respectively consistent with the reported values for Ta_3N_5.[11,98]

5.3.4 Electrochemical impedance spectroscopy (EIS)

To investigate the effect of nitridation conditions on the charge transfer across the Ta_3N_5 NTs–electrolyte interface, we have performed EIS (**Fig. 5. 8**). For the set of samples prepared for the nitridation time of 10 h (**Fig. 5. 8a**); incomplete semicircles can be observed which are characteristic of capacitance systems exhibiting non ideal behavior. As observed in the TEM images displayed in **Fig. 5.1 (bottom),** nitridation for longer time at high temperatures results in a rougher structure; that can affect the charge transportation at the interface. From the single semicircles (one time constant) shown in **Fig.5. 8a** EIS data was fitted to an equivalent circuit (**Fig. 5. 8d**); consisting of a series resistance R_s and single CPE (constant phase element) parallel with charge transfer R_{ct}. The CPE in an electrochemical system may arise from: (a) distribution of the relaxation times due to non-homogeneities existing at the electrode– electrolyte interface, (b) porosity of the electrode, (c) the nature of the electrode and (d) dynamic disorder associated with diffusion.[143,144,145] The impedance of CPE can be calculated by the following relationship;

$$1/Z(\omega) = Q (j\omega)^n$$

Where Q is the pre-factor of CPE and n is the exponential term. For pure capacitor its value is 1 whereas for pure resistor it is 0. Based on the nanotubular nature and structural non-

homogeneities (SEM and Rietveld refinements) adding CPE for the Ta_3N_5 NTs–electrolyte interface is physically true. By fitting the Nyquist plots into the proposed equivalent circuit the values of the components have been found and to better visualize the R_{ct} as a function of various nitridation temperatures and times; we have plotted R_{ct} against different thermal treatments shown in the inset of Nyquist plots in **Fig. 5. 8**.
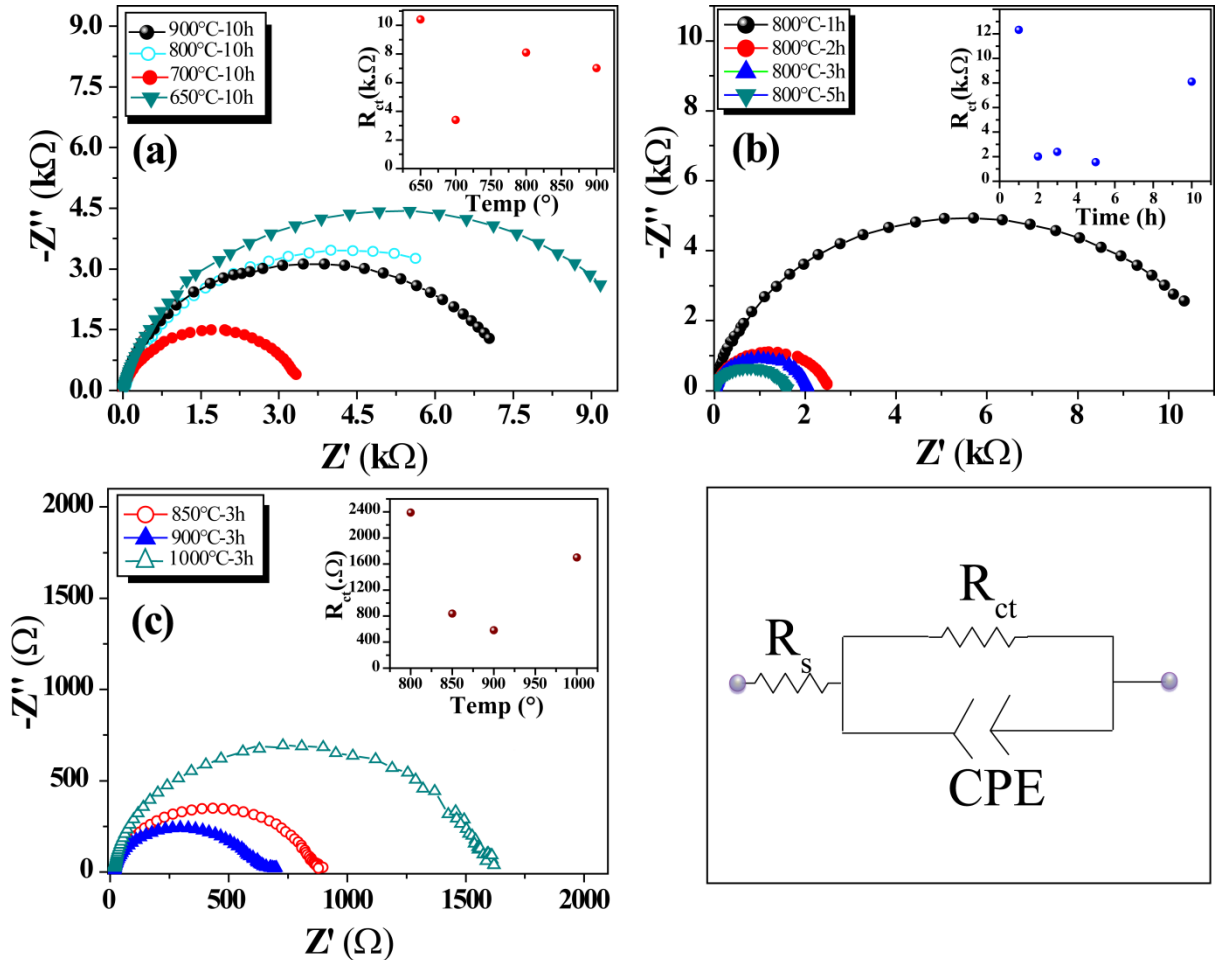
Fig.5. 8 Nyquist plots obtained under dark for Ta_3N_5 NTs prepared at different nitridation conditions.

The 650°C-10h sample presents the highest R_{ct} (**Fig. 8a**). In the XRD patterns of the sample some amorphism was observed (**Fig. 5. 3d**) and as observed in the Rietveld refinements (**Table 5.3**), the sample consists of highest oxygen content. Therefore, it is reasonable to propose that the amorphism and the highest oxygen content in the sample are the main reasons for the highest R_{ct}. Interestingly, 700°C-10h has exhibited the lowest R_{ct}. The stoichiometry of both 650°C-10h and 700°C-10h samples (**Table 5.3)** show the presence of oxygen content and 700°C-10h is more crystalline than 650°C-10h and present a smaller R_{ct}.

Also 800°C-10h presents slightly higher R_{ct} compared to 900°C-10h, that might be related to smaller concentration of defects as can be inferred from the stoichiometry of $Ta_{2.99}N_{4.61}O_{0.22}$ obtained for sample prepared at 3h of nitridation time at 900° i.e 900°C-3h (**Table 5.3**). Now evaluating the samples prepared at fixed temperature of 800°C and varying nitridation times (**Fig. 5. 8b**); 800°C-1h (consisting of mixed phases of Ta_3N_5 and Ta_2O_5 as shown in **Fig. 5. 4**) present the highest R_{ct} while 800°C-5h presents the smallest R_{ct}. Lastly, for the set of 3h samples (**Fig. 5. 8c**), 900°C-3h evidently indicates the lowest interfacial charge transfer resistance compared to all of the samples synthesized in the current work corroborating the high crystallinity and phase purity as discussed earlier (**Table 5.3**). These results strongly suggest that nitridation conditions alter the crystalline structure of Ta_3N_5 NTs that further affects the interfacial charge transportation properties that are the functions of morphology, crystallinity and phase purity of Ta_3N_5 NTs photoanodes and for the lowest R_{ct} an optimum is exhibited for 900°C-3h.

The flat band potential of the semiconductor is one of the most important parameters for evaluating photoelectrochemical water splitting that helps to predict whether semiconductor should be biased externally or not. One of the most widely used technique to estimate the flat band of a semiconductor is the Mott-Shottky plot.[133] **Fig. 5. 9** displays the Mott-Shottky plots of the Ta_3N_5 NTs that present n-type transition from the positive slopes of the curves. On each graph the flat band potential (E_{fb}) is obtained by extrapolating the linear region which is presented as blue line intercepts. A very interesting result is that all of the samples present almost the same flat band potential of ca. –0.05 vs RHE; therefore, for Ta_3N_5 NTs, the E_{fb} is almost independent of nitridation temperature. In addition, samples 650°C-10h and 700°C-10h present a lower transition along with the main transition (highlighted in **Fig. 5. 9**); that can be related to the presence of oxide content that are higher in 650°-10h than in 700°-10h.
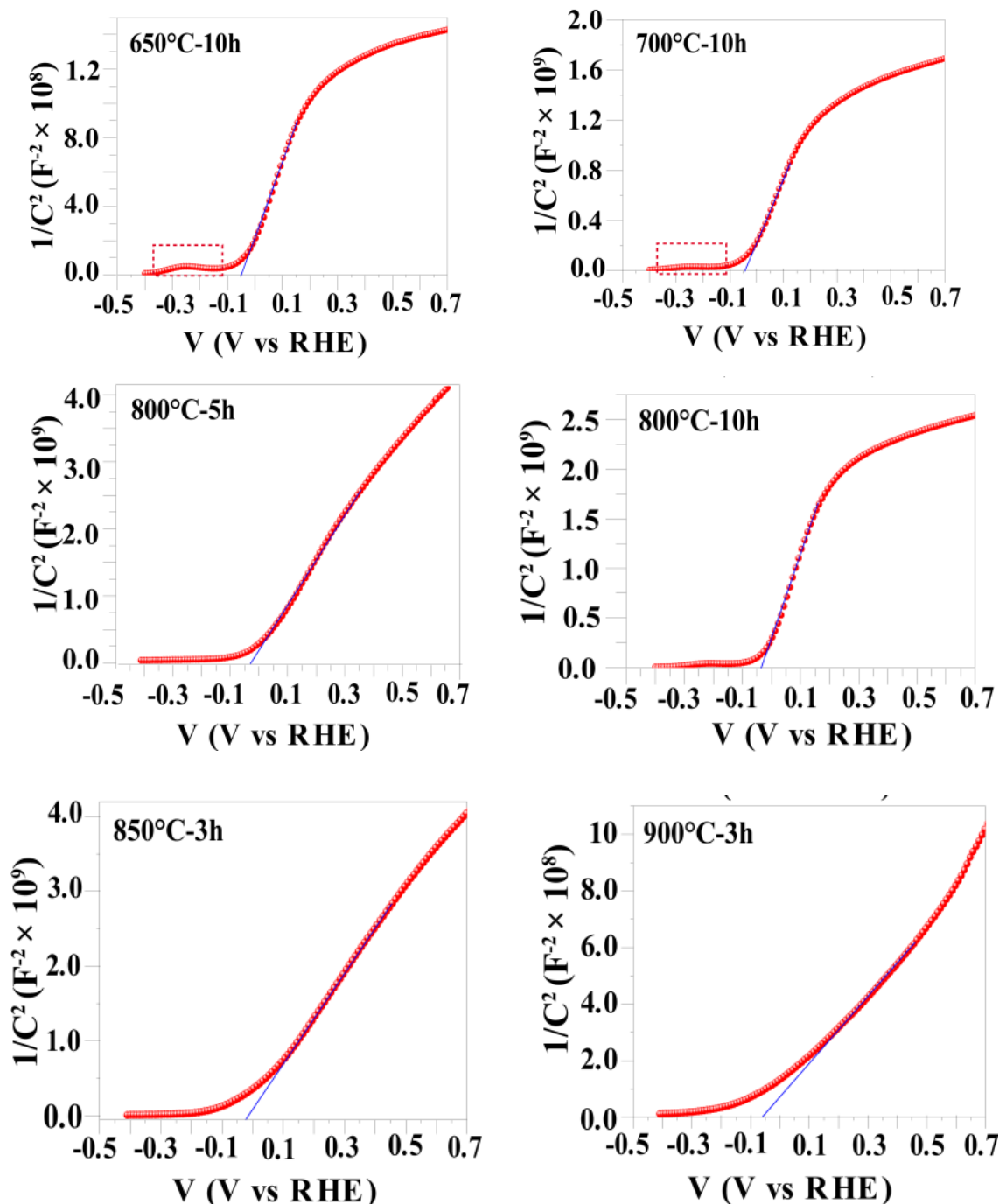
Fig.5. 9 Mott-Schottky plots of Ta_3N_5 NTs synthesized at various nitridation conditions.

5.3.5 PEC activity of Ta_3N_5 NTs

Fig. 5. 10 shows the linear sweep voltammetry (LSV) curves of all samples. Among the set of samples prepared for 10 h of nitridation, 650°C-10h has presented lowest PEC activity that can be related to lower order crystallinity (**Fig. 5. 3c**) as well as highest interfacial R_{ct} (**Fig. 5. 8a**). On the other hand the highest photocurrent was obtained from 900°C-10h. For the set of samples prepared at fixed temperature of 800°C by varying nitridation time; the sample

800°C-1h has shown poor PEC performance. The XRD analysis presents the mixture of Ta_2O_5 and Ta_3N_5 phases for 800°C-1h (**Fig. 5.4**). The trade-off between the sample chemical composition and the electrolyte clearly affects the PEC performance. Therefore, the impure phase and low crystallinity are the main reasons behind the poor performance of 800°C-1h. Interestingly 800°C-5h presented the higher PEC activity even compared to 800°C-10h. This result can be related to the thermal decomposition of the Ta_3N_5 at longer nitridation periods.[146] Although 800°C-5h present the higher photocurrent compared to other samples of the set; however, the photocurrent is still low, that can be rationalized in terms of the stoichiometries of the samples prepared at 800°C for varying nitridation times i.e, far away from the ideal Ta_3N_5. Therefore, 800°C is not a good choice to synthesize Ta_3N_5 NTs.
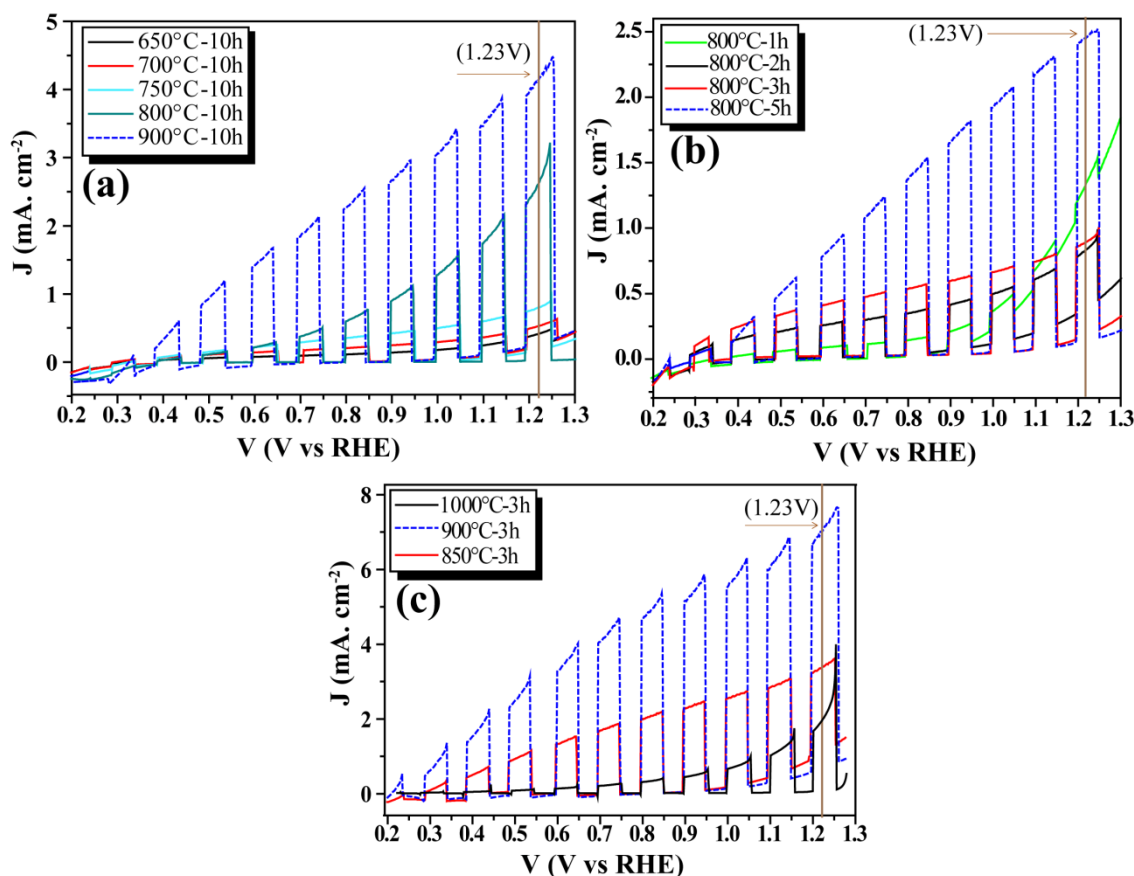
Fig.5. 10 LSV curves of Ta_3N_5 NTs obtained by chopping AM 1.5 (1 Sun) illumination.

Considering now the nitridation of the samples for fixed time of 3h under varying temperatures; clearly the 900°C-3h, presented improved photocurrent compared to all other samples prepared in the current work and the one shown in the earlier reports.[113,112] In addition, it has presented nearly a 2–3 fold photocurrent compared to 900°C-10h and 1000°C-3h. Therefore, the improved photocurrent from Ta_3N_5 nanotubular photoanodes is in fact a

synergistic combination of the tubular morphology, the controlled chemical composition and the improved charge transfer across the interface. **Table 5.4** contrasts the parameters obtained during the LSV experiments for Ta_3N_5 NTs photoanodes synthesized in the current study. To obtain the photocurrent, the dark current is subtracted from the current obtained under illumination.

Table 5. 4 (Photo)electrochemical parameters of Ta_3N_5 NTs obtained under various conditions of temperatures and nitridation times.

Sample	V_{oc}(dark)V vs Ag/AgCl	V_{oc} (AM 1.5) V vs Ag/AgCl	I_{ph} (0.64V vs RHE) 0 V vs Ag/AgCl	I_{ph} (1.23V vs RHE) 0.6 V vs Ag/AgCl
650°C-10h	0.10	–0.32	70 µA	180 µA
700°C-10h	0.10	–0.32	151 µA	328 µA
750°C-10h	0.11	–0.36	251 µA	710 µA
800°C-01h	0.08	–0.26	107 µA	98 µA
800°C-02h	0.10	–0.34	251 µA	556 µA
800°C-03h	0.10	–0.36	430 µA	900 µA
800°C-05h	0.10	–0.36	940 µA	2.6 mA
800°C-10h	0.11	–0.33	280 µA	2.4 mA
850°C-03h	0.10	–0.32	1.5 mA	3.2 mA
900°C-03h	0.10	–0.34	4 mA	7.4 mA
900°C-10h	0.11	–0.35	1.8 mA	3.9 mA
1000°C-3h	0.10	–0.34	600 µA	2.8 mA

The V_{oc} values are almost independent of the nitridation conditions for pristine Ta_3N_5 NTs photoanodes that might be related to the same flat band position obtained for pristine Ta_3N_5 NTs, however, 800°C-1h presented a slightly different V_{oc} under dark related to the presence of impurities in the sample.

5.3. Partial Conclusions

In summary, we have performed a thorough study on the effect of nitridation temperature and time on the syntheses of Ta_3N_5 NTs by thermal nitridation of the anodized precursor Ta_2O_5 NTs. We observed that amorphous Ta_2O_5 NTs are easier to transform to Ta_3N_5 by nitridation at low temperatures; however the samples obtained at lower temperatures present low crystallinity and poor photoelectrochemical performance. To synthesize Ta_3N_5 NTs by thermal nitridation; the temperature should be high enough to obtain higher crystallinity and time should be short enough to preserve the tubular morphology. The combined effect of high

crystallinity, tubular morphology and low charge transfer resistance across Ta_3N_5 NTs-electrolyte interface presents an optimized nitridation condition. Based on Rietveld refinement, EIS and LSV curves the sample 900°C-3h presents optimum features of a promising photoelectrode prepared in the current study.

CHAPTER 6

GENERAL CONCLUSIONS AND FUTURE PERSPECTIVES

In summary, we have successfully synthesized Ta_3N_5 thin films and nanotubes by thermal nitridation starting from Ta_2O_5 materials. Firstly, thin films were characterized to understand their optical and photoelectrochemical (PEC) properties comprehensively (**See Appendix 1 also**); and later the study was focused on optimizing Ta_3N_5 nanotubes to enhance their PEC performance.

Ta_3N_5 thin films have presented monoclinic phase. It was found that thermal nitridation results into nitrogen and tantalum Schottky defects and substitutional oxygen in 3-coordinated N atoms. The surface of the monoclinic Ta_3N_5 thin films presented different chemical composition compared to the underlying film. Real ε_1 and imaginary ε_2 parts of dielectric functions of the film were analyzed by the spectroscopic ellipsometry (SE) within a broad spectral range of 0.54–4.6 eV. The optical parameterization of SE data was carried out utilizing the Tauc-Lorentz and Lorentz oscillators. Concerning the application of the semiconductor in PEC water splitting, the dielectric constant ε_1 of Ta_3N_5 film in the visible spectral region (3.1–1.7 eV) was found within the range of 7–9; matching the theoretically reported value. The PEC analyses revealed that the band structure of Ta_3N_5 is strongly influenced by the pH of the employed electrolyte. Enhanced PEC activity was observed in alkaline condition that is attributed to the shorter depletion region width and the lower recombination life time.

After the investigations on Ta_3N_5 thin films we have provided the insight to the photoelectrochemical (PEC) performance of pristine Ta_3N_5 NTs by studying the semiconductor–electrolyte interface in Water and competitive sacrificial reagent. It was found that in Water the pristine photoanode presents large anodic and cathodic spikes upon light chopping; of that the later was more prominent at lower biasing potentials. On the other hand, the photocurrent was not only improved in the sacrificial agent but also the anodic and as well as the cathodic spikes were not observed demonstrating simple outer sphere valence band hole scavenging. By thorough investigations, it was confirmed that the PEC activity of pristine Ta_3N_5 NTs is highly dependent on the interfacial hole scavenging. We observed for the first time that pristine Ta_3N_5 NTs are highly affected by the trapping states related to Ta_3N_5 NTs–Water junction. It was observed that these trapping states are activated under light illumination and photogenerated holes are either recombine or trapped in the these states and higher biasing potential is required to improve the photocurrent, albeit very little. It has been

suggested that these trapping states are the Water intermediates with reduced tantalum species and/or the oxygen content in the tubular matrix. In the literature, for pristine Ta_3N_5 NTs higher external biasing (> 1.23V vs RHE) has been reported for improved water oxidation [14,17] and we found that the large onset potential required in Water for pristine Ta_3N_5 NTs is related to these trapping events. Furthermore, when the anodization and nitridation conditions were modified; the conditions of large applied biasing were still required; showing that the trapping states are intrinsic drawback of pristineTa_3N_5 NTs–Water junction. Therefore, for improved PEC activity at lower external biasing efficient hole scavenger or suitable water oxidation co-catalysts should be used. Thus, in addition to providing new insight into the water oxidation process for Ta_3N_5 NTs photoanode, the investigation methodology presented in this work, will be of great utility in further studies on other semiconductor electrodes, aiming to understand their charge transportation and photocatalytic properties.

As we found that Ta_3N_5 NTs when used without sacrificial reagent have poisoned by the trapping states related to the Ta_3N_5 NTs–Water junction; therefore we used sacrificial reagent to study the effect of nitridation on the properties of Ta_3N_5 NTs. A thorough study on the effect of nitridation temperature and time on the syntheses of Ta_3N_5 NTs by thermal nitridation of the anodized precursor Ta_2O_5 NTs have been provided. We observed that amorphous Ta_2O_5 NTs are easier to transform to Ta_3N_5 by nitridation at low temperatures; however the samples obtained at lower temperatures present low crystallinity and poor photoelectrochemical performance. To synthesize Ta_3N_5 NTs by thermal nitridation; the temperature should be high enough to obtain higher crystallinity and time should be short enough to preserve the tubular morphology. The combined effect of high crystallinity, tubular morphology and low charge transfer resistance across Ta_3N_5 NTs-electrolyte interface presents an optimized nitridation condition. Based on Rietveld refinement, EIS and LSV curves the sample 900°C-3h presents optimum features of a promising photoelectrode prepared in the current study.

From the effect of nitridation temperature and time on the syntheses of Ta_3N_5 NTs for PEC activities we found that higher nitridation temperatures for the shorter time as beneficial to improve the structural and PEC properties of Ta_3N_5 NTs. Therefore, we have focused on the short time nitridations of 3 h at higher temperatures to investigate the effect of oxygen content on the PEC activities of Ta_3N_5 NTs (**See Appendix 1**). The morphological, structural, surface and charge transportation properties of the porous Ta_3N_5 NTs were investigated. Performing anodization in a lower electrolyte temperature helped to preserve the tubular morphology at a higher nitridation temperature. X-ray diffraction and high resolution

transmission electron microscopy analyses revealed that nitridation has controlled the preferential orientation along the (110) plane of orthorhombic Ta_3N_5. The oxygen content is one limiting source that influences the PEC activity of the photoanode. Increasing the nitridation temperature increased the grain size, decreased the oxygen substitution defects and Schottky defects in the crystalline structure and removed the amorphous layer on the walls of the NTs. Crystallographically oriented along (110), highly crystalline, larger grain size and lower oxygen containing 900°C-3h demonstrated enhanced photocurrent, which was 3.4-times and *25-fold* higher than the Ta_3N_5 film prepared in this study and the literature reported values, respectively. These results show that porous Ta_3N_5 NTs with crystallographically preferential orientation along (110) and low oxygen content can improve PEC activity.

The work presented here evidently demonstrated that Ta_3N_5 nanotubes strongly adhere to Ta substrate are promising photoelectrodes for PEC devices. However, we have used oxidation sacrificial reagent of $Fe(CN)_6^{3-/4-}$ (aq) to scavenge the photogenerated holes due to the presence of traps under water oxidation conditions. Furthermore, we found that the nanotubes synthesized at 900°C for 3 h of nitridation have presented enhanced PEC activity in $Fe(CN)_6^{3-/4-}$ (aq) compared to all other samples prepared in the current study. To enhance actual water oxidation, Ta_3N_5 NTs needs further modifications. We suggest to incorporate doping elements in the structure of Ta_3N_5 that can help to avoid the trapping states and nitridation should be done at 900°C for 3 hours. Furthermore, in the literature loading suitable oxidizing co-catalysts, such as Co_3O_4, $Co(OH)_x$, IrO_2, Co-Pi etc have shown improvements.[9, 112, 111, 121 119] Therefore, it would be interesting to investigate new doping elements and further co-catalysts for Ta_3N_5. We also suggest a suitable route to synthesize Ta_3N_5 in the form of p-type semiconductor that may help for its long time durability in the aqueous solutions.

APPENDIX 1

PUBLISHED ARTICLES

Article No. 1

Effect of Oxygen Content on the Photoelectrochemical Activity of Crystallographically Preferred Oriented Porous Ta$_3$N$_5$ Nanotubes

Sherdil Khan[†], **Maximiliano J. M. Zapata**[†], **Daniel L. Baptista**[†], **Renato V. Gonçalves**[‡], **Jesum A. Fernandes**[ǁ], **Jairton Dupont**[⊥], **Marcos J. L. Santos**[§], **and Sérgio R. Teixeira**[±†]

[†] Instituto de Física, UFRGS, Av Bento Goncalves 9500 PO Box -15051 91501-970, POA-RS, Brazil

[‡] Instituto de Física de São Carlos, Universidade de São Paulo, CP 369, São Carlos 13560−970, SP Brazil

[§] Instituto de Quimica, UFRGS, Av Bento Goncalves 9500 PO Box -15051 91501-970, POA-RS, Brazil

[ǁ] Department of Chemistry, University of Victoria, Victoria, BC V8W 3 V6, Canada

[⊥] School of Chemistry, University of Nottingham, University Park, Nottingham NG7 2RD, U.K.

*E-mail: durao@if.ufrgs.br. Phone: +55-51-33086498

Abstract
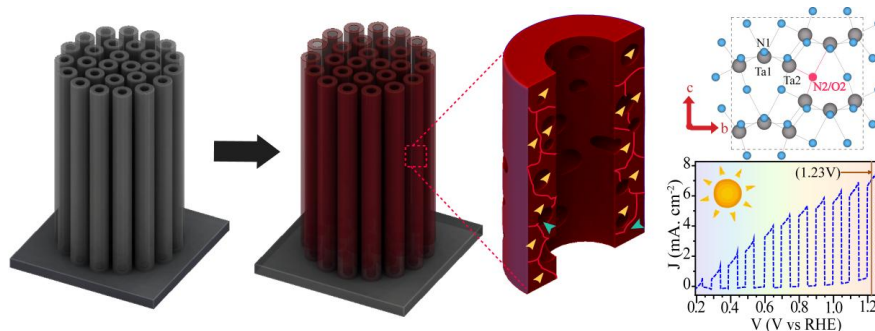
Crystallographically preferred oriented porous Ta$_3$N$_5$ nanotubes (NTs) were synthesized by thermal nitridation of vertically oriented, thick-walled Ta$_2$O$_5$ NTs, strongly adhered to the substrate. The adherence on the substrate and the wall thickness of the Ta$_2$O$_5$ NTs were fine-tuned by anodization, thereby helping to preserve their tubular morphology for nitridation at higher temperatures. Samples were studied by scanning electron microscopy, high-resolution electron microscopy, X-ray diffraction, Rietveld refinements, ultraviolet−visible spectrophotometry, X-ray photoelectron spectroscopy, photoluminescence spectra, and electrochemical techniques. Oxygen content in the structure of porous Ta$_3$N$_5$ NTs strongly influenced their photoelectrochemical activity. Structural analyses revealed that the nitridation temperature has crystallographically controlled the preferential orientation along the (110) direction, reduced the oxygen content in the crystalline structure and the tubular matrix, and increased the grain size. The preferred oriented porous Ta$_3$N$_5$ NTs optimized by the nitridation temperature presented an enhanced photocurrent of 7.4 mA cm^{-2} at 1.23 V vs RHE under AM 1.5 (1 Sun) illumination. Hydrogen production was evaluated by gas chromatography, resulting in 32.8 μmol of H$_2$ in 1 h from the pristine porous Ta$_3$N$_5$ NTs. Electrochemical impedance spectroscopy has shown an effect of nitridation temperature on the interfacial charge transport resistance at the semiconductor−liquid interface; however, the flat band of Ta$_3$N$_5$ NTs remained unchanged.

Article No. 2

Structural, optical and photoelectrochemical characterizations of monoclinic Ta₃N₅ thin films

Sherdil Khan,[a] Maximiliano J. M. Zapata,[a] Marcelo B. Pereira,[a] Renato V. Gonçalves,[b] Lukas Strizik,[c] Jairton Dupont,[d] Marcos J. L. Santos[e] and Sérgio R. Teixeira*[a]

*Corresponding authors

[a] Institute of Physics, Universidade Federal do Rio Grande do Sul, Av Bento Goncalves 9500, P.O. Box – 15051, POA-RS, Brazil

E-mail: srgrbrtxr@gmail.com

[b]Instituto de Física de São Carlos, Universidade de São Paulo, CP 369, São Carlos 13560–970, Brazil

[c]Department of General and Inorganic Chemistry, Faculty of Chemical Technology, University of Pardubice, Studentska 573, Pardubice, Czech Republic

[d]School of Chemistry, University of Nottingham, University Park, Nottingham, UK

[e]Institute of Chemistry, Universidade Federal do Rio Grande do Sul, Av Bento Goncalves 9500, POA-RS, Brazil

Abstract
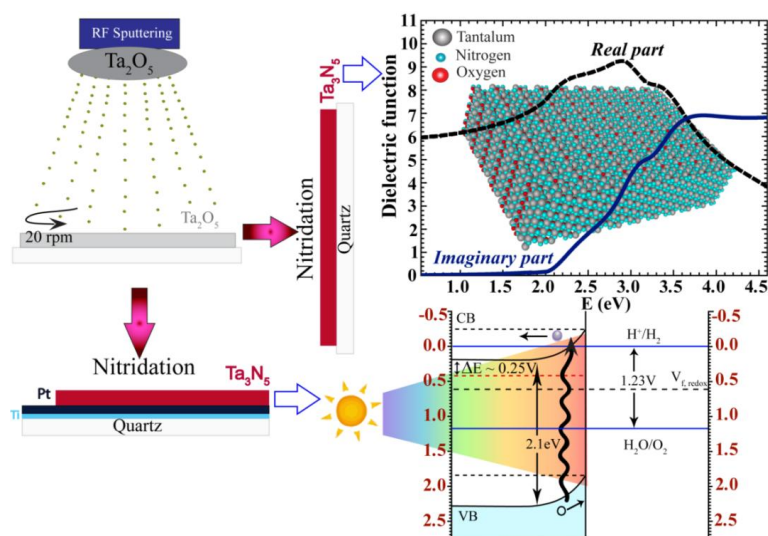
Monoclinic Ta₃N₅ thin films were synthesized by thermal nitridation of amorphous Ta₂O₅ films directly sputtered by radio frequency magnetron sputtering. The samples were studied by high resolution transmission electron microscopy, X-ray photoelectron spectroscopy, UV-Vis-NIR spectrophotometry, Rietveld refinements, spectroscopic ellipsometry (SE) and electrochemical techniques. The surface composition of Ta₃N₅ thin film was found different than the underlying film, affecting the optical properties of the material. The Rietveld refinement has confirmed that nitridation process results in Schottky and oxygen substitutional defects within the crystalline structure of monoclinic Ta₃N₅ thin film. The optical constants of the film were obtained by SE within a spectral range of 4.60–0.54 eV, i.e. 270–2 300 nm. The suitable parameterization was found to consist of three Tauc-Lorentz and one Lorentz oscillators. The conduction band, valence band and the flat band positions were determined by photoelectrochemical (PEC) techniques, presenting a strong dependence on pH of the eletrolyte. Improved photocurrent was obtained in alkaline condition and attributed to the shorter depletion region width measured by Mott-Schottky and the lower recombination life time measured by open circuit potential decay analyses.

Article No .3

(Conference proceeding "IOP Conference Series: Materials Science and Engineering" on the basis of best oral work presentation in SBPMAT meeting, 2014 Joao Pessoa, Brazil)

Photoelectrochemical study of Ta_3N_5 nanotubes for water splitting

Sherdil Khan[1], Marcos J. Leite Santos *[2], Jairton Dupont [2], Sergio R. Teixeira*[1]

[1] Instituto de Física, Universidade Federal do Rio Grande do Sul, Av Bento Gonçalves 9500 POBox - 15051 CEP 91501-970, POA-RS, Brazil.

[2] Instituto de Química, Universidade Federal do Rio Grande do Sul, Av Bento Gonçalves 9500 POBox 15003, CEP 91501-970, POA-RS, Brazil.

E-mail address: *srgrbrtxr@gmail.com*

Abstract. Nanotubes (NTs) of Ta_3N_5 were synthesized by nitridation of Ta_2O_5 NTs. The samples were studied by scanning electron microscopy, UV-VIS spectrophotometry, x-ray diffraction and photoelectrochemical (PEC) measurements carried out in aqueous solutions of Na_2SO_4 and $Fe(CN)_6^{3-/4-}$. The results show the presence of trapping states on illuminated pristine Ta_3N_5 NTs in Na_2SO_4 (aq). These trapping states act as recombination center for photogenerated holes, affecting the photocatalytic performance of Ta_3N_5 NTs. On the other hand, by using $Fe(CN)_6^{3-/4-}$ (aq) the photogenerated holes were scavenged efficiently without giving rise to the trapping states at Ta_3N_5 NTs/solution interface. The results obtained by cyclic voltammetry, linear sweep voltammetry and electrochemical impedance spectroscopy have shown that the presence of these trapping states is a limiting step for water oxidation using pristine Ta_3N_5 NTs.

REFERENCES

1.   Nowotny, J. V., T. Nejat, Impact of hydrogen on the environment. *Int. J. Hydrog. Energy* **2011,** (36), 13218-13224.

2.   Navarro, R. M.; Alvarez-Galvan, M. C.; Villoria de la Mano, J. A.; Al-Zahrani, S. M.; Fierro, J. L. G., A framework for visible-light water splitting. *Energ. Environ. Sci.* **2010,** *3* (12), 1865-1882.

3.   Photoelectrochemical Water Splitting Materials, Processes and Architectures. Hans-Joachim Lewerenz, L. P., Ed. England, **2013**.

4.   https://windowfilmonline.wordpress.com/2008/07/04/infrared-rejection/. **2008**.

5.   United Nations Development Program, World Energy Assessment Report, Energy and the challenge of Sustainabilty. *United Nations, Newyork.* **2003**.

6.   Turner, J. A., A realizable renewable energy future. *Science* **1999,** *285* (5428), 687-689.

7.   Salamat, A.; Hector, A. L.; Kroll, P.; McMillan, P. F., Nitrogen-rich transition metal nitrides. *Coordination Chemistry Reviews* **2013,** *257* (13-14), 2063-2072.

8.   Maeda, K.; Nishimura, N.; Domen, K., A precursor route to prepare tantalum (V) nitride nanoparticles with enhanced photocatalytic activity for hydrogen evolution under visible light. *Appl. Catal. A-Gen.* **2009,** *370* (1-2), 88-92.

9.   Li, Y.; Zhang, L.; Torres-Pardo, A.; Gonzalez-Calbet, J. M.; Ma, Y.; Oleynikov, P.; Terasaki, O.; Asahina, S.; Shima, M.; Cha, D.; Zhao, L.; Takanabe, K.; Kubota, J.; Domen, K., Cobalt phosphate-modified barium-doped tantalum nitride nanorod photoanode with 1.5% solar energy conversion efficiency. *Nature Communications* **2013,** *4*, 1-4.

10.   Wang, Z.; Hou, J.; Yang, C.; Jiao, S.; Huang, K.; Zhu, H., Hierarchical Metastable γ-TaON Hollow Structures for Efficient Visible-Light Water Splitting. *Energ. Environ. Sci.* **2013,** 6, 2134-2144.

11.   Cong, Y.; Park, H. S.; Wang, S.; Dang, H. X.; Fan, F.-R. F.; Mullins, C. B.; Bard, A. J., Synthesis of Ta_3N_5 Nanotube Arrays Modified with Electrocatalysts for Photoelectrochemical Water Oxidation. *J. Phys. Chem. C* **2012,** *116* (27), 14541-14550.

12.   Feng, X. J.; LaTempa, T. J.; Basham, J. I.; Mor, G. K.; Varghese, O. K.; Grimes, C. A., Ta_3N_5 Nanotube Arrays for Visible Light Water Photoelectrolysis. *Nano Letters* **2010,** *10* (3), 948-952.

13.   Cong, Y. Q.; Park, H. S.; Wang, S. J.; Dang, H. X.; Fan, F. R. F.; Mullins, C. B.; Bard, A. J., Synthesis of Ta_3N_5 Nanotube Arrays Modified with Electrocatalysts for Photoelectrochemical Water Oxidation. *J. Phys. Chem. C* **2012,** *116* (27), 14541-14550.

14.   Wang, L.; Nguyen, N. T.; Zhou, X.; Hwang, I.; Killian, M. S.; Schmuki, P., Enhanced Charge Transport in Tantalum Nitride Nanotube Photoanodes for Solar Water Splitting. *ChemSusChem* **2015**, 8, 2615–2620.

15.   Grigorescu, S.; Bärhausen, B.; Wang, L.; Mazare, A.; Yoo, J. E.; Hahn, R.; Schmuki, P., Tungsten doping of Ta_3N_5-nanotubes for band gap narrowing and enhanced photoelectrochemical water splitting efficiency. *Electrochemistry Communications* **2015,** *51*, 85-88.

16.   Su, Z.; Grigorescu, S.; Wang, L.; Lee, K.; Schmuki, P., Fast fabrication of Ta2O5 nanotube arrays and their conversion to Ta_3N_5 for efficient solar driven water splitting. *Electrochemistry Communications* **2015,** *50*, 15-19.

17.   Zhang, P.; Wang, T.; Zhang, J.; Chang, X.; Gong, J., Bridging the transport pathway of charge carriers in a Ta_3N_5 nanotube array photoanode for solar water splitting. *Nanoscale* **2015,** *7* (31), 13153-13158.

18.   Zhebo Chen, E. M., Huyen N. Dinh, Photoelectrochemical Water Splitting (Standards, Experimental Methods, and Protocols), Springer New York Heidelberg Dordrecht London. **2013**.

19.   Krishnan, R., Fundamentals of Semiconductor Electrochemistry and Photoelectrochemistry. In *Encyclopedia of Electrochemistry*, Wiley-VCH Verlag GmbH & Co. KGaA: **2007**.

20.   Beranek, R., (Photo)electrochemical Methods for the Determination of the Band Edge Positions of TiO_2-Based Nanomaterials. *Advances in Physical Chemistry* **2011,** *2011*, 1-20.

21.   Grimes, C. A.; Mor, G. K., *TiO2 Nanotube Arrays - Synthesis, Properties, and Applications*. Springer: New York, **2009**; p 1-345.

22.   (a) Allen J Bard, M. S., Stuart Licht., Encyclopedia of Electrochemistry: Semiconductor Electrodes and Photoelectrochemistry. **2002**.

23.   Li, Z.; Luo, W.; Zhang, M.; Feng, J.; Zou, Z., Photoelectrochemical cells for solar hydrogen production: current state of promising photoelectrodes, methods to improve their properties, and outlook. *Energ. Environ. Sci.* **2013,** *6* (2), 347.

24.   The Concept of Fermi Level Pinning at Semiconductor/Liquid Junctions. Consequences for Energy Conversion Efficiency and Selection of Useful Solution Redox Couples in Solar Devices, *J. Am. Chem. Soc.*, **1980**, 102 (11), pp 3671–3677.

25.   CARL A. KOVAL, J. N. H., Electron Transfer at Semiconductor Electrode-Liquid Electrolyte Interfaces, . *Chem. Rev.* **1992***, 92, 411-433*.

26.   (a) Arthur J. Nozik, R. M., Physical Chemistry of Semiconductor-Liquid Interfaces. . *J. Phys. Chem.* **1996***, 100, 13061-13078*; (b) Allen J. Bard, L. R. F., Electrochemical Methods: Fundamentals and Applications, . **2000**.

27.   Morisaki, H.; Hariya, M.; Yazawa, K., Anomalous photoresponse of n-TiO_2 electrode in a photoelectrochemical cell. *Appl. Phys. Lett.* **1977,** *30* (1), 7.

28.   L M Peter, D. V., *Advances in Electrochemical Science and Engineering.* **1999,** (6), 77.

29.   Gerischer, H., The role of semiconductor structure and surface properties in photoelectrochemical processes. *Journal of Electroanalytical Chemistry and Interfacial Electrochemistry* **1983,** *150* (1–2), 553-569.

30.   Koval, C. A.; Howard, J. N., Electron transfer at semiconductor electrode-liquid electrolyte interfaces. *Chemical Reviews* **1992,** *92* (3), 411-433.

31.   Gratze, A. H. a. M., Light-Induced Redox Reactions in Nanocrystalline Systems. *Chem. Rev. 1995, 95, 49-68* **1995**.

32.   Le Formal, F.; Sivula, K.; Graetzel, M., The Transient Photocurrent and Photovoltage Behavior of a Hematite Photoanode under Working Conditions and the Influence of Surface Treatments. *J. Phys. Chem. C* **2012,** *116* (51), 26707-26720.

33.   Jennings, J. R.; Ghicov, A.; Peter, L. M.; Schmuki, P.; Walker, A. B., Dye-Sensitized Solar Cells Based on Oriented TiO_2 Nanotube Arrays: Transport, Trapping, and Transfer of Electrons. *J. Am. Chem. Soc.* **2008,** *130* (40), 13364-13372.

34.   Klahr, B.; Gimenez, S.; Fabregat-Santiago, F.; Hamann, T.; Bisquert, J., Water Oxidation at Hematite Photoelectrodes: The Role of Surface States. *J. Am. Chem. Soc.* **2012,** *134* (9), 4294-4302.

35.   Mercado, C. C.; Knorr, F. J.; McHale, J. L., Observation of Charge Transport in Single Titanium Dioxide Nanotubes by Micro-Photoluminescence Imaging and Spectroscopy. *Acs Nano* **2012,** *6* (8), 7270-7280.

36.   Howe, R. F.; Gratzel, M., EPR observation of trapped electrons in colloidal titanium dioxide. *The Journal of Physical Chemistry* **1985,** *89* (21), 4495-4499.

37.   Wang, H.; He, J.; Boschloo, G.; Lindström, H.; Hagfeldt, A.; Lindquist, S.-E., Electrochemical Investigation of Traps in a Nanostructured TiO_2 Film. *The Journal of Physical Chemistry B* **2001,** *105* (13), 2529-2533.

38.   Palmas, S.; Da Pozzo, A.; Mascia, M.; Vacca, A.; Ricci, P. C.; Matarrese, R., On the redox behaviour of glycerol at TiO_2 electrodes. *J. Solid State Electrochem.* **2012,** *16* (7), 2493-2502.

39.   Jankulovska, M.; Berger, T.; Wong, S. S.; Gómez, R.; Lana-Villarreal, T., Trap States in TiO_2 Films Made of Nanowires, Nanotubes or Nanoparticles: An Electrochemical Study. *ChemPhysChem* **2012,** *13* (12), 3008-3017.

40.   Mercado, C. C.; Knorr, F. J.; McHale, J. L.; Usmani, S. M.; Ichimura, A. S.; Saraf, L. V., Location of Hole and Electron Traps on Nanocrystalline Anatase TiO_2. *The Journal of Physical Chemistry C* **2012,** *116* (19), 10796-10804.

41.   Klahr, B.; Gimenez, S.; Fabregat-Santiago, F.; Bisquert, J.; Hamann, T. W., Electrochemical and photoelectrochemical investigation of water oxidation with hematite electrodes. *Energ. Environ. Sci.* **2012,** *5* (6), 7626-7636.

42.   Schäfer, S.; Koch, A. H. R.; Cavallini, A.; Stutzmann, M.; Sharp, I. D., Charge Transfer across the n-Type GaN–Electrolyte Interface. *The Journal of Physical Chemistry C* **2012,** *116* (42), 22281-22286.

43.   Nishida, M., A theoretical treatment of charge-transfer via surface-states at a semiconductor-electrolyte interface - analysis of the water photoelectrolysis process. *J. Appl. Phys.* **1980,** *51* (3), 1669-1675.

44.   Klahr, B.; Gimenez, S.; Fabregat-Santiago, F.; Bisquert, J.; Hamann, T. W., Electrochemical and photoelectrochemical investigation of water oxidation with hematite electrodes. *Energ. Environ. Sci.* **2012,** *5* (6), 7626.

45.   Reichman, J., The current-voltage characteristics of semiconductor-electrolyte junction photovoltaic cells. *Appl. Phys. Lett.* **1980,** *36* (7), 574-577.

46.   Fujishima, A.; Honda, K., Electrochemical photolysis of water at a semiconductor electrode. *Nature* **1972,** *238* (5358), 37.

47.   Lewerenz, H. J.; Heine, C.; Skorupska, K.; Szabo, N.; Hannappel, T.; Vo-Dinh, T.; Campbell, S. A.; Klemm, H. W.; Munoz, A. G., Photoelectrocatalysis: principles, nanoemitter applications and routes to bio-inspired systems. *Energ. Environ. Sci.* **2010,** *3* (6), 748-760.

48.   Ndiege, N.; Chandrasekharan, R.; Radadia, A. D.; Harris, W.; Mintz, E.; Masel, R. I.; Shannon, M. A., Synthesis, Characterization, and Photoactivity of Ta_2O_5-Grafted SiO_2 Nanoparticles. *Chemistry – A European Journal* **2011,** *17* (27), 7685-7693.

49.   Renato V. Gonçalves, e. a., Ta_2O_5 Nanotubes Obtained by Anodization: Effect of Thermal Treatment on the Photocatalytic Activity for Hydrogen Production, *J. Phys. Chem. C*, 2012, 116 (26), pp 14022–14030.

50.   Fernandes, J. A.; Migowski, P.; Fabrim, Z.; Feil, A. F.; Rosa, G.; Khan, S.; Machado, G. J.; Fichtner, P. F. P.; Teixeira, S. R.; Santos, M. J. L.; Dupont, J., TiO_2 nanotubes sensitized with CdSe via RF magnetron sputtering for photoelectrochemical applications under visible light irradiation. *Phys. Chem. Chem. Phys.* **2014,** (16), 9148-9153.

51.   Seddon, M. J. E. a. K. R., Ionic liquids. Green solvents for the future, *Pure Appl. Chem.* **2000,** 72, 1391-1398.

52.   Welton, T., Room-Temperature Ionic Liquids. Solvents for Synthesis and Catalysis. *Chem. Rev.* **1999,** *99* (8), 2071-2084.

53.   Ishikawa, A.; Takata, T.; Kondo, J. N.; Hara, M.; Domen, K., Electrochemical behavior of thin Ta_3N_5 semiconductor film. *Journal of Physical Chemistry B* **2004,** *108* (30), 11049-11053.

54.   Cong, Y. Q.; Park, H. S.; Dang, H. X.; Fan, F. R. F.; Bard, A. J.; Mullins, C. B., Tantalum Cobalt Nitride Photocatalysts for Water Oxidation under Visible Light. *Chem Mater* **2012,** *24* (3), 579-586.

55.   Dang, H. X.; Hahn, N. T.; Park, H. S.; Bard, A. J.; Mullins, C. B., Nanostructured Ta_3N_5 Films as Visible-Light Active Photoanodes for Water Oxidation. *J. Phys. Chem. C* **2012,** *116* (36), 19225-19232.

56.   Chun, W. J.; Ishikawa, A.; Fujisawa, H.; Takata, T.; Kondo, J. N.; Hara, M.; Kawai, M.; Matsumoto, Y.; Domen, K., Conduction and valence band positions of Ta_2O_5, TaON, and Ta_3N_5 by UPS and electrochemical methods. *Journal of Physical Chemistry B* **2003,** *107* (8), 1798-1803.

57.   Swisher, J. H.; Read, M. H., Thermodynamic properties and electrical conductivity of Ta_3N_5 and TaON. *Metallurgical Transactions* **1972,** *3* (2), 489-&.

58.   Stampfl, C.; Freeman, A. J., Stable and metastable structures of the multiphase tantalum nitride system. *Physical Review B* **2005,** *71* (2).

59.   Dabirian, A.; van de Krol, R., Resonant optical absorption and defect control in Ta_3N_5 photoanodes. *Appl. Phys. Lett.* **2013,** *102* (3), 033905.

60.   Lee, Y.; Nukumizu, K.; Watanabe, T.; Takata, T.; Hara, M.; Yoshimura, M.; Domen, K., Effect of 10 MPa ammonia treatment on the activity of visible light responsive Ta_3N_5 photocatalyst. *Chem. Lett.* **2006,** *35* (4), 352-353.

61.   H. Funk, H. Boehland "Zur Darstellung von Metallnitriden aus Ammonium?uorometallaten und Ammoniak," *Z. Anorg. Allg. Chem.* **1964** 334, pp. 155—162.

62.   Brauer, G.; Weidlein, J. R., Synthesis and properties of red tantalum nitride Ta$_3$N$_5$. *Angewandte Chemie-International Edition* **1965,** *4* (3), 241-&.

63.   Strahle, J., Crystal-structure of tantalum(v) nitride Ta$_3$N$_5$. *Zeitschrift Fur Anorganische Und Allgemeine Chemie* **1973,** *402* (1), 47-57.

64.   Hieber, K., Structural and electrical properties of Ta and Ta nitrides deposited by chemical vapour deposition. *Thin Solid Films* **1974,** *24* (1), 157-164.

65.   Terao, N., Electron-diffraction study of structure of tantalum nitride Ta$_3$N$_5$. *Comptes Rendus Hebdomadaires Des Seances De L Academie Des Sciences Serie B* **1977,** *285* (1), 17-20.

66.   Brese, N. E.; Okeeffe, M.; Rauch, P.; Disalvo, F. J., Structure of Ta$_3$N$_5$ at 16-k by time-of-flight neutron-diffraction. *Acta Crystallographica Section C-Crystal Structure Communications* **1991,** *47*, 2291-2294.

67.   Fang, C. M.; Orhan, E.; de Wijs, G. A.; Hintzen, H. T.; de Groot, R. A.; Marchand, R.; Saillard, J. Y.; de With, G., The electronic structure of tantalum (oxy)nitrides TaON and Ta$_3$N$_5$. *Journal of Materials Chemistry* **2001,** *11* (4), 1248-1252.

68.   Wang, J. J.; Fang, T.; Zhang, L.; Feng, J. Y.; Li, Z. S.; Zou, Z. G., Effects of oxygen doping on optical band gap and band edge positions of Ta$_3$N$_5$ photocatalyst: A GGA plus U calculation. *J Catal* **2014,** *309*, 291-299.

69.   Hara, M.; Hitoki, G.; Takata, T.; Kondo, J. N.; Kobayashi, H.; Domen, K., TaON and Ta$_3$N$_5$ as new visible light driven photocatalysts. *Catalysis Today* **2003,** *78* (1-4), 555-560.

70.   Lu, D. L.; Hitoki, G.; Katou, E.; Kondo, J. N.; Hara, M.; Domen, K., Porous single-crystalline TaON and Ta$_3$N$_5$ particles. *Chemistry of Materials* **2004,** *16* (9), 1603-1605.

71.   Hisatomi, T.; Otani, M.; Nakajima, K.; Teramura, K.; Kako, Y.; Lu, D. L.; Takata, T.; Kondo, J. N.; Domen, K., Preparation of Crystallized Mesoporous Ta$_3$N$_5$ Assisted by Chemical Vapor Deposition of Tetramethyl Orthosilicate. *Chem Mater* **2010,** *22* (13), 3854-3861.

72.   Tabata, M.; Maeda, K.; Higashi, M.; Lu, D. L.; Takata, T.; Abe, R.; Domen, K., Modified Ta$_3$N$_5$ Powder as a Photocatalyst for O$_2$ Evolution in a Two-Step Water Splitting System with an Iodate/Iodide Shuttle Redox Mediator under Visible Light. *Langmuir* **2010,** *26* (12), 9161-9165.

73.   (a) Yuliati, L.; Yang, J. H.; Wang, X. C.; Maeda, K.; Takata, T.; Antonietti, M.; Domen, K., Highly active tantalum(v) nitride nanoparticles prepared from a mesoporous carbon nitride template for photocatalytic hydrogen evolution under visible light irradiation. *J. Mater. Chem.* **2010,** *20* (21), 4295-4298; (b) Gao, R.; Zhou, S. X.; Chen, M.; Wu, L. M.,

Facile synthesis of monodisperse meso-microporous Ta_3N_5 hollow spheres and their visible light-driven photocatalytic activity. *Journal of Materials Chemistry* **2011,** *21* (43), 17087-17090.

74.   Ma, S. S. K.; Hisatomi, T.; Maeda, K.; Moriya, Y.; Domen, K., Enhanced Water Oxidation on Ta_3N_5 Photocatalysts by Modification with Alkaline Metal Salts. *J Am Chem Soc* **2012,** *134* (49), 19993-19996.

75.   Grimes, C. A.; Mor, G. K., *TiO_2 Nanotube Arrays: Synthesis, Properties, and Applications*. Springer: 2009.

76.   (a) Roy, P.; Berger, S.; Schmuki, P., TiO_2 Nanotubes: Synthesis and Applications. *Angewandte Chemie International Edition* **2011,** *50* (13), 2904-2939; (b) Aerts, T.; Dimogerontakis, T.; De Graeve, I.; Fransaer, J.; Terryn, H., Influence of the anodizing temperature on the porosity and the mechanical properties of the porous anodic oxide film. *Surf. Coat. Technol.* **2007,** *201* (16-17), 7310-7317.

77.   El-Sayed, H. A.; Birss, V. I., Controlled Interconversion of Nanoarray of Ta Dimples and High Aspect Ratio Ta Oxide Nanotubes. *Nano Letters* **2009,** *9* (4), 1350-1355.

78.   Barton, J. E.; Stender, C. L.; Li, P.; Odom, T. W., Structural control of anodized tantalum oxide nanotubes. *J. Mater. Chem.* **2009,** *19* (28), 4896-4898.

79.   El-Sayed, H. A.; Birss, V. I., Controlled growth and monitoring of tantalum oxide nanostructures. *Nanoscale* **2010,** *2* (5), 793-798.

80.   Goncalves, R. V.; Migowski, P.; Wender, H.; Feil, A. F.; Zapata, M. J. M.; Khan, S.; Bernardi, F.; Azevedo, G. M.; Teixeira, S. R., On the crystallization of Ta_2O_5 nanotubes: structural and local atomic properties investigated by EXAFS and XRD. *Crystengcomm* **2014,** *16* (5), 797-804.

81.   El-Sayed, H.; Singh, S.; Greiner, M. T.; Kruse, P., Formation of Highly Ordered Arrays of Dimples on Tantalum at the Nanoscale. *Nano Letters* **2006,** *6* (12), 2995-2999.

82.   Kado, Y.; Lee, C.-Y.; Lee, K.; Müller, J.; Moll, M.; Spiecker, E.; Schmuki, P., Enhanced water splitting activity of M-doped Ta_3N_5 (M = Na, K, Rb, Cs). *Chem Commun* **2012,** *48* (69), 8685.

83.   Zhebo Chen, H. N. D., Eric Miller, *Photoelectrochemical Water Splitting (Standards, Experimental Methods, and Protocols)*. Springer New York Heidelberg Dordrecht London: 2013.

84.   Rodríguez-Carvajal, J., Recent advances in magnetic structure determination by neutron powder diffraction. *Physica B: Condensed Matter* **1993,** *192* (1–2), 55-69.

85.   Thompson, P.; Cox, D. E.; Hastings, J. B., Rietveld refinement of Debye-Scherrer synchrotron X-ray data from Al_2O_3. *Journal of Applied Crystallography* **1987,** *20* (2), 79-83.

86.   Dollase, W., Correction of intensities for preferred orientation in powder diffractometry: application of the March model. *Journal of Applied Crystallography* **1986,** *19* (4), 267-272.

87.   McCusker, L. B.; Von Dreele, R. B.; Cox, D. E.; Louer, D.; Scardi, P., Rietveld refinement guidelines. *Journal of Applied Crystallography* **1999,** *32* (1), 36-50.

88.   Goncalves, R. V.; Migowski, P.; Wender, H.; Eberhardt, D.; Weibel, D. E.; Sonaglio, F. C.; Zapata, M. J. M.; Dupont, J.; Feil, A. F.; Teixeira, S. R., Ta_2O_5 Nanotubes Obtained by Anodization: Effect of Thermal Treatment on the Photocatalytic Activity for Hydrogen Production. *Journal of Physical Chemistry C* **2012,** *116* (26), 14022-14030.

89.   Jarvinen, M., Application of symmetrized harmonics expansion to correction of the preferred orientation effect. *Journal of Applied Crystallography* **1993,** *26* (4), 525-531.

90.   K.H. Zaininger, A. G. R., *RCA Reviews.* **1964,** (25 (1)), 85.

91.   M. Born, E. W., Principles of Optics: Electromagnetic Theory of Propagation Interference and Diffraction of Light, . Cambridge University Press, Cambridge: **1997.**

92.   Muller, R. H., Definitions and Conventions in Ellipsometry", Surface Science. **1969**.

93.   M. Courdille, M. S., J.B. Thesten,, Demande de Brevet D'Invention (French). **1980**.

94.   Pinaud, B. A.; Vailionis, A.; Jaramillo, T. F., Controlling the Structural and Optical Properties of Ta_3N_5 Films through Nitridation Temperature and the Nature of the Ta Metal. *Chemistry of Materials* **2014,** *26* (4), 1576-1582.

95.   Henderson, S. J.; Hector, A. L., Structural and compositional variations in Ta_3N_5 produced by high-temperature ammonolysis of tantalum oxide. *Journal of Solid State Chemistry* **2006,** *179* (11), 3518-3524.

96.   Young, K. F.; Frederikse, H. P. R., Compilation of the Static Dielectric Constant of Inorganic Solids. *Journal of Physical and Chemical Reference Data* **1973,** *2* (2), 313-410.

97.   Mohamed, S. H.; Kappertz, O.; Niemeier, T.; Drese, R.; Wakkad, M. M.; Wuttig, M., Effect of heat treatment on structural, optical and mechanical properties of sputtered TiO_xN_y films. *Thin Solid Films* **2004,** *468* (1-2), 48-56.

98.   Zhang, Q. H.; Gao, L., Ta_3N_5 nanoparticles with enhanced photocatalytic efficiency under visible light irradiation. *Langmuir* **2004,** *20* (22), 9821-9827.

99.   Chun, W.-J.; Ishikawa, A.; Fujisawa, H.; Takata, T.; Kondo, J. N.; Hara, M.; Kawai, M.; Matsumoto, Y.; Domen, K., Conduction and Valence Band Positions of Ta_2O_5, TaON,

and Ta$_3$N$_5$ by UPS and Electrochemical Methods. *The Journal of Physical Chemistry B* **2003,** *107* (8), 1798-1803.

100.   Satoshi Hashimoto, C. T., Aki Murata, and Tsuguo Sakurada, Formulation for XPS Spectral Change of oxides by Ar Ion Bombardment: Application of the Formulation to Ta$_2$O$_5$ System. *Journal of Surface Analysis* **2006,** *Vol.13 (No. 1) 14 - 18*

101.   Goncalves, R. V.; Wojcieszak, R.; Uberman, P. M.; Teixeira, S. R.; Rossi, L. M., Insights into the active surface species formed on Ta$_2$O$_5$ nanotubes in the catalytic oxidation of CO. *Phys. Chem. Chem. Phys.* **2014,** *16* (12), 5755-5762.

102.   (a) Feng, W.; Chen, G.; Li, L.; Lv, G.; Zhang, X.; Niu, E.; Liu, C.; Yang, S.-z., Characteristics of (Ti,Ta)N thin films prepared by using pulsed high energy density plasma. *Journal of Physics D: Applied Physics* **2007,** *40* (14), 4228-4233; (b) Li, M.; Luo, W.; Cao, D.; Zhao, X.; Li, Z.; Yu, T.; Zou, Z., A Co-catalyst-Loaded Ta$_3$N$_5$ Photoanode with a High Solar Photocurrent for Water Splitting upon Facile Removal of the Surface Layer. *Angewandte Chemie International Edition* **2013,** *52* (42), 11016-11020.

103.   Nurlaela, E.; Ould-Chikh, S.; Harb, M.; del Gobbo, S.; Aouine, M.; Puzenat, E.; Sautet, P.; Domen, K.; Basset, J.-M.; Takanabe, K., Critical Role of the Semiconductor–Electrolyte Interface in Photocatalytic Performance for Water-Splitting Reactions Using Ta$_3$N$_5$ Particles. *Chemistry of Materials* **2014,** *26* (16), 4812-4825.

104.   Soave, P. A. D., R. A. F.; Becker, M. R.; Pereira, M. B.; Horowitz, F., Refractive index control in bicomponent polymer films for integrated thermo-optical applications. *Optical Engineering (Bellingham. Print) 48*, 12460.

105.   Degryse, R.; Gomes, W. P.; Cardon, F.; Vennik, J., Interpretation of mott-schottky plots determined at semiconductor-electrolyte systems. *J Electrochem Soc* **1975,** *122* (5), 711-712.

106.   Matsumoto, Y., Energy positions of oxide semiconductors and photocatalysis with iron complex oxides. *Journal of Solid State Chemistry* **1996,** *126* (2), 227-234.

107.   Abe, R., Recent progress on photocatalytic and photoelectrochemical water splitting under visible light irradiation. *J. Photochem. Photobiol. C-Photochem. Rev.* **2010,** *11* (4), 179-209.

108.   Tilley, S. D.; Cornuz, M.; Sivula, K.; Grätzel, M., Light-Induced Water Splitting with Hematite: Improved Nanostructure and Iridium Oxide Catalysis. *Angewandte Chemie International Edition* **2010,** *49* (36), 6405-6408.

109.   Li, M.; Luo, W.; Cao, D.; Zhao, X.; Li, Z.; Yu, T.; Zou, Z., A Cocatalyst-Loaded Ta_3N_5 Photoanode with a High Solar Photocurrent for Water Splitting upon Facile Removal of the Surface Layer. *Angewandte Chemie International Edition* **2013**, 52, 1 – 6.

110.   Li, Y. B.; Takata, T.; Cha, D.; Takanabe, K.; Minegishi, T.; Kubota, J.; Domen, K., Vertically Aligned Ta_3N_5 Nanorod Arrays for Solar-Driven Photoelectrochemical Water Splitting. *Advanced Materials* **2013,** *25* (1), 125-131.

111.   Liao, M.; Feng, J.; Luo, W.; Wang, Z.; Zhang, J.; Li, Z.; Yu, T.; Zou, Z., Co3O4 Nanoparticles as Robust Water Oxidation Catalysts Towards Remarkably Enhanced Photostability of a Ta_3N_5 Photoanode. *Advanced Functional Materials* **2012,** *22* (14), 3066-3074.

112.   Yokoyama, D.; Hashiguchi, H.; Maeda, K.; Minegishi, T.; Takata, T.; Abe, R.; Kubota, J.; Domen, K., Ta_3N_5 photoanodes for water splitting prepared by sputtering. *Thin Solid Films* **2011,** *519* (7), 2087-2092.

113.   Kado, Y.; Lee, C. Y.; Lee, K.; Muller, J.; Moll, M.; Spiecker, E.; Schmuki, P., Enhanced water splitting activity of M-doped Ta_3N_5 (M = Na, K, Rb, Cs). *Chemical Communications* **2012,** *48* (69), 8685-8687.

114.   Wang, W. Y.; Chen, B. R., Characterization and Photocatalytic Activity of TiO2 Nanotube Films Prepared by Anodization. *International Journal of Photoenergy* **2013**.

115.   Mor, G. K.; Shankar, K.; Paulose, M.; Varghese, O. K.; Grimes, C. A., Enhanced photocleavage of water using titania nanotube arrays. *Nano Letters* **2005,** *5* (1), 191-195.

116.   Salvador, P., Kinetic approach to the photocurrent transients in water photoelectrolysis at n-TiO_2 electrodes .1. analysis of the ratio of the instantaneous to steady-state photocurrent. *J. Phys. Chem.* **1985,** *89* (18), 3863-3869.

117.   Lincot, D.; Vedel, J., Recombination and charge-transfer at the illuminated n-cdte electrolyte interface - simplified kinetic-model. *Journal of Electroanalytical Chemistry* **1987,** *220* (2), 179-200.

118.   Hou, J.; Wang, Z.; Yang, C.; Cheng, H.; Jiao, S.; Zhu, H., Cobalt-bilayer catalyst decorated Ta_3N_5 nanorod arrays as integrated electrodes for photoelectrochemical water oxidation. *Energ. Environ. Sci.* **2013,** *6* (11), 3322.

119.   Zhen, C.; Wang, L.; Liu, G.; Lu, G. Q.; Cheng, H.-M., Template-free synthesis of Ta_3N_5 nanorod arrays for efficient photoelectrochemical water splitting. *Chem. Commun.* **2013,** *49* (29), 3019.

120. Higashi, M.; Domen, K.; Abe, R., Fabrication of efficient TaON and Ta$_3$N$_5$ photoanodes for water splitting under visible light irradiation. *Energy & Environmental Science* **2011,** *4* (10), 4138-4147.

121. Li, Y.; Takata, T.; Cha, D.; Takanabe, K.; Minegishi, T.; Kubota, J.; Domen, K., Vertically Aligned Ta$_3$N$_5$ Nanorod Arrays for Solar-Driven Photoelectrochemical Water Splitting. *Advanced Materials* **2013,** *25* (1), 125-131.

122. Abrantes, L. M.; Peter, L. M., Transient photocurrents at passive iron electrodes. *Journal of Electroanalytical Chemistry and Interfacial Electrochemistry* **1983,** *150* (1–2), 593-601.

123. Ghicov, A.; Tsuchiya, H.; Macak, J. M.; Schmuki, P., Annealing effects on the photoresponse of TiO$_2$ nanotubes. *physica status solidi (A)* **2006,** *203* (4), R28-R30.

124. Tsuchiya, H.; Macak, J. M.; Ghicov, A.; Räder, A. S.; Taveira, L.; Schmuki, P., Characterization of electronic properties of TiO$_2$ nanotube films. *Corrosion Science* **2007,** *49* (1), 203-210.

125. Reemts, J.; Kittel, A., Persistent photoconductivity in highly porous ZnO films. *J Appl Phys* **2007,** *101* (1), 013709.

126. Covington, L. R.; Moore, J. C., Photoconductivity and transient response of Al:ZnO:Al planar structures fabricated via a thermal oxidation process. *Thin Solid Films* **2013,** *540* (0), 106-111.

127. Fabregat-Santiago, F.; Randriamahazaka, H.; Zaban, A.; Garcia-Ca?adas, J.; Garcia-Belmonte, G.; Bisquert, J., Chemical capacitance of nanoporous-nanocrystalline TiO$_2$ in a room temperature ionic liquid. *Phys. Chem. Chem. Phys.* **2006,** *8* (15), 1827.

128. Fabregat-Santiago, F.; Mora-Sero, I.; Garcia-Belmonte, G.; Bisquert, J., Cyclic voltammetry studies of nanoporous semiconductors. Capacitive and reactive properties of nanocrystalline TiO$_2$ electrodes in aqueous electrolyte. *J. Phys. Chem. B* **2003,** *107* (3), 758-768.

129. Bisquert, J.; Fabregat-Santiago, F.; Mora-Seró, I.; Garcia-Belmonte, G.; Barea, E. M.; Palomares, E., A review of recent results on electrochemical determination of the density of electronic states of nanostructured metal-oxide semiconductors and organic hole conductors. *Inorg. Chim. Acta* **2008,** *361* (3), 684-698.

130. Bertoluzzi, L.; Badia-Bou, L.; Fabregat-Santiago, F.; Gimenez, S.; Bisquert, J., Interpretation of Cyclic Voltammetry Measurements of Thin Semiconductor Films for Solar Fuel Applications. *J. Phys. Chem. Lett.* **2013,** *4* (8), 1334-1339.

131. Hara, M.; Chiba, E.; Ishikawa, A.; Takata, T.; Kondo, J. N.; Domen, K., Ta_3N_5 and TaON thin films on Ta foil: Surface composition and stability. *Journal of Physical Chemistry B* **2003,** *107* (48), 13441-13445.

132. Wang, Y.-C.; Chang, C.-Y.; Yeh, T.-F.; Lee, Y.-L.; Teng, H., Formation of internal p-n junctions in Ta_3N_5 photoanodes for water splitting. *Journal of Materials Chemistry A* **2014,** *2* (48), 20570-20577.

133. Djellal, L.; Bouguelia, A.; Trari, M., Physical and photoelectrochemical properties of p-$CuInSe_2$ bulk material. *Mater. Chem. Phys.* **2008,** *109* (1), 99-104.

134. Nishida, M., Charge-transfer by surface-states in the photoelectrolysis of water using a semiconductor electrode. *Nature* **1979,** *277* (5693), 202-203.

135. Dutoit, E. C.; van Meirhaeghe, R. L.; Cardon, F.; Gomes, W. P., Investigation on the frequency-dependence of the impedance of the nearly ideally polarizable semiconductor electrodes CdSe, CdS and TiO_2. *Berichte der Bunsengesellschaft für physikalische Chemie* **1975,** *79* (12), 1206-1213.

136. Shankar, K.; Basham, J. I.; Allam, N. K.; Varghese, O. K.; Mor, G. K.; Feng, X.; Paulose, M.; Seabold, J. A.; Choi, K.-S.; Grimes, C. A., Recent Advances in the Use of TiO_2 Nanotube and Nanowire Arrays for Oxidative Photoelectrochemistry. *J. Phys. Chem. C* **2009,** *113* (16), 6327-6359.

137. Kim, H.-i.; Monllor-Satoca, D.; Kim, W.; Choi, W., N-doped TiO_2 nanotubes coated with a thin TaO_xN_y layer for photoelectrochemical water splitting: dual bulk and surface modification of photoanodes. *Energ. Environ. Sci.* **2015,** *8* (1), 247-257.

138. Mohamed, A. M.; Aljaber, A. S.; AlQaradawi, S. Y.; Allam, N. K., TiO_2 nanotubes with ultrathin walls for enhanced water splitting. *Chem. Commun.* **2015,** *51* (63), 12617-12620.

139. Sabat, R. G.; Santos, M. J. L.; Rochon, P., Surface Plasmon-Induced Band Gap in the Photocurrent Response of Organic Solar Cells. *Int. J. Photoenergy* **2010,** *2010*, 5.

140. Santos, M. J. L.; Rubira, A. F.; Pontes, R. M.; Basso, E. A.; Girotto, E. M., Electrochromic properties of poly(alkoxy-terthiophenes): an experimental and theoretical investigation. *J. Solid State Electrochem.* **2006,** *10* (2), 117-122.

141. Hou, J. G.; Wang, Z.; Yang, C.; Cheng, H. J.; Jiao, S. Q.; Zhu, H. M., Cobalt-bilayer catalyst decorated Ta_3N_5 nanorod arrays as integrated electrodes for photoelectrochemical water oxidation. *Energ. Environ. Sci.* **2013,** *6* (11), 3322-3330.

142. Wang, J.; Feng, J.; Zhang, L.; Li, Z.; Zou, Z., Role of oxygen impurity on the mechanical stability and atomic cohesion of Ta_3N_5 semiconductor photocatalyst. *Physical Chemistry Chemical Physics* **2014,** *16* (29), 15375-15380.

143. Dubal, D. P.; Lee, S. H.; Kim, J. G.; Kim, W. B.; Lokhande, C. D., Porous polypyrrole clusters prepared by electropolymerization for a high performance supercapacitor. *J. Mater. Chem.* **2012,** *22* (7), 3044-3052.

144. Jorcin, J.-B.; Orazem, M. E.; Pébère, N.; Tribollet, B., CPE analysis by local electrochemical impedance spectroscopy. *Electrochim. Acta* **2006,** *51* (8-9), 1473-1479.

145. Shoar Abouzari, M. R.; Berkemeier, F.; Schmitz, G.; Wilmer, D., On the physical interpretation of constant phase elements. *Solid State Ionics* **2009,** *180* (14-16), 922-927.

146. Dabirian, A.; van de Krol, R., Resonant optical absorption and defect control in Ta_3N_5 photoanodes. *Applied Physics Letters* **2013,** *102* (3).